The Physical and Numerical Representation of Turbulent Flow over a Porous Riverbed

Alex Stubbs

School of Engineering

Cardiff University, Wales, UK

Supervised by:

Dr. Michaela Bray and Prof. Shunqi Pan

This thesis is submitted in partial fulfilment of the requirements

for the degree of

Doctor of Philosophy (Ph.D.)

2021

Acknowledgements

Cardiff, 2021   Alex Stubbs

Abstract

There are numerous scenarios in which turbulent flow interactions are of great importance, particularly in nature, where the dispersion and exchange of oxygen and nutrients is directly related to the turbulence over riverbeds. However, due to the highly complex nature of both the flow field and the bed geometry, the study of turbulent flow phenomena in open channel flows above and within porous media is highly challenging. A fundamental challenge is how to represent a natural gravel riverbed in terms of surface roughness characteristics, porosity, particle packing, grain size, and grain shape variation. In both experimental and computational studies alike, impermeable roughness surfaces have been successfully employed and have shed much light on flow interactions with roughness elements. Some progress has also been made investigating turbulent flow behaviours with permeable bed surfaces. However, such experimental studies have limitations in terms of gathering data between roughness elements. Equally, such numerical studies are limited by the numerical representation of the geometry of the bed itself. Therefore, this study aims to provide methodology for the manufacture of a physical representation as well as the generation of a numerical representation of a natural gravel riverbed. Through validation of the porosity, surface roughness distribution and surface roughness spectra against the literature this study shows that both a physical and a numerical riverbed can be successfully generated based on the methodology presented here. The artificial riverbed has a porosity of 31.5% and the numerical riverbed has a porosity of 32.5%. The Hurst exponent, a key indicator of roughness, was found to be 0.97 for the artificial riverbed, 1.4330 for a coarse resolution version of the numerical riverbed, and 1.4305 for a fine resolution version of the numerical riverbed. To further understand the distribution of Turbulent Kinetic Energy (TKE) in the near-bed region of a porous roughness surface, two LES cases at disparate resolutions were also undertaken as part of this study. Streamwise TKE budget components contribute significantly to the overall TKE compared to the spanwise components. This study also shows that with increased elevation away from the bed surface, the magnitude and thus, contribution to TKE of the flow field declines. The shear production, wake production, vertical diffusion transport, pressure transport TKE budget terms were found to be significant both in the near-bed region as well as within the uppermost 2 layers of the riverbed geometry.

Contents

---

[1] Results from this chapter are directly adopted from the first journal paper listed in the section of related publications.

[2] The methodology presented in this chapter is directly adopted from the first journal paper listed in the section of related publications.

Related Publications

The publications derived from the research undertaken in this thesis are listed as follows:

Journal Papers

1. **Stubbs, A**. Stoesser, T. Bockelmann-Evans, B. 2018. Developing an approximation of a natural, rough gravel riverbed both physically and numerically. Geosciences 8 (12), p. 449. doi: 10.3390/geosciences8120449.

Conference Papers

1. Nassrullah, S. **Stubbs, A**. Stoesser, T. Wilson, C.A. 2019. The validation of the logarithmic velocity profiles above rough-bed flows. 38th IAHR World Congress, September 1-6, Panama City, Panama. doi: 10.3850/38WC092019-0421.

Nomenclature

Abbreviations

2D	Two-dimensional
3D	Three-dimensional
ADV	Acoustic Doppler Velocimetry
CAD	Computer Aided Design
CFD	Computational Fluid Dynamics
CFL	Courant-Friedrichs-Lewy condition
CNC	Computer Numerical Control
DA	Double Averaged
DNS	Direct Numerical Simulation
EL	Eulerian-Lagrangian
EPIV	Echo PIV, not to be confused with Endoscopic PIV
ET	Eddy Turnover
FT	Flow Through
IB	Immersed Boundary
IBM	Immersed Boundary Method
LDV	Laser Doppler Velocimetry
LES	Large Eddy Simulation
LSM	Level-Set Method
LSV	Laser Surface Velocimetry
MDF	Multi-Direct Forcing
MPI	Message Passing Interface
OpenMP	Open Multi-Processing
PG	Probe Group
PSD	Power Spectral Density
PTV	Particle Tracking Velocimetry
PIV	Particle Image Velocimetry
RANS	Reynolds Averaged Navier-Stokes
RIM	Refraction Index Matching
SGS	Sub-Grid Scale
TKE	Turbulent Kinetic Energy
VLSM	Very Large-Scale Motion

Dimensionless parameters

Fr Froude number

Re Reynolds number

Re_D Roughness Reynolds number

Re_F Friction Reynolds number

Re_K Permeability Reynolds number

Greek Symbols

δ Interpolating delta function

ν Kinematic viscosity

μ Dynamic viscosity

∂ Indicates partial derivation operation

φ Kernel function

π Number pi

ρ_p Particle density

ρ Fluid density

σ_z Standard deviation

τ Shear stress

ε Dissipation

κ Von Karman's constant

Roman Symbols

d Particle diameter

D_d Kinematic eddy diffusivity

h Flow depth

H Hurst exponent

F Lagrangian force

f Eulerian force

F_{ku} Streamwise TKE flux

F_{kw} Wall-normal TKE flux

I Turbulence intensity

K Permeability

k Turbulent kinetic energy

N Matrix of node coordinates

p Pressure

P_s Shear production

P_m	Work of the bed induced velocity fluctuation against DA shear stress
P_w	Wake production
$R_{\partial u_i}$	Correlation coefficient of spatial and temporal derivatives in the component directions
Sk_z	Skewness
Ku_z	Kurtosis
t	Time
T_D	Vertical diffusion transport
T_w	Form-induced diffusion transport
T_p	Pressure Transport
T_v	Viscous transport
g	Gravitational acceleration, taken here to be 9.81 m/s^2
U	Lagrangian marker velocity
u	Eulerian velocity
U_*	Forced Lagrangian velocity
u_*	Eulerian friction velocity
U_{cu_i}	Convective velocities in the component directions
V	Volume
w_s	Settling velocity
X	Lagrangian coordinates
x	Eulerian coordinate
z_0	Zero-plane displacement

Superscripts

$(\cdot)'$	Fluctuation value
$(\cdot)^+$	Normalised variable
$(\overline{\cdot})$	Time-averaged variable
$\langle \cdot \rangle$	Spatially averaged variable
$\langle \overline{\cdot} \rangle$	Double averaged variable

Subscripts

$(\cdot)_L$	Referred to Lagrangian marker
$(\cdot)_{RMS}$	Root Mean Square error
$(\cdot)_{i,j,k}$	Referred to component in the x, y, or z-direction

List of Figures

List of Tables

Chapter 1

1. Introduction

1.1. Motivation

When first approaching the issue of what to specifically investigate within the broad and far-reaching field of fluid dynamics a wide, brief, review of riverine processes in general was undertaken. This review included sediment transport processes, such as traction and suspension, hydrodynamic phenomena, such as near-bed and interstitial turbulence, the linkage between groundwater and surface water flows, as well as an overview of the riverine ecosystem focusing on salmonids and the movement of dissolved oxygen and nutrients upon which they depend. By undertaking this review, though brief, it became clear that many, if not all, of these processes are driven by turbulent flow phenomena and though much research over several decades has provided a far greater understanding of the physics behind such phenomena, there is still much that requires further investigation and quantification to be fully understood and accepted. Therefore, this study focuses upon near-bed and interstitial turbulent flow behaviors within the riverine environment.

The grain size and distribution of particles forming a gravel riverbed determine its roughness, which drives near-bed turbulence (Aberle, 2007; Nield and Bejan, 2017; and Stoesser, 2010) as well as in-bed microscopic pore turbulence. The roughness of the riverbed and its pore structure are both paramount factors driving and affecting near-bed turbulence structures as well as the hydrodynamic and transport processes within the pore spaces of the riverbed itself.

Pore space turbulence is believed to consist of pulsating jets whose direction and intensity depend on the Froude number of the interstitial flow (Blois et al.

2012). Microscopic turbulent flow distorts interstitial fluid velocities which under laminar flow conditions has streamlines that tend to the horizontal axis, whereas under turbulent flow conditions has streamlines that tend towards the vertical. As interstitial flow becomes increasingly turbulent due to these jets, the inertial effects on fluid particles are enhanced, further amplifying the development of turbulent flows within the pore space. Therefore, it is essential to first understand turbulence and its occurrence in the form of large-scale energetic structures in the near-bed region before quantifying interstitial turbulence.

Many studies have empirically defined near-bed turbulence, but few have provided a quantitative definition. However, with recent advances in technology, there has been a resurgence in interest in exploring near-bed turbulence. Such studies, either experimental or numerical in nature, are divided into two main categories: those investigating turbulent flows over permeable beds (Dark, 2017; Goharzadeh et al. 2005; Panah and Blanchette, 2018; Goyeau et al. 2003; Khalili et al. 1999; Pokrajac and Manes, 2009; and Morad and Khalili, 2009) and those exploring flows over impermeable beds (Stewart et al. 2018; Aberle and Nikora, 2006; Anderson and Meneveau, 2011; and Barros et al. 2018); both have limitations.

Those investigating only impermeable surface roughness effects on turbulence experimentally often use solid plates that are placed within a flume. Such investigations then employ either Particle-Tracking Velocimetry (PTV) or Particle Image Velocimetry (PIV) to determine the near-bed velocities, and in turn the turbulence. Similarly, those numerically investigating the influence of impermeable roughness on turbulence typically generate a series of roughness elements, such as bars, hemispheres, dunes, or fractals, that are placed on the bottom of the computational domain to represent a rough surface (Bomminayuni and Stoesser (2011); Stoesser and Nikora (2008); McSherry et al. (2018); Cameron et al. (2017); and Singh et al. (2007)). Some have gone to great lengths to generate highly complex roughness surfaces using technologies such as photogrammetry or through mathematical definitions (McSherry et al. 2017; and Alfonsi et al. 2020) which are far more representative of the surface of a natural riverbed. However, whether using solid plates, or roughness elements or surfaces, to define the roughness geometry of a riverbed, no account can be made for the effect that processes associated with a porous bed, like turbulent bursting, might have on near-bed turbulence. Thus, turbulence in these cases is driven entirely by the shear stress arising from the roughness geometry that is used. This may well describe macroscale near-bed turbulence with some accuracy, but as others (Blois et al. 2012; Valyrakis

et al. 2013; and Stoesser, 2008) have pointed out, the microscale turbulence might have a far greater impact on the macroscale than previously understood and this can only be taken into account by looking at the bed matrix as a whole.

For those exploring the particle bed matrix as a whole, a different set of limitations exist. Generally, in experimental studies of this type, spherical elements are placed within a flume in a grid-like pattern (e.g. Blois et al. (2012); Kim et al. (2020); Pokrajac and Manes (2009); and Manes et al. (2009)) or packed more naturally (e.g. Dark (2017); Khalili et al. (1999); and Morad and Khalili (2009)), and again, PTV or PIV are used to determine both the near-bed and pore velocities. Similarly, in numerical studies looking at permeable beds, it is typical for unimodal or bimodal spherical particles to be placed, again in grid-like patterns, within the computational domain (e.g. Fang et al. (2018); and Shen et al. (2020)). Such simplistic representations of a particle bed matrix are often employed as they are relatively straightforward to represent numerically. Thus, allowing an accurate approximation of the desired matrix as well as reduced computational demand.

Whether the study is experimental or numerical, using regularised bed matrixes, in terms of both shape and volume, results in a reduced pressure differential between pores than would necessarily be found naturally. Therefore, any observed turbulent bursting, although present in such studies, does not necessarily reflect that seen over natural gravel. There is a clear need to move away from simplistic geometry towards more accurate, or representative, gravel-like permeable beds to further understand the effects of permeability on turbulent flow phenomena.

In addition to the difficulties in accurately representing a natural gravel riverbed, computationally, there is also an added difficulty of accurately approximating highly complex turbulent flows. As Stoesser (2010) points out, until recently, most numerical studies were based on the Reynolds-Averaged Navier–Stokes (RANS) equations, which are driven by empirically-derived roughness functions, and thus, have had limited success in modelling highly turbulent near-bed flow. The computational approaches of Direct Numerical Simulation (DNS) and Large-Eddy Simulation (LES) differ substantially to the RANS approach. In DNS all scales of fluid motion are fully resolved providing a flow field entirely simulated using physics equations for fluid motion. The LES approach sits between RANS and DNS whereby larger scales of fluid motion are fully resolved, like DNS, but the effects of small-scale fluid motion on the wider flow field are modelled in a fashion like that employed in the RANS approach. Both DNS and LES require far greater computational effort than RANS, but with advances in computing hardware, DNS

and LES approaches have recently made great strides using rough geometry boundaries.

Although there has been a move from modelling towards simulation resulting in highly turbulent flow being much better represented, particularly in the near-bed region, the roughness geometry typically being employed has remained simplistic.

1.2. Research Aims and Objectives

This study first aims to design and manufacture an artificial representation of a gravel riverbed matrix with the goal of providing a validated means of manufacturing porous roughness geometry with pre-determined characteristics for the purposes of physical experimentation. Analysis will determine how well such geometry represents a natural riverbed in terms of particle size distribution, surface roughness, and porosity in comparison with both artificial and natural riverbeds, as reported in the literature to date.

Secondly, this study aims to develop a complementary numerical representation of a gravel riverbed matrix for use with the Immersed Boundary Method (IBM) employed by the in-house Large Eddy Simulation (LES) code Hydro3D (Ouro and Stoesser, 2017). In doing so, this study will provide a validated methodology for numerically representing not only roughness geometry, but other highly complex bodies for investigation through numerical simulation. Analysis will determine to what degree the process of creating a numerical representation of a complex body alters the geometry compared to that originally intended. Further analysis will also be undertaken to determine the roughness characteristics of the numerical representation of a gravel riverbed in comparison to the literature to date.

Lastly, this study aims to further explore near-bed and interstitial turbulent flows associated with porous media through numerical simulation using the LES code Hydro3D (Ouro and Stoesser, 2017) with the goal of quantifying the effects of porosity and roughness on such flows. Statistical analysis will be presented by means of velocity profiles, Reynolds normal and shear stresses, turbulence intensities, skewness and kurtosis, and wavenumber spectra to validate this study against the wider literature to date. An in-depth analysis of the vertical distribution of Turbulent Kinetic Energy (TKE), the streamwise and spanwise TKE fluxes, and the TKE budget terms in both streamwise and spanwise directions will also be undertaken. The aim of exploring the TKE both above and within a porous roughness

surface is to further understand the effects of topography, porosity, and flow conditions on TKE and the associated turbulent flow phenomena.

1.3. Outline of Thesis

The structure of this thesis is as follows:

- Chapter 2: A review of existing literature is presented on the research topic of gravel riverbed hydraulics (Section 2.1), the experimental approach to near-bed turbulence (Section 2.2), the numerical approach to near-bed turbulence (Section 2.3), and the double averaging methodology (Section 2.4), before an overview (Section 2.5) is presented.

- Chapter 3: Provides a description of the governing equations and mathematical framework behind the large eddy simulation employed in this study by providing background on the different computational fluid dynamic approaches (Section 3.1), detailing the Navier-Stokes Equations (Section 3.2), showing the methodology behind the fractional-step method (Section 3.3), before finally providing details of the immersed boundary method (Section 3.4).

- Chapter 4: Presents a novel methodology for the design and manufacture of a physical representation of a gravel riverbed by first outlining the aims and objectives of the chapter (Section 4.1), providing detail on the CAD model development (Section 4.2), discussing design and manufacturing decisions and methods (Section 4.3), analysing the porosity and roughness characteristics of the artificial riverbed in comparison with natural gravel riverbed (Section 4.4), very briefly outlining the experimental methodology conducted by others using the artificial bed designed in this study, for completeness only (Section 4.5), before finally providing a summary of the findings of Chapter 4 (Section 4.6).

- Chapter 5: Explores a novel methodology for the design and generation of a numerical representation of a gravel riverbed by first outlining the aims and objectives of the chapter (Section 5.1), presenting details and options for the CAD model development (Section 5.2), introducing the Gmsh2Hydro3D methodology for obtaining a nodal point cloud representation of a complex geometry model ready for use with the immersed boundary method, as well as determining the degree of representation provided by the methodology (Section 5.3), analysing the porosity and roughness characteristics of the generated

numerical riverbed (Section 5.4), before finally providing a summary of the findings of the chapter (Section 5.5).

- Chapter 6: Investigates, using large eddy simulation, the near-bed and interstitial flows of the previously developed numerical riverbed by first providing the aims and objectives of the chapter (Section 6.1), giving details on the numerical setup of the simulations and the bulk flow conditions, as well as the initialisation inputs (Section 6.2), providing an in-depth analysis of the mean flow statistics, spectral analysis, mean turbulent kinetic energy, turbulent kinetic energy flux, and turbulent kinetic energy budget (Section 6.3), before summarising the findings of this chapter (Section 6.4).

- Chapter 7: Conclusions of the thesis, contributions and future research are all outlined in this chapter.

Chapter 2

2. Literature Review

2.1. Gravel Riverbed Hydraulics

2.1.1. Channel Flows

Open channel flows are fluid flows that have a free surface subject to atmospheric pressure; streams and rivers are considered types of open channel flow. Such flows differ considerably to confined flows such as that within a pipe which are mainly driven by pressure as opposed to gravity.

Turbulence within open channel flows is the main driver in many riverine exchange and transport mechanisms which are critical to the ecology of river systems and the wider environment. All benthic life depends on the exchange of dissolved oxygen and nutrients between the channel and the riverbed which is driven by turbulence. The dispersal of pollutants that enter the channel and can damage the ecosystem are also driven by turbulent eddies. The transport of sediment through suspension as well as traction is also dependent upon turbulent flow phenomena as is the formation of bedforms such as riffles and dunes which are important habitats for juvenile fish.

Turbulent flow is where fluid particles behave in a seemingly chaotic manner in all three-dimensions with irregular fluctuations, or instabilities, where the velocity of fluid particles at a given point in space changes in both magnitude and direction with time. Such flow is governed by high momentum convection and low momentum diffusion.

Turbulent eddies emerge within a flow field due to drag forces acting on the fluid as it interacts with boundaries, such as a gravel bed or bridge piers in the case

or a river or stream. Within the near-bed region of flows over a gravel riverbed turbulent flow phenomena known as turbulent bursting occurs.

Turbulent bursting consists of quasi-periodic ejections of low momentum fluid from the riverbed and sweeps of high momentum fluid towards the riverbed (Zhong et al. 2011; Cao, 1997; Nino and Garcia, 1996; Grass, 1971; Kline et al. 1967, Dwivedi et al. 2010 and Sutherland, 1967). Sutherland (1967) theorised that the ejection of low momentum fluid from the bed causes turbulent eddies to form near the bed which disrupts the viscous sublayer. The disruption causes an increase in local shear stress within the viscous sublayer beyond that arising due to the interaction of fluid with the roughness surface itself.

Nino and Garcia (1996) go further and suggest that instead of eddy's disrupting flow in the viscous sublayer, the ejections of low momentum fluid create coherent structures, often referred to as streaks in the literature, made up of layers of turbulent shear flow with concentrated spanwise vorticity.

Since the incidence of ejections is dependent on shear stress and bed roughness drives shear stress, changes in the bed surface, such as by the infilling of deposited particles, can not only reduce the roughness and porosity of the surface, but also the shear stress and turbulent kinetic energy (Nino and Garcia, 1996 and Sambrook-Smith and Nicholas, 2005). However, that is not to say that turbulent bursting ceases to occur, more that it is modified and in fact continues irrespective of roughness (Zhong et al. 2011 and Cao, 1997). This is an interesting observation as this would suggest that irrespective of whether a bed is permeable or impermeable, or has a different roughness, similar turbulent phenomena within the near-bed region will occur, but with different magnitude and incidence. This is an area requiring much further investigation. Nino and Garcia (1996) also highlight that though this theory of turbulent bursting holds true for Reynolds numbers less than 3×10^4, for higher Reynolds, a different set of events may occur and requires exploration.

Open channel flows can be classified by the ratio of flow depth to roughness particle diameter, or the relative submergence. The relative submergence of a flow is key to appreciating how bed generated turbulence interacts with the free surface and vice-versa. For flows of high relative submergence, interaction between bed turbulence and the surface may be absent, or certainly minimal (Singha and Balachandar, 2010). However, for flow of intermediate or low relative submergence, bed induced turbulence interacts with the free-surface, and vice-versa, and significantly increases the complexity in trying to understand such flows further.

Pan and Banerjee (1995) classified such bed-surface interactions as vortices, upwelling, and downdraft dependent upon the characteristic driving velocity. Surface-normal vortical structures exist where the ratio of surface-normal to surface-parallel velocities tends to zero. Upwelling structures are where high magnitude surface-normal velocity with an upwards trajectory disrupts streamwise streamlines within the water column. Conversely, downdraft structures are where surface-normal velocity with a downwards trajectory projects from the free-surface and effectively disperses the effects of any upwelling. The pattern of upwelling, vortical development, and downdraft that exists within channel flows of low and intermediate relative submergence plays an important part in redistributing the turbulent kinetic energy of the flow (Singha and Balachandar, 2010). Within the surface layer itself, surface-normal and surface-parallel vortex tubes drive free-surface deformations (in the absence of wind induced stress) (Weigard and Gharib, 1995)

Flows of high relative submergence have been extensively studied, but it has only been relatively recently that there has been a push to investigate flows of intermediate and low relative submergence with a focus on turbulent flow phenomena throughout the entire water column across all scales (Nikora et al. 2019; Manes et al. 2009; Ferraro et al. 2016; McSherry et al. 2018; and Blois et al. 2012). A fully quantitative understanding of the interactions between bed induced turbulent phenomena and the free surface presently eludes researchers.

2.1.2. Interstitial Flow

The study of fluid flow through porous media has interested researchers since the 1850's. Stuart (1953) showed that flow enters a gravel layer at right angles to the surface and is driven by the hydraulic gradient between the upstream and downstream faces of a bedform, such as a pool or riffle. This pressure difference is not dissimilar to that caused by airflow over a wing or fluid flow around a cylinder (Thibodeaux and Boyle, 1987). Thibodeaux and Boyle (1987) further add that without bedforms, a pressure imbalance still exists over some distance due to differences in temperature, water density and hydrostatic pressure.

Darcy's Law describes fluid flow through porous media which is driven by a hydraulic gradient (Bear, 2007)

$$Q = KA(h_1 - h_2)/L \tag{2.1}$$

where, Q is discharge, A is the area occupied by fluid, K is the coefficient of proportionality, h_1 and h_2 are lengths measured with respect to some datum and L is the filter length.

Eq. (2.26) gives a linear relationship between fluid velocity and hydraulic gradient due to the following assumptions:

> (1) Fully saturated porous media of medium-sized sand; (2) constant temperature; (3) inert porous media; (4) stable sand bed; (5) flow under medium-range gradients; and (6) steady-state laminar flow (Soni et al. 1978, p. 231)

Many researchers have applied Darcy's Law for simplicity in describing interstitial flow (Tonina and Buffington, 2007; and Soni et al. 1978). However, it is well established that under high and low hydraulic gradients, Darcy's Law is not applicable and instead the empirical equations developed by Izbash (1931), cited in Soni et al. (1978, p. 232), and Forchheimer (1901), cited in Takhanov (2011, p.2), are often applied to non-Darcian flow regimes, as shown in Fig. 2.1. Zhou and Mendoza (1993) offer an alternate equation to Forchheimer (1901), cited in Takhanov (2011, p.2), where variations in velocity through the bed as well as shear at the bed are also considered.

$$J = C_1 q + C_2 q^2 \qquad\qquad\qquad (2.2)$$

where, J is hydraulic gradient, C_1 and C_2 are experimentally derived constants and q is mean bulk velocity averaged over thickness of porous layer.

Flow non-linearity occurs within the riverbed due to the presence of microscopic turbulence within the pore space of the sediment matrix (Zhou and Mendoza, 1993). This turbulent flow distorts the fluid velocity streamlines, as shown in Fig. 2.2, by enhancing the effects of inertia on fluid particles (Zhou and Mendoza, 1993).

It is the formation of coherent structures and the phenomenon of turbulent bursting that causes pressure fluctuations within the riverbed that leads to the development of micro-scale turbulence. (Vollmer and Kleinhans, 2007; Stoesser and Rodi, 2007; Goharzadeh et al, 2005; Blois et al, 2012; Carling et al, 2006; Packman et al, 2000 and Elliott and Brooks, 1997). Microscopic turbulent flow consists of pulsating jets within the pore spaces of a gravel riverbed matrix. These microscopic

jets have been found (Blois et al, 2012) to change direction and intensity with changes in the Froude number of the overlying channel flow; a reduction in Froude number results in a decrease in turbulent intensity and the interstitial flow tends towards laminar. With increased depth into the riverbed interstitial flow tends towards laminar (Zhou and Mendoza, 1993). The direction of flow through any given pore space depends upon which flow condition is dominating; turbulent jets result in horizontal flow whilst laminar conditions result in vertical flow.
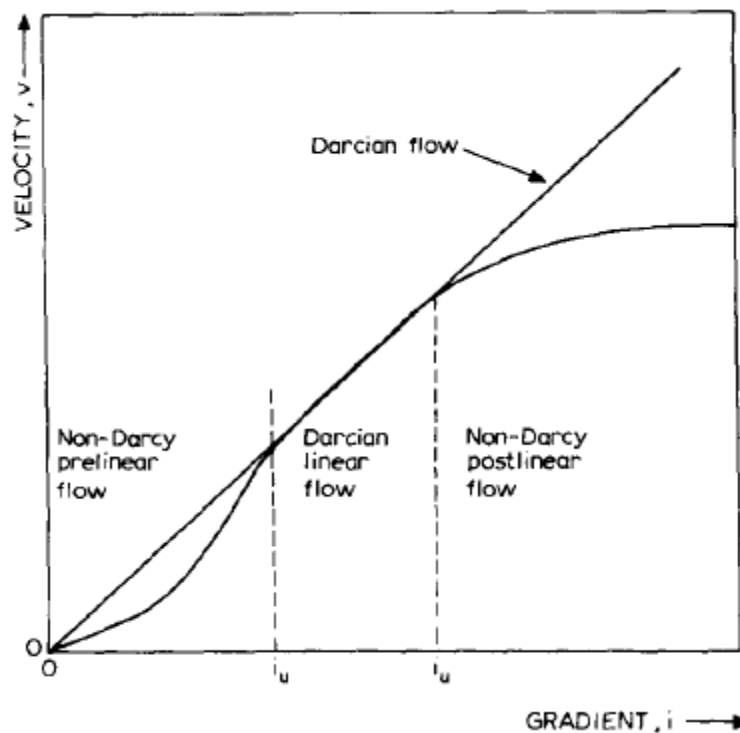
Figure. 2.1. Non-Darcian velocity-gradient relationship, figure taken from Soni et al. (1978, p. 232).

All the literature talked about so far has assumed that the riverbed is fully saturated. However, if "the rate at which water is transmitted through a sediment exceeds the rate at which it enters" (van't Woudt and Nicolle 1978, p. 115) then negative pressure will develop allowing air to enter the system leading to an unsaturated riverbed. Though the observations by van't Woudt and Nicolle (1978) cannot be denied, so long as the hydrostatic pressure above the bed is sufficient and given that channel flow tends to be far greater than interstitial flow, even if conditions facilitated the development of negative bed pressures, they could not result in air accumulation within the pore space. Therefore, the assumption that riverbeds are fully saturated is reasonable.

11
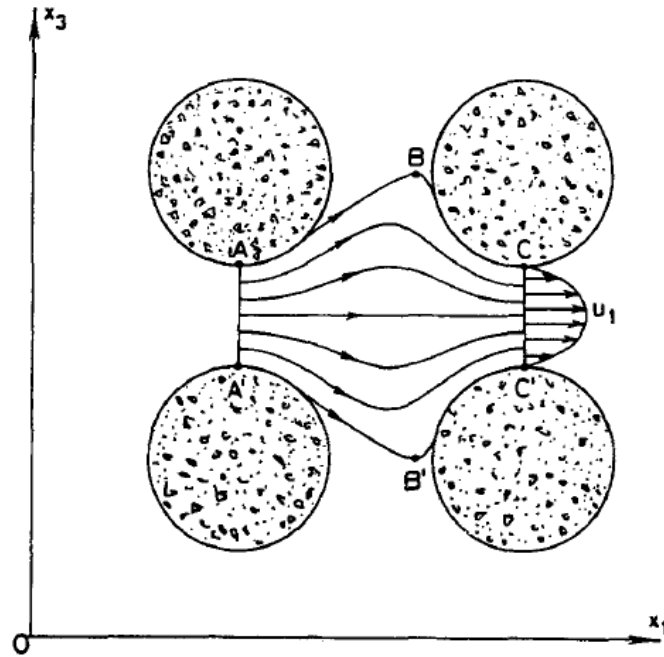
Figure 2.2. Idealised pore space velocity streamlines influenced by the effects of inertia, figure taken from Zhou and Mendoza (1993, p. 368).

It is clear from the literature that the relationship between channel and interstitial flow as well as interstitial flow itself is well understood at the macro-scale. However, it is only with recent advances in technology that an understanding of the micro-scale is beginning to be formed which is essential to the validation of existing theory for macroscopic flows within the riverbed (Blois et al, 2012).

There is a distinct lack of literature on the physical quantification of interstitial flows, specifically at the microscopic scale, as well as the drivers behind channel-bed flux in the near-bed region.

2.2. Experimental Approach to Near-bed Turbulence

Researchers have approached the experimental evaluation of near-bed turbulence in numerous different ways, each with their own limitations, benefits, and successes.

Few researchers have engaged in field studies of near-bed turbulence. This is mainly due to the practical difficulties of gaining access and taking precise and accurate velocity measurements within a river. However, it is also due to a need to limit the scope of a study and thus, introduce more controls to allow determination of a single characteristic of near-bed turbulence rather than numerous, inter-linked and inter-dependant characteristics. Most researchers have therefore conducted

12

laboratory experiments to describe some element(s) of near-bed turbulence. Such laboratory experiments often consist of a recirculating flume of varying length and width and a flume bed consisting of roughness elements to generate the required, highly turbulent flow. All laboratory-based research of this nature falls into two categories depending on whether the roughness elements are permeable or impermeable.

Researchers investigating flows over impermeable surfaces often use artificial roughness elements to represent the surface of natural gravel riverbeds. With recent advances in manufacturing technology such as 3D-printing (Fee, 2017) and advanced 5-axis CNC machining, as well as with more conventional manufacturing methods of casting and moulding (Buffin-Belanger et al. 2003), the options for creating impermeable roughness surfaces with specific roughness characteristics are endless and relatively simple to manufacture. Roughness surfaces made up of bars (McSherry et al. 2018), hemispheres, cubes (Rouzes et al. 2018), and fractals (Nikora et al. 2019) have all been successfully employed to investigate specific aspects of turbulent flows.

However, with non-porous roughness surfaces, no account can be made for the effect that turbulent bursting has on near-bed turbulence. Thus, turbulence in these cases is driven entirely by the shear stress arising from the roughness geometry that is used. This may well describe macroscale near-bed turbulence with some accuracy, but as others such as Blois et al. (2012), Valyrakis et al. (2013), and Stoesser (2008) have pointed out, the microscale turbulence might have a far greater impact on the macroscale than previously understood.

Permeable, or porous, roughness surfaces consist of numerous roughness elements that when placed in a flume create a representation of a gravel riverbed matrix. As such, these surfaces contain voids and the influence of interstitial flow and turbulent bursting phenomena upon macroscale turbulent flow can be investigated. Those researchers requiring a permeable roughness surface often employ natural gravels of varying diameter. Most studies use gravel with unimodal size to represent a natural gravel riverbed. Other researchers use gravel with a bimodal size in an effort to better represent a natural riverbed and thus, also obtain more realistic turbulent flow characteristics. Few researchers have used truly heterogeneous gravels (Hardy et al. 2009 or Ferraro et al. 2016).

Many researchers (Cameron et al. 2017; Dark, 2017; Manes et al. 2009; Kim et al. 2019; Pokrajac and Manes, 2009; and Blois et al. 2012) have also successfully used spherical artificial elements of uniform diameter. However, when packed to

form a matrix the pore space, especially once the elements are water-worked, becomes regularized in both shape and volume. This results in interstitial flow that has a reduced pressure differential between pores. Therefore, any observed turbulent bursting, although present in such studies, does not necessarily reflect that seen over natural gravel. This limitation is further enhanced when roughness elements are stacked, where particles are both horizontally and vertically aligned and placed on top of one another in a cubic grid-like pattern (e.g. Cameron et al. 2017), rather than packed, where particles are placed in triangular, or hexagonal patterns (e.g. Manes et al. 2009 or Kim et al. 2020), which naturally enhances the lack of variability in the pore space shape and volume. Additionally, the overall surface of such roughness elements is often far less rough than desirable to truly represent the roughness of a natural gravel riverbed, and to also generate highly turbulent flow. Very few researchers have successfully managed to combine a naturalistic pore matrix structure with a naturalistic roughness surface through artificial means. However, the benefits of doing so are clear in the obtained results and drawn conclusions.

Regardless of whether using permeable- or impermeable roughness elements in the field, or in the laboratory; experimental velocity measurements can be gathered using different techniques.

Acoustic Doppler Velocimetry (ADV) uses a probe of between two and four receivers submerged within the fluid flow to sample a given volume and provides the velocity of fluid particles based upon the Doppler shift effect. Similarly, Laser Doppler Velocimetry (LDV) also uses the Doppler shift effect to measure the velocity of fluid particles passing through a laser beam.

Particle Image Velocimetry (PIV) and Particle Tracking Velocimetry (PTV) techniques capture the overall flow field by taking images of dilute tracer particles that are illuminated by a suitable light source. The difference between PIV and PTV is that PIV is based on a Eulerian measurement field represented as a function of position and time, as opposed to PTV which is based upon a Lagrangian measurement field, where tracer particles are tracked as they move through space and time. Conventional PIV systems use only one camera to provide velocities in two-component directions. However, by using 2 or more cameras, stereoscopic PIV allows velocities in all three-component directions to be obtained.

Endoscopic PIV, not to be confused with the often similarly abbreviated Echo PIV (EPIV), uses the same principle of conventional external PIV systems, but utilises small viewing ports in the sides or bottom of the flume walls to gain internal velocity

measurements. Such systems have proven very successful in providing insight into pore-space microscopic turbulent flow. Echo PIV (EPIV) systems use ultrasonic pulses emitted from medical ultrasound machines to measure the echo displacement of reflections, relative to the two probes, from tracer particles to determine fluid velocity. This technique is primarily used for measurements within pipes or opaque fluid flows where optical measurement techniques such as PTV, PIV, and Endoscopic PIV cannot be used. However, EPIV does offer an alternative non-intrusive method for obtaining fluid velocity measurements.

Laser Surface Velocimetry (LSV) uses an optical speed sensor to measure the velocity of a moving surface. Though designed for use in the manufacturing industry, this technique could potentially provide highly accurate fluid surface velocity measurements that could be useful for the validation of other measurement techniques, or where fluctuations in the fluid surface, like in the case of highly turbulent, deep-water flow, might cause a problem for conventional measurement techniques.

Great strides have recently also been made in the development of methodologies to overcome the issue of invasive measurement techniques through the combination of PIV systems and RIM techniques (Dark, 2017; Blois et al. 2012; and Blois et al. 2020).

Most of the recent near-bed turbulence experimentation has been conducted using PIV systems. This is because such systems are non-intrusive and yet, relatively attainable in terms of both cost and setup requirements. That being said, ADV systems remain popular due to their availability and ease of use. Interestingly, little or no evidence is provided by the literature on the affect such intrusive systems might have on microscopic turbulent phenomena, and thus, also any inferred effect on macroscopic turbulent behaviour.

2.3. Numerical Approach to Near-bed Turbulence

Like the experimental approaches described in Section 2.2, researchers have numerically investigated near-bed turbulence in many ways. However, regardless of the computational techniques employed to simulate fluid flow, the generation and propagation of turbulent flow is either due to a roughness function or geometry placed within the fluid domain.

Researchers have used many different techniques to create numerical roughness elements and surfaces with varying degrees of basis on natural gravel riverbeds. All

techniques do however fall into two categories: namely, porous- and nonporous-surfaces.

Non-porous geometry is often simplistic and consists of various regularised three-dimensional shapes (eg: hemispheres, cuboids, bars, etc) placed on the bed of the fluid domain (Bomminayuni and Stoesser, 2011 and Fang et al. 2018). Such shapes are useful as they can easily be mathematically described and thus, are relatively simple to model within the fluid domain. However, highly complex non-porous geometry is also used whereby a power-spectral density function is used to generate a roughness surface within the fluid domain (Nikora et al. 2019). Equally, photogrammetry and laser scanning techniques have enabled the numerical use of natural gravel bed surfaces (Alfonsi et al. 2020). This kind of complex roughness surface offers far greater geometric variance over simplistic three-dimensional shapes. Therefore, the resulting turbulent flows are more comparable with that found above natural gravel-bed rivers. However, as simple, or complex as these geometries are, they are still non-porous and therefore, no account can be made for the effects of interstitial flow or turbulent bursting phenomena.

Some researchers have therefore instead chosen to create porous geometry within their fluid domain. Like the experimental approach, described in Section 2.2, of packing or stacking unimodally sized spheres to create a porous roughness surface, researchers have numerically created a roughness matrix formed of uniform spheres (Fang et al. 2018; Han et al. 2015; Fukuda and Fukuoka, 2019; Bartzke et al. 2016; and Lian et al. 2019). Equally, arrays of cubic cylinders have also be applied (Kuwahara et al. 2006) to create a porous roughness matrix. Simplified roughness geometry has been used by many studies as numerical representation is relatively straightforward. This allows an accurate approximation of the roughness geometry in computational simulations as well as reducing the computational expense. However, like the experimental approaches described in Section 2.2, the same set of limitations of a lack of pore space variability and low surface roughness are present in such numerical studies. A few researchers have therefore generated highly complex porous roughness surfaces (Baker, 2011), but this is far from the norm. The resulting insight gained into near-bed turbulence clearly validates the effort required in developing geometry this complex. However, the complex nature of such simulations is a problem in of itself, as has already been found in Section 2.2, few field or laboratory data sets exist of flow above highly naturalistic porous roughness surfaces for verification and validation purposes.

Aside from the method adopted for the generation and propagation of turbulence within the fluid domain, the size of the domain and the resolution of the fluid solver mesh employed by researchers varies considerably.

The idealised fluid domain size of $2\pi h \cdot \pi h \cdot h$ where, h is the flow depth, is often considered large enough to capture all scales of turbulent motion within the domain (Bomminayuni and Stoesser, 2011). However, this idealised criterion is somewhat misleading as it applies to flows above smooth beds as opposed to flows above rough beds. It is now understood within the experimental research field that large scale and very large-scale turbulent motions greatly exceed such dimensional criterion (Cameron et al. 2017) and yet, this does not appear to be reflected within the numerical research field given the relatively small sized domain being widely utilised at present. This is likely due to the current limitations of available computational resource that still play a large role in the determination of domain size and grid resolution for any given study. The chosen numerical approach to the fluid-structure interaction, through implementation of techniques such as the Immersed Boundary Method (Peskin, 1972), as well as the treatment of the free-surface, through rigid-lid approximation or by using an approach such as the Level-Set Method (Osher and Sethian, 1988), must also be considered when determining the domain size and grid resolution as they will further influence the overall computational effort and resource required to conduct any given numerical study.

2.4. Double Averaging Methodology

As turbulent flows are highly three-dimensional and vary in scale from the microscopic to Very Large-Scale Motions (VLSM), conventional Reynolds Averaged Navier-Stokes (RANS) equations are not always appropriate, especially within the proximity of a rough bed. As Nikora et al. (2007) (p.873) remark, "two-dimensional (2D) approximations based on the Reynolds equations, as well as similarity considerations for time-averaged variables, are not possible for the near-bed region in rough-bed flows." The Double Averaging (DA) approach of averaging new momentum and continuity equations in both time and space overcomes such issues. Additionally, the DA approach provides additional terms, such as form-induced stress, explicitly even within the bed matrix itself which cannot be obtained any other way.

Critical to the DA approach is relating spatial and time derivatives to the volume averaging of instantaneous variables which can be defined as (Nikora et al. 2007):

$$\langle\theta\rangle(x,y,z,t) = \frac{1}{V_f}\int_{V_f}\theta dV \tag{2.3}$$

and

$$\langle\theta\rangle_s(x,y,z,t) = \frac{1}{V_o}\int_{V_f}\theta dV \tag{2.4}$$

where, Eq. 2.3 is the so-called intrinsic spatial average in which, θ is the instantaneous flow variable where $\langle\ \rangle$ denotes spatial averaging, and V_f is the volume occupied by fluid within the total volume V_o; and Eq. 2.4 is the so-called superficial spatial average.

Eq's. 2.3 and 2.4 can also be performed using area averaging (Nikora et al. 2001; and Raupach and Shaw, 1982), but volume averaging allows the same equations to be applied for both channel and interstitial flows. Here the intrinsic spatial average (Eq. 2.3) is utilised. Eq's. 2.3 and 2.4 are related by $\langle\theta\rangle_s = \phi_s\langle\theta\rangle$ where, $\phi_s = \frac{V_f}{V_o}$ can be considered as akin to a roughness geometry function (e.g. Nikora et al. 2001).

Through Reynolds' decomposition of the instantaneous variables into their mean, denoted by the overbar ($\bar{\cdot}$), and instantaneous fluctuating constituents, denoted by the accent ($\cdot'$), as

$$\theta = \bar{\theta} + \theta' \tag{2.5}$$

and with decomposition of the time-averaged variables into their time-space average and form-induced constituents, denoted by the tilde ($\tilde{\cdot}$), as

$$\bar{\theta} = \langle\bar{\theta}\rangle + \tilde{\theta} \tag{2.6}$$

and by assuming that

$$\langle\langle\bar{\theta}\rangle\rangle = \langle\bar{\theta}\rangle \tag{2.7}$$

and

$$\overline{\langle\bar{u_i}\rangle\langle\bar{u_j}\rangle} = \langle\bar{u_i}\rangle\langle\bar{u_j}\rangle \tag{2.8}$$

the DA momentum conservation and continuity equations can be derived from the Navier-Stokes equations as (Nikora et al. 2007)

$$\frac{\partial \langle \overline{u_\iota} \rangle}{\partial t} + \langle \overline{u_\jmath} \rangle \frac{\partial \langle \overline{u_\iota} \rangle}{\partial x_j} = g_i - \frac{1}{\rho \phi} \frac{\partial \phi \langle \overline{p} \rangle}{\partial x_i} - \frac{1}{\phi} \frac{\partial \phi \langle \widetilde{u_\iota} \widetilde{u_\jmath} \rangle}{\partial x_j} - \frac{1}{\phi} \frac{\partial \phi \langle \overline{u_i' u_j'} \rangle}{\partial x_j}$$
$$+ \frac{1}{\phi} \frac{\partial}{\partial x_j} \phi \langle v \frac{\overline{\partial u_\iota}}{\partial x_j} \rangle + \frac{1}{\rho} \frac{1}{\langle \phi_t \rangle} \frac{1}{V_f} \iint\limits_{S_{int}} \overline{p n_\iota dS}^{S}$$
$$- \frac{1}{\langle \phi_t \rangle} \frac{1}{V_f} \iint\limits_{S_{int}} \overline{v \frac{\partial u_\iota}{\partial x_\jmath} n_\jmath dS}^{S}$$

(2.9)

and

$$\langle \overline{\frac{\partial \rho}{\partial t} + \frac{\partial \rho u_\iota}{\partial x_\iota}} \rangle = \rho \frac{\partial \phi}{\partial t} + \rho \frac{\partial \phi \langle \overline{u_\iota} \rangle}{\partial x_i} = 0$$

(2.10)

where, u_i and u_j are the ith components of the velocity vector, g_i is the ith component of the gravitational acceleration, p is the pressure, ρ is the fluid density, v is the kinematic viscosity of the fluid, and t is time.

2.5. Literature Overview

From the literature it is clear that within open-channel flows, such as rivers, turbulence at a macro-scale is generally well understood and has been the focus of much research energy over recent decades. However, channel flows of intermediate and low relative submergence over rough beds still pose many challenges and present opportunities for further understanding. The interaction of bed induced turbulence with the free-surface, and vice-versa, under low relative submergence conditions is receiving much attention both experimentally and numerically at present with findings of such studies offering the most complete picture of turbulence within open-channel flows to date. However, a lack of quantification exists for turbulent flows within the bed matrix, even though such phenomena are conceptually well understood. The study of pore-space, microscopic turbulent phenomena perhaps present the largest challenge to both experimental and numerical studies alike currently due to limitations of non-intrusive measurement techniques and computational affordability.

Both numerical and experimental approaches to the investigation of near-bed turbulence are relatively similar, perhaps as the datasets are used to validate the other's approach, in that they employ bed geometry that is either porous or non-porous and are often a highly simplistic representations of natural gravel riverbed. The bed geometry used can consist of any number of shapes from cubes and bars, to spheres and roughness plates. Much, if not all, of our knowledge and understanding of turbulent near-gravel-bed phenomena comes from such experimental and numerical studies. However, critically, very few truly represent a gravel riverbed in terms of porosity, roughness distribution, roughness heights, particle size, particle packing, or interstitial flowrate. It is therefore apparent that with more realistic bed geometry there is a great potential for furthering understanding of near-bed turbulent processes and even interstitial, microscopic turbulence by some margin.

The DA method offers an approach to time-space averaging of turbulent flows both above and within rough beds through new derivations for the momentum conservation and continuity equations that is more appropriate than the conventional RANS approach. Additionally, the DA approach provides additional terms, such as form-induced stress, explicitly which would be impossible to obtain through other means and can thus offer further insight into turbulent flows than previously possible.

Overall, turbulent flows in open channels are generally well understood, at least conceptually, but quantification of specific phenomena, particularly within the bed matrix, is lacking. Great strides have been recently made to not only provide insight into turbulent flow phenomena itself, but also for the advancement of the tools that could be used in the near-future to improve understanding and allow rigorous quantification at all scales within both the channel and interstitial realms.

Chapter 3

3.   Numerical Framework

3.1. Numerical Simulation

The numerical simulation of unsteady, turbulent, incompressible fluids is performed by resolving the governing Navier-Stokes equations for fluid flow in three-dimensions. However, as turbulent flow is a phenomenon that involves a wide range of scales of fluid motion, this is not necessarily as simple as it might first appear. Researchers have therefore developed numerous different methods for numerically resolving the Navier-Stokes equations with varying degrees of computational demand and basis on the physics of fluid motion.

Direct Numerical Simulation (DNS) allows the Navier-Stokes equations to be fully resolved for all length scales without introducing any turbulence model. Naturally, this makes DNS extremely highly computationally demanding, yet fully deterministic. Whereas the Reynolds-Averaged Navier-Stokes (RANS) approach, through time-averaged filtering, only resolves the Navier-Stokes equations for the mean-flow quantities and stochastically models turbulent fluctuations. Therefore, DNS and RANS represent either end of a spectrum of computational demand versus reliance upon a stochastic model to describe turbulent fluid motion. All other numerical methods fall somewhere on this spectrum between DNS and RANS.

Large Eddy Simulation (LES) sits somewhere near to DNS in terms of high computational demand, yet far enough away to still make it affordable, whilst also not compromising on the accuracy of the overall simulation through selective use of turbulence modelling. Like DNS, LES explicitly calculates the motion of large-scale eddies through resolving the Navier-Stokes equations, as shown in Fig. 3.1. However, unlike DNS, this method then models the effects of the smaller scales of

fluid motion upon the wider flow field, as shown in Fig. 3.1. The assumption here is that the smaller scales are isotropic and thus, easier to model than their more energetic and anisotropic large-scale counterparts. The small-scale turbulent motions are separated from the large eddies through spatial filtering, first introduced by Leonard (1975). The filter width is equal to the grid resolution and the effect of turbulent motions that are smaller in scale than this are modelled using a so-called Sub-Grid Scale (SGS) model, as depicted in Fig. 3.1.
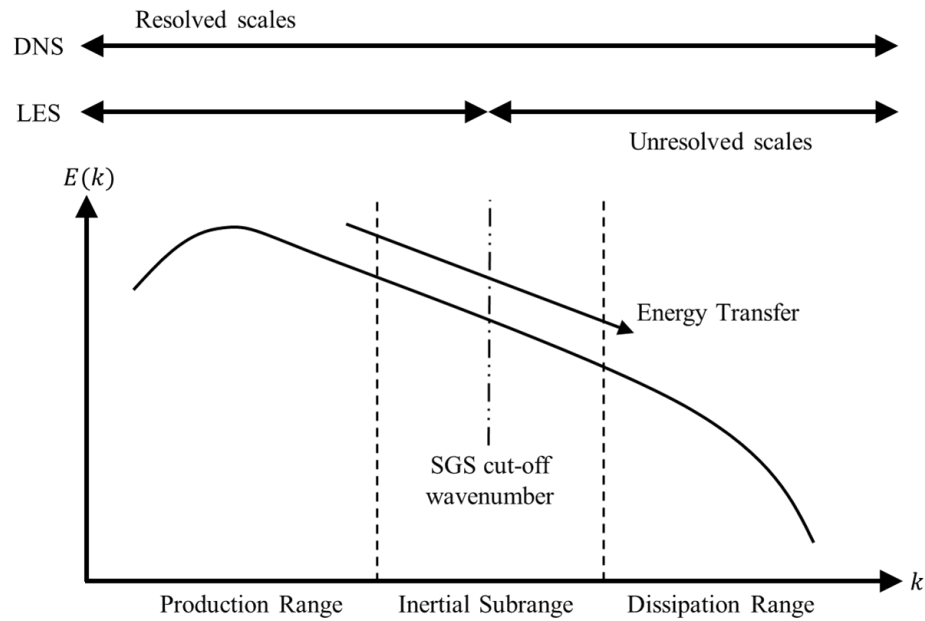
Figure 3.1. Representation of the energy spectrum, highlighting the difference between DNS and LES approaches to resolving eddies at various scales.

As a result of this computational affordability, combined with simulation accuracy, LES has greatly gained in popularity within academia for numerous applications across many research areas. Since this study focuses on flows above naturalistic gravel riverbed, which are dominated by large scale turbulent structures, an LES approach to numerical modelling was adopted as DNS was deemed impractical and RANS insufficient.

3.2. Governing Equations

Numerical modelling undertaken within this study is performed using the in-house LES code, Hydro3D, which has been thoroughly validated for numerous internal and external flows (e.g.: Bomminayuni and Stoesser (2011); Cevheri et al. (2016); Fraga and Stoesser (2016); Fraga et al. (2016); Liu et al. (2016); McSherry

et al. (2018); Ouro et al. (2017); Stoesser (2010); Stoesser and Nikora (2008); Stoesser et al. (2015)).

Hydro3D solves the incompressible, filtered Navier-Stokes equations

$$\frac{\partial u_i}{\partial x_i} = 0 \tag{3.1}$$

$$\frac{\partial u_i}{\partial t} + \frac{\partial u_i u_j}{\partial x_j} = -\frac{\partial p}{\partial x_i} + \nu \frac{\partial^2 u_i}{\partial x_i \partial x_j} - \frac{\partial \tau_{ij}}{\partial x_j} + f_i \tag{3.2}$$

where, x_i (x, y, z for $i = 1,2,3$) and x_j (x, y, z for $j = 1,2,3$) are the spatial location vectors, u_i ($i = 1,2,3$) and u_j ($j = 1,2,3$) are the resolved velocity components in the x- and y-directions, normalised with the reference velocity U, p is the normalised pressure divided by the density, ν is the kinematic viscosity, τ_{ij} is a sub-grid stress tensor, and f_i represents the forcing arising from the Immersed Boundary (IB) method (Uhlmann, 2005), also employed in this study, which is explained in Section 3.4.

The energy cascade, as shown in Fig. 3.1, by definition means that kinetic energy that is extracted from the mean flow at the largest turbulence scales must then be transferred to the smaller scales. LES utilises this to dissipate kinetic energy through the SGS model at the smallest scales to balance the energy balance within the spectral domain (Rodi et al. 2013). Thus, making the choice of the SGS model critical to the performance of the overall simulation. If the SGS model dissipates too much energy, then the increased difference between the resolved and modelled turbulent scales would lead to damping of the resolved scales. Equally, if the SGS models fails to dissipate enough energy, then a build-up of energy would occur at the separation between the resolved and modelled turbulent scales, otherwise called the cut-off wavenumber.

Several different SGS approaches could have been employed in this study, including the Smagorinsky model (Smagorinsky, 1963), One-Equation model (Yoshizawa and Horiuti, 1985), and K-Epsilon model. However, the Wall-Adapting Local Eddy (WALE) viscosity SGS model (Nicoud and Ducros, 1999) was utilised as it is highly suited for use with the IB method also employed. This is because the WALE model can correctly predict the eddy viscosity near solid boundaries, even if they are not sharply defined, as is the case with complex geometries and the IB method. This is not the case for the other SGS models mentioned here which all have near-wall limitations and as such, could not be used in this study.

Within the WALE model, the unresolved velocity fluctuations, accounted for by the sub-grid stress tensor τ_{ij}, can be described as

$$\tau_{ij} = \tau_{ij}^a + \frac{1}{3}\tau_{kk}\delta_{ij} \qquad (3.3)$$

where, δ_{ij} is the Kronecker delta and τ_{ij}^a is the anisotropic sub-grid stress tensor represented as

$$\tau_{ij}^a = -2\upsilon_t \bar{S}_{ij} \qquad (3.4)$$

in which,

$$\upsilon_t = (C_w\Delta)^2 \frac{(S_{ij}^d S_{ij}^d)^{3/2}}{(\bar{S}_{ij}\bar{S}_{ij})^{5/2}+(S_{ij}^d S_{ij}^d)^{5/4}} \qquad (3.5)$$

and

$$\bar{S}_{ij} = \frac{1}{2}\left(\frac{\partial u_i}{\partial x_j} + \frac{\partial u_j}{\partial x_i}\right) \qquad (3.6)$$

where, υ_t is turbulent viscosity, $\bar{S}_{ij}$ is the rate of strain tensor for the resolved scales, C_w is the WALE model constant, Δ is the sub-grid characteristic length scale equal to the grid resolution, S_{ij}^d is the traceless symmetric part of the square of the velocity gradient tensor (g_{ij}) and is described as

$$S_{ij}^d = \frac{1}{2}\left(\bar{g}_{ij}^2 + \bar{g}_{ij}^2\right) - \frac{1}{3}\delta_{ij}\bar{g}_{kk}^2 \qquad (3.7)$$

in which,

$$g_{ij} = \frac{\partial u_i}{\partial x_j} \qquad (3.8)$$

The WALE model constant, which was assumed here to be 0.46 (Cevheri et al. 2016), is important in maintaining the near-wall scaling for the eddy viscosity without the requirement for damping functions.

3.3. Fractional-step Method

Hydro3D (Ouro and Stoesser, 2017) employs a staggered rectilinear Cartesian grid whereby u, v, w, and p and computed on four separate grids and the velocity vectors, approximated by a fourth-order central differencing scheme, are stored in the middle of the cell faces and the pressure at the cell centres. It should be noted that this is a subtly different approach to other similar codes (eg: KIVA (Amsden et al. 1989) or Nek5000 (Fischer et al. 2008)) where the velocity vectors are more commonly stored at the middle of the cell edges.

Due to the staggered grid implementation, the spatially filtered Navier-stokes equations, as described by Eq's. 1 and 2 in Section 3.2, are advanced in time using a fractional-step method, based upon the projection method developed by Chorin (1968), whereby the computation of velocity and pressure are decoupled. The fractional-step method obtains the flow field using Helmholtz decomposition by predicting the velocity field, $\tilde{u}$ from the convection, diffusion, and pressure terms of the previous time step.

The first computation of the fractional-step method is to obtain the convective and diffusive terms using a low-storage, three-step Runge-Kutta scheme (Cevheri et al. 2016)

$$\frac{\tilde{u} - u^{l-1}}{\Delta t} = \nu \alpha_l \nabla^2 u^{l-1} - \alpha_l \nabla p^{l-1} - \alpha_l [(u\nabla)u]^{l-1} - \beta_l [(u\nabla)u]^{l-2} \qquad (3.9)$$

where, l is the Runge-Kutta sub-step whereby $l = 1$ denotes values from the previous time step, $t - 1$, $l = 2$ denotes the current time step, and $l = 3$ denotes the next time step, $t + 1$, and α_l and β_l are the Runge-Kutta coefficients with values as follows: $\alpha_1 = \beta_1 = 1/3$, $\alpha_2 = \beta_2 = 1/6$, and $\alpha_3 = \beta_3 = 1/2$.

However, as this study employs an IB method, which is explained further in Section 3.4, the Eulerian force, f is also applied to account for a Lagrangian body within the fluid domain, giving a corrected velocity field, $\tilde{u}^*$ described as

$$\tilde{u}^* = \tilde{u} + f\Delta t \qquad (3.10)$$

The Poisson equation is then solved iteratively using the multigrid approach developed by Ferziger and Peric (2002) to give a pseudo-projection scalar function, $\tilde{p}$ as

$$\nabla^2 \tilde{p} = \frac{\nabla \tilde{u}^*}{\Delta t} \qquad (3.11)$$

The pseudo-projection scalar function is then used to project the corrected velocity field onto the divergence-free field to give the velocity field at the current time step, u^t as

$$u^t = \tilde{u}^* - \Delta t \nabla \tilde{p} \qquad (3.12)$$

Iterations of the Poisson equation continue until the divergence-free condition of u^t is met.

Lastly, the pressure field is calculated at the current time step, p^t using the result of the previous time step, p^{t-1} and the pseudo-projection scalar function using

$$p^t = p^{t-1} + \tilde{p} - \frac{v \Delta t}{2} \nabla^2 \qquad (3.13)$$

As is common practice, Hydro3D (Ouro and Stoesser, 2017) enforces the Courant-Friedrichs-Lewy (CFL) condition to ensure model stability through a CFL number, α, described in a general form as

$$\alpha = \Delta t \left(\sum_{i=1}^{n} \frac{u_{xi}}{\Delta x_i} \right) \leq 1 \qquad (3.14)$$

where, Δt is the time step, n is the number of dimensions (equal here to 3), u_{xi} ($i = $ 1,2,3) is the magnitude of the velocity in each dimension, and Δx_i ($i = $ 1,2,3) is the length interval (equal here to the corresponding fluid cell dimension).

Model stability is further ensured through application of a factor, in this study equal to 0.1, to the pressure forcing, or gradient, across the periodic boundaries to help maintain the flowrate at those boundaries.

3.4. Immersed Boundary Method

The Immersed Boundary (IB) method was originally developed for use in the simulation of heart valves by Peskin (1972). This initial approach has been built upon by many subsequent researchers resulting in two main tranches of IB methodology:

continuum and discrete. The continuum approach uses a continuous description of a body to project velocities over the vectors normal to the body surface. Whereas the discrete approach uses a set of individual Lagrangian points to represent the shape of a body and an interpolation procedure to map velocities onto the Eulerian fluid grid.

In this study, a refined version of the Direct Forcing Immersed Boundary (DFIB) method developed by Uhlmann (2005) is used due to its numerical stability and applicability to complex geometries, as well as its computational efficiency.

In DFIB methodology, solid bodies are discretised into a finite amount of Lagrangian markers, or points (the Lagrangian grid). The desired velocity at each Lagrangian point is enforced onto the surrounding fluid cells using the forcing term, f seen earlier in Section's 3.2 and 3.3, through a set of direct forcing equations that follow a multi-step predictor-corrector procedure.

Firstly, a delta function, δ is used to interpolate the predicted Eulerian velocities, $\tilde{u}$ calculated using Eq. 3.9 in Section 3.3, to each Lagrangian point, L from its closest number of Eulerian neighbours, n_e to give the Lagrangian velocity, U_L

$$U_L = \sum_{ijk=1}^{n_e} \tilde{u}_{ijk}\, \delta\big(x_{ijk} - X_L\big)\Delta x_{ijk} \tag{3.15}$$

where, x_{ijk} is the vector of the Eulerian fluid cell ijk, $X_L = (X_L, Y_L, Z_L)^T$ is the location of the Lagrangian point, L, and $\Delta x_{ijk} = \Delta x \cdot \Delta y \cdot \Delta z$ is the Eulerian fluid cell volume.

The delta function is calculated through the multiplication of three, one-dimensional kernels, $\emptyset$ as

$$\delta\big(x_{ijk} - X_L\big) = \frac{1}{\Delta x_{ijk}}\emptyset\big(\tfrac{x_{ijk}-X_L}{\Delta x}\big)\emptyset\big(\tfrac{y_{ijk}-Y_L}{\Delta y}\big)\emptyset\big(\tfrac{z_{ijk}-Z_L}{\Delta z}\big) \tag{3.16}$$

This study uses a kernel with 27 neighbouring cells as using a higher n_e would be prohibitively computationally expensive due to the high number of Lagrangian points combined with the high resolution, large fluid domain used in this study.

To satisfy the no-slip condition at each Lagrangian point, a force, F_L that accounts for the difference between the desired velocity at that point, U_L^* and the previously interpolated Lagrangian velocity, U_L can be calculated as

$$F_L = \frac{U_L^* - U_L}{\Delta t} \tag{3.17}$$

Therefore, for the case when the solid body is static, like in this study, U_L^* is zero.

To obtain the Eulerian force, f a backwards procedure of using the delta function, δ to now reverse interpolate F_L from the closest Lagrangian points, n_L to each Eulerian fluid cell is followed:

$$f(x_{ijk}) = \sum_{L=1}^{n_L} F_L \, \delta(X_L - x_{ijk}) \, \Delta V_L \tag{3.18}$$

where, ΔV_L is the Lagrangian volume which should approximate Δx_{ijk}.

Within each Eulerian cell there can only be one Lagrangian point to ensure the total force exchanged between the two grids using Eq. 3.18 remains constant.

Finally, using Eq. 3.10 described in Section 3.3, the predicted Eulerian velocity, $\tilde{u}$ is corrected using the Eulerian force, f to give the corrected velocity field, $\tilde{u}^*$.

Chapter 4

4. Physical Representation of a Gravel Riverbed

4.1. Aims and Objectives

An experimental investigation of flow over a naturalistic gravel riverbed was undertaken by Nassrullah et al. (2019) as the first undertaking of a wider study into the flow characteristics above porous roughness surfaces. The next undertaking of this wider study is a similar investigation into flow over an artificial riverbed. To that end, this chapter aims to provide a novel methodology for the creation of an artificial riverbed with similar characteristics to natural gravel riverbed. This chapter proceeds firstly to provide detail on how an artificial riverbed was designed using CAD. It then explains how the artificial riverbed was manufactured using Computer Numerical Control (CNC) manufacturing processes. This chapter then offers statistical analysis by means of skewness, kurtosis, power spectral density, and a roughness geometry function to determine how well the characteristics of this artificial riverbed compare with natural gravel riverbed found in the literature. Lastly, and only for completeness, this chapter also provides a very brief summary of the experimental methodology that is being undertaken using the artificial riverbed developed here.

4.2. CAD Model Development

The design of the artificial riverbed was largely determined by the constraints of the Computer Numerical Control (CNC) manufacturing process as well as the

experimental setup. The largest effective machining area of the CNC machines available in Cardiff University's Mechanical Department is 600 mm × 700 mm × 600 mm in the x, y, and z directions. Thus, any component of the artificial riverbed not only had to fit within these dimensions, it also had to have ample space surrounding it to allow it to be readily fixed to the machining table.

The experimentation performed by Nassrullah et al. (2019) in the case of a naturalistic gravel riverbed was conducted using a 300 mm wide and 10 m long narrow flume within Cardiff University's Hydro-Lab. Therefore, the artificial riverbed could, at a maximum, be 300 mm wide to permit use in the same flume. Equally, the artificial riverbed could be a maximum of 120 mm deep to enable comparison with the riverbed of natural gravel of the same depth

Flow in the narrow flume can be considered uniform between approximately 4 m and 6 m from the inlet based on the surface water slope obtained through depth gauge measurements performed above different rough natural gravel beds with discharge between 0.004 and 0.009 m^3/s and particles sizes from 20-35mm (Shahla Nassrullah, personal communication, February 2018). Beyond 7 m, the backwater influence of the outlet's sluice gate affects the flow (Shahla Nassrullah, personal communication, February 2018). Therefore, the artificial riverbed would not need to be longer than two meters, as flow measurements can only be taken once flow is uniform. Equally, machining an artificial riverbed longer than 2m was also deemed impractical and beyond the scope of this study. However, creating an artificial riverbed shorter than two meters would not allow the flow to propagate and develop through the pore matrix, and any measurements obtained would not necessarily feature highly turbulent near-bed and pore-space flows. It was proposed that natural gravel would be placed upstream and downstream of the artificial riverbed within the flume to minimize the development of an internal boundary layer at the roughness transition (ie: at 4m from the inlet). The gravel particle size, particle size distribution, roughness characteristics would all need to be very similar to the artificial riverbed for this to be achieved. The dimensional limitations used to create a 3D CAD model representing a gravel riverbed were therefore a width of 300 mm, a depth of 120m, and a length of 2m.

The CAD model was developed by dividing the length of the riverbed into four, 500 mm long identical elements. Thus, requiring only one unique element, or assembly, to be created, with the remaining three being copies of the original. To achieve the appearance and characteristics of a natural gravel riverbed, the artificial gravel particles had to meet the following conditions: be individually,

uniquely curved shapes devoid of any flat planes in any axis or overlap, appear randomly positioned in terms of each particle not touching another particle at the exact same place, and form void spaces that vary in volume and shape. These criteria were achieved by first designing a single, 300 mm wide and 500 mm long layer of 272 uniquely shaped gravel particles with diameters between 26–30 mm, with an average diameter of 28 mm, as shown in Fig's. 4.1(a) and 4.1(b).

Within this layer, voids between particles were formed by ensuring that individual particles touched each other in a triangular formation, as shown by Fig. 4.1(b). Due to the CNC machining process, each particle had to be rigidly joined to each of its neighbours to provide structural stability to the overall layer whilst being machined due to the brittleness of the chosen material for manufacturing. Such joints were achieved by overlapping the jointing edges by some portion as shown in Fig. 4.3(b). Though this jointing method diverges from that found naturally where gravel particles might only touch at one discrete point, individually machining over 5500 individual particles to achieve this effect was deemed impractical for use in this study.

a)

b)

c)

d)
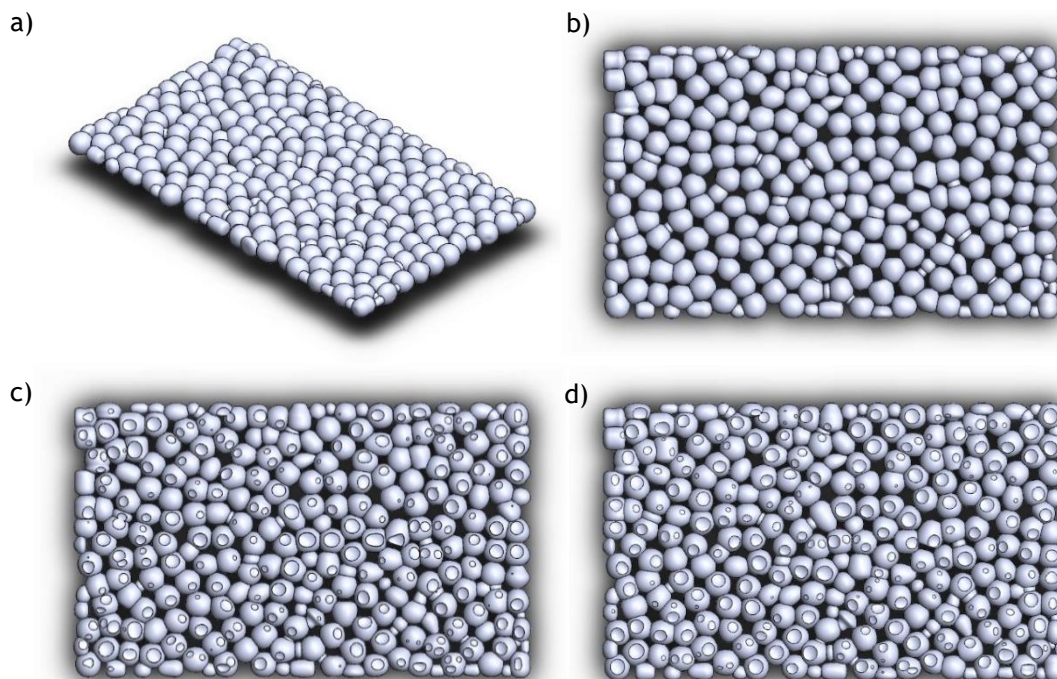
Figure 4.1. Clockwise from top left; **(a)** An orthogonal view of the first layer of the artificial riverbed measuring 300 mm wide, 500 mm long, and 28 mm thick, on average; **(b)** The plan view of the first layer of the artificial riverbed, highlighting how particle geometry is positioned to form voids; **(c)** The plan view of the second layer of the artificial riverbed, highlighting the cavities left by the third layer; **(d)**

The plan view of the fourth layer of the artificial riverbed, highlighting the cavities left by the fifth layer.

This unique, original layer of artificial gravel particles was then copied four times, giving five similar layers that were then stacked at 23 mm centers and at different orientations, as detailed in Table 4.1(a), to form a 120 mm tall assembly. As Fig's. 4.1(c) and 4.1(d) show, the first, third, and fifth-layer geometry were taken away from the second and fourth layers, forming cavities or sockets where the geometries intersected. Thus, once machined, each layer of the riverbed would fit together with minimal interference and in the correct orientation.

At this point in the design, there were a total of 12 similar 'whole' geometry sheets for the first, third, and fifth layers, four similar 'cavity' geometry sheets for the second layer, and a further four similar 'cavity' geometry sheets for the fourth layer; these made up the entire artificial gravel riverbed assembly.

To realise a mating design between each assembly similar to that between the layers within those assemblies, every sheet would have to be unique. This would greatly increase the time required for setup, and the CNC cut program development by the machinist resulting in an increased total manufacturing time. Therefore, without greatly increasing this time, yet preventing disjointed geometry between assemblies, three unique jointing elements were designed.

Table 4.1. Orientation details for the layers and assemblies of the artificial riverbed.

(a) Layer Orientation Details		(b) Assembly Orientation Details	
Layer Number	180° Rotation about Axis Relative to Layer 1	Assembly Number	180° Rotation about Axis Relative to Assembly 1
1	None - bottom	1	None
2	y-axis	2	y-axis
3	z-axis	3	None
4	x-axis	4	y-axis
5	None-top		

To improve the geometric variation in the streamwise direction, each assembly was orientated differently, as detailed in Table 4.1(b). At the joints between the assemblies three similar 120 mm tall and 300 mm wide elements, which were created in the same fashion as the layers that made up each assembly, were inserted at eight-millimeter offsets from each assembly. The solid assembly

geometry was taken away from the jointing elements, forming cavities where the geometry intersects, and creating two different types of unique joint. Two of the joints are shown in Fig. 4.2(a), and one of the joints is shown in Fig. 4.2(b).

Equivalent 500 mm-wide joints were also designed in a similar fashion to the 300 mm-wide joints to allow a 500 mm-wide flume to potentially be used in later study. For the 500 mm-wide joints, each assembly was orientated in the same fashion as detailed in Table 4.1(b) but placed side-by-side rather than end-on-end. Finally, manufacturing, and numerical simulation of the now 2.048 m long, if using 300 mm-wide joints, or 1.248 m long if using 500 mm-wide joints, artificial riverbed assembly could begin.

(a)   (b)
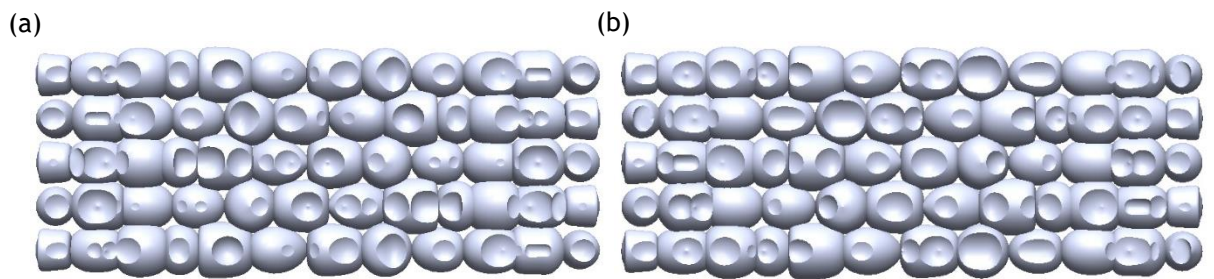
Figure 4.2. (a) The side view of the jointing element between assemblies one and two, as well as assemblies three and four; **(b)** The side view of the jointing element between assemblies two and three.

4.3. Manufacture

The CAD design outlined in Section 4.1 was used to physically manufacture an artificial gravel riverbed from a single 3.050-m long, 2.030-m wide and 30-mm thick sheet of cast acrylic. Cast acrylic was chosen for manufacturing due to it being relatively easy to machine using CNC machines; it exhibits high thermal stability, is readily available at a reasonable cost, and exhibits good structural properties whilst remaining relatively lightweight and, above all else, is transparent. Transparency was a key material requirement, as proposed video capture inside the riverbed matrix pores would only be possible with high light levels. Also, using a transparent material gives a greater possibility of being able to gather velocity data using non-intrusive video and scanning techniques. This is particularly desirable in terms of turbulent flow structures that might otherwise by disrupted or even enhanced by measurement apparatus positioned within the water column itself.

It should be noted that cast acrylic does discolor with time, but it can easily be rejuvenated with the application of a small amount of cutting compound. Ideally,

the refractive index of the cast acrylic (1.49) would be closer to that of water at 20°C (1.33), resulting in riverbed geometry being indistinguishable from water. Thus, similar to Dark (2017), the flow across the entire width of the riverbed could be studied. However, the study using this artificial riverbed only needed to use video cameras with a focal depth of 30 mm, and so looking beyond that depth from any given camera location would not be possible and cast acrylic could be used.

The first step in manufacturing was to cut the cast acrylic sheet into 25, 600 mm-long by 400 mm-wide plates, and thus, providing a couple of spare sheets in case they were needed due to manufacturing issues. As explained in Section 4.1, the geometry of the artificial riverbed only required a 500 mm by 300 mm plate; however, a surrounding frame was required, as shown in Fig. 4.3(a), to allow the material to be clamped to the CNC machine bed. The riverbed geometry was connected to the frame with at least 20 evenly spaced tags, or ribs. Once clamped to either of the two five-axis CNC machines (only three-axis required) that were used, each plate was individually milled. To reduce the setup and cut programming between plates, and thus reduce the overall manufacturing time, only one side of all the corresponding plates was milled. It was not until that side of all that layer type, as detailed in Section 4.1, were completed that the plates could be turned over, re-mounted, and the remaining sides of each plate milled.

(a)   (b)
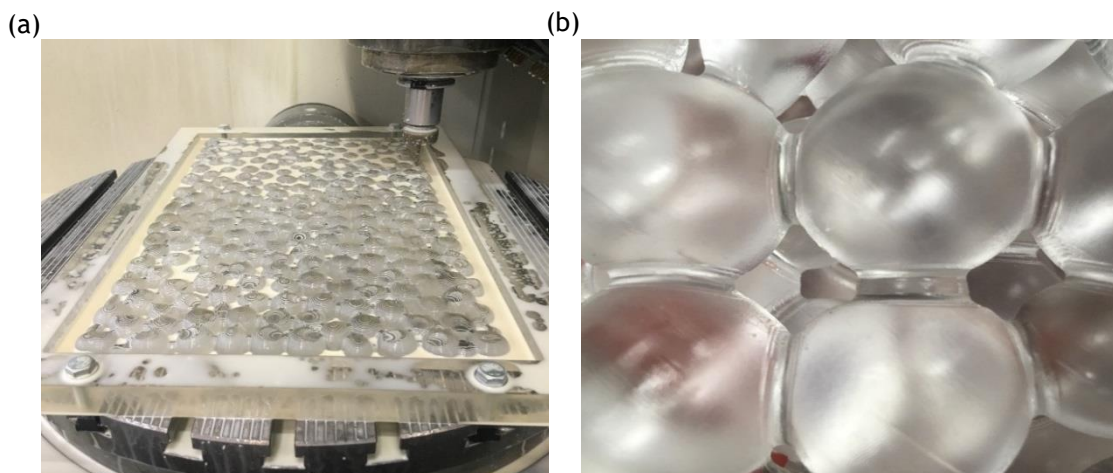
Figure 4.3. (a) A typical plate of the artificial riverbed in the process of being machined using a 4 mm flat, long series bit including the surrounding frame required for clamping the plate to the CNC machine bed; **(b)** A close-up, in plan, of the artificial gravel particles highlighting the fillet detail between adjoining particles and the voids that are typically formed when the layers are stacked.

The cast acrylic was machined using a 12 mm flat, long series bit for roughing out the geometry before a 4 mm flat, long series bit was used to start forming the

curvature of the geometry and pores, as shown in Fig. 4.3(a), and a 3 mm ball end bit was used to finish the detailing. A final pass by a pencil-line program and a 2 mm ball end bit was used to help smooth over any machining marks resulting in the completed plate, as shown in Fig. 4.4(a). This final pencil-line program reduced the radii of the joints between any of the curved surfaces. The radii could have been further reduced with a smaller diameter bit, but at the cost of increased machining time and reduced shear strength of the plate at large, making it much more likely to fail whilst machining. The filleted material between artificial gravel particles, as shown in Fig. 4.3(b), resembles small-grained sediment particles, such as silts, that have culminated into the riverbed matrix similar to that found in nature. Thus, this specific artifact of the machining process helps to enhance the realism and representation of a natural gravel riverbed in cast acrylic. However, this is a small deviation of the physical model from the CAD model.

a) b)
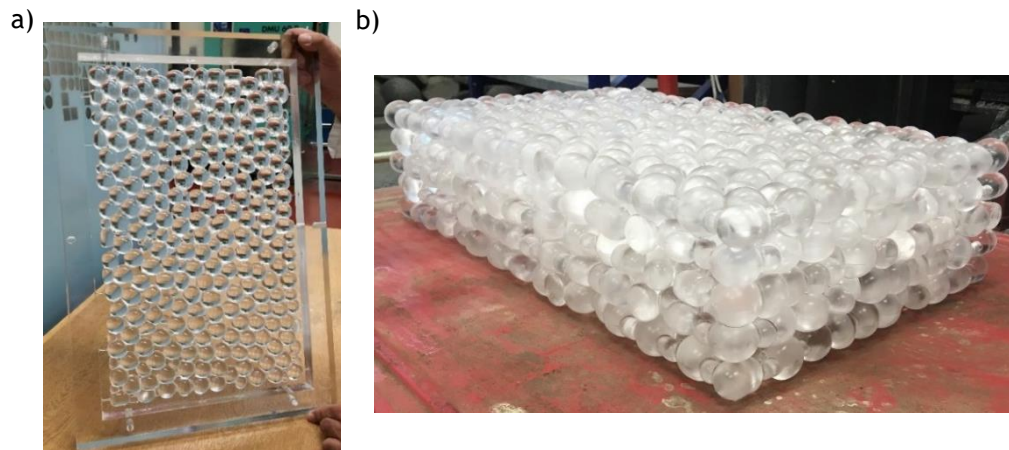
Figure 4.4. (a) A typical completed plate with the frame still attached, highlighting the optical clarity of the cast acrylic; **(b)** A fully stacked assembly of the artificial riverbed prior to placement within the flume, highlighting the discoloration of the cast acrylic with time.

Upon completion of the machining, the tags between the geometry and the frame were cut, and any residual tag was filed back. It was at this point that any dimensional difference between the very small tolerance of the machining and the relatively large tolerance of the manufacture of the cast acrylic itself were dealt with. Cast acrylic is formed by pouring molten acrylic into a mold, which resulted in a relatively large degree of tolerance in material thickness over the 500 mm length of a single plate. Such dimensional variability could have been avoided by using extruded acrylic, but due to its low thermal stability resulting in poor machinability, this was not an option in this instance. With the design of the

artificial riverbed consisting of nominally spherical shapes between 26–30 mm in diameter, the large tolerance in material thickness resulted in two or three small flat spots forming on each side of every plate. These were removed by sanding the affected area to a smooth convex shape. Again, this is a divergence of the physical model from that modeled using CAD. The resulting plates could then be stacked, as described in Section 4.1 and as shown in Fig. 4.4(b), to form the completed assembly of the artificial riverbed within the flume, as shown by Fig. 4.5(a), and the resulting artificial roughness surface, as shown by Fig. 4.5(b). The physical and statistical characteristics of this artificial riverbed are explored in Section 4.4 to determine how well it represents a natural gravel riverbed and thus, whether the methodology explained in this chapter provides a methodology for creating a naturalistic artificial riverbed.

(a) (b)
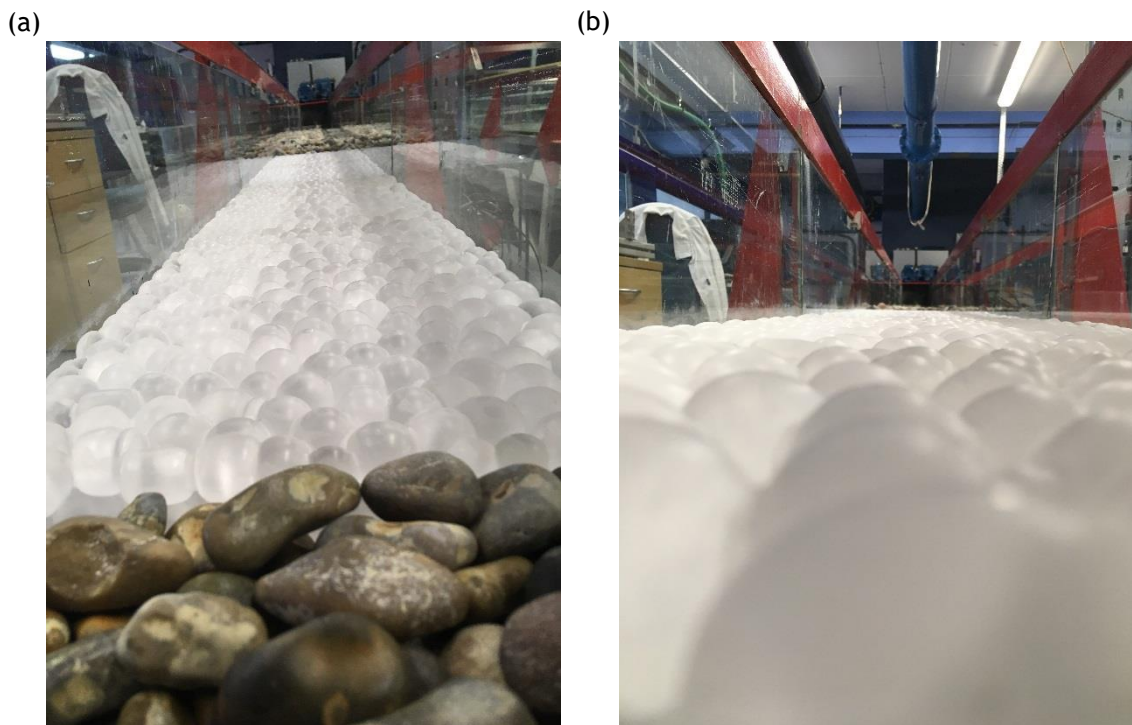
Figure 4.5. (a) The completed 2.048 m long, 300 mm wide cast acrylic artificial riverbed set within the narrow flume of Cardiff University's Hydro-Lab looking downstream, also showing the resulting porous roughness surface; **(b)** A view looking downstream at the bed-surface level clearly showing the crests and troughs of the resulting porous roughness surface.

4.4. Porosity and Roughness Analysis

The CAD software's inbuilt volume calculator was used to aid the calculation of the porosity of the artificial gravel riverbed. The volume of the voids formed on the

surface of the riverbed are considered by this study to be part of the channel, rather than the riverbed itself. Thus, to calculate the volume occupied by the geometry, the surface geometry, which was determined as 0.25d above the centerline of the uppermost layer of the artificial riverbed, was excluded, giving the volume of the geometry as 11,612.46 cm^3. The total volume occupied by the geometry was calculated as 16,950 cm^3, again excluding the surface geometry by using a height of 0.113 m instead of 0.12 m. Thus, the porosity of the artificial gravel riverbed was calculated using the following equation:

$$\text{porosity} = \frac{(\text{total volume} - \text{volume occupied by the geometry})}{\text{total volume}} \times 100\% \qquad (4.1)$$

as 31.5%. This porosity compares well with that found by Nassrullah et al. (2019) for their experimentation using gravel that was on average 20 mm in diameter with a porosity of 35.8%, and that found by Shahla Nassrullah for gravel with an average diameter of 35 mm in diameter of 31.1% (personal communication, February 2018).

Using the relationship:

$$\text{void ratio} = \frac{\text{porosity}}{1 - \text{porosity}} \qquad (4.2)$$

the void ratio of the artificial riverbed was calculated as 0.46, which was at the extreme end, due to the lack of smaller particles; it was also within the minimum and maximum range for typical gravels of 0.3 to 0.6, respectively (Das, 2008). Therefore, the artificial riverbed's pore matrix is comparable to that of a natural gravel riverbed in volume, which is a key determinant of the interstitial flowrate.

To quantify the roughness the artificial gravel riverbed presents to the fluid, the manufactured plates could have been probed using a gauge point, or similar equipment, within the laboratory to obtain a limited data set of surface elevations for use in the statistical analysis presented here. However, since the artificial riverbed was developed using CAD, thus meaning the surface was already well described, it was decided that processing the geometry using the meshing software Gmsh (Geuzaine et al. 2009) at an extremely fine mesh resolution so as to approximate the uppermost surface of the CAD geometry as closely as possible would provide the best possible bed elevation data for further analysis. The process of meshing is fully explained in Section 5.3 regarding the numerical representation of gravel riverbed found in Chapter 5. In brief, the meshing of only the surface geometry of the uppermost layer of the artificial riverbed was achieved using Gmsh

(Geuzaine et al. 2009) by applying default settings, in addition to using recombination for all triangular meshes, and setting minimum/maximum element sizes of zero and one respectively.

Using the following equations:

$$\sigma_z = \sqrt{\frac{1}{N}\sum_{i=1}^{N}(z(i) - \bar{z})^2} \tag{4.3}$$

$$Sk_z = \frac{\frac{1}{N}\sum_{i=1}^{N}(z(i)-\bar{z})^3}{\sigma_z^3} \tag{4.4}$$

$$Ku_z = \frac{\frac{1}{N}\sum_{i=1}^{N}(z(i)-\bar{z})^4}{\sigma_z^4} - 3 \tag{4.5}$$

where,

$$\bar{z} = \frac{1}{N}\sum_{i=1}^{N} z(i) \tag{4.6}$$

the standard deviation in Eq. (4.3), Fisher–Pearson coefficient of skewness in Eq. (4.4), and kurtosis in Eq. (4.5) of the artificial riverbed's surface elevations, $z(x, y)$, were found using an N of 347,766, or the number of nodes that describe the artificial riverbed's surface geometry, as summarised in Table 4.2.

The confidence intervals for standard deviation shown in Table 4.2 were calculated using the following formulae (Spiegel and Stephens, 1999) (p.245):

$$\sqrt{\frac{(N-1)\sigma^2}{\chi_{0.05}^2}} < \sigma < \sqrt{\frac{(N-1)\sigma^2}{\chi_{(1-0.05)}^2}} \tag{4.7}$$

where,

$$\chi_{0.05}^2 \approx \frac{1}{2}\left[z_{0.05} + \sqrt{2df - 1}\right]^2 \tag{4.8}$$

and df is the degrees of freedom equal to $N - 1$, and $\chi_{0.05}^2$ and $z_{0.05}$ are the chi-squared and normal distributions, respectively, for the 95% confidence level. Note that Eq. (4.8) is only applicable if the df value is greater than 30.

The standard errors of skewness and kurtosis that are shown in Table 4.2 were calculated using the following formula:

$$\text{Standard error of skewness} = \sqrt{\frac{6}{N}} \tag{4.9}$$

$$\text{Standard error of kurtosis} = \sqrt{\frac{24}{N}} \tag{4.10}$$

As Table 4.2 shows, the variance in the size of the particles in the artificial gravel riverbed is lower than that found using natural gravel, but not as low as that used in a 2018 study (Stewart et al. 2018) for their R3 roughness plate design. Given the apparent uniformity of the CAD design, as shown by Fig. 4.1(a), the standard deviation of 3.81 mm in the surface elevations is somewhat larger than expected. This is likely due to the inclusion of the much smaller than average diameter geometry that was used to improve the structural rigidity of the artificial riverbed by joining specific particles together, as shown by Fig. 4.1(b). That said, even greater variance in the particle size of the artificial gravel riverbed would be desirable to create a true likeness of a natural gravel riverbed. However, due to the prohibitory cost involved in obtaining thicker material, and thus more particles larger than the desired 28-mm average diameter, as well as the increased machining and setup time required, this was not possible in this study. Of course, a smaller average diameter could have been used, but at the expense of the structural rigidity of each plate, resulting in an increased risk of particle breakage whilst being machined. Thus, a reduction in the average diameter was decided against in this study.

Table 4.2. Bulk statistics of various artificial and natural gravel riverbeds, table adapted from Stewart et al. (2018) (p. 7) to include multiple studies.

Roughness material	σ_z (mm)	Sk_z (-)	Ku_z (-)
Cast acrylic artificial gravel riverbed, 28-mm diameter	3.81*	−0.176 (± 0.004)	−1.012 (± 0.008)
35-mm diameter gravel (Shahla Nassrullah, personal communication, February 2018)	6.06 (5.50,6.77)	0.19 (± 0.18)	−0.72 (± 0.37)
20-mm diameter gravel (Nassrullah et al. 2019)	7.83 (7.28,8.48)	−0.59 (± 0.13)	−0.30 (± 0.27)
Epoxy resin artificial roughness plates, R3 design (Stewart et al. 2018)	1.58 (1.46,1.72)	−0.11 (± 0.14)	0.18 (± 0.28)

Table 4.2 also shows that the skewness of the artificial gravel riverbed is close to zero, with little error due to the large population size, suggesting that the surface elevations have a normal distribution. The negative and relatively large kurtosis shown in Table 4.2 for the artificial gravel riverbed reflects the lack of any significant variance in the size of the gravel particles, in particular, particles larger than the average diameter particles, and the few resulting irregularities in the surface elevations.

To further investigate the roughness characteristics of the artificial gravel riverbed, a roughness geometry function $A(z')$ (Stoesser, 2010 and Nikora et al. 2001), which describes the cumulative probability distribution of $z(x,y)$, was utilised, and $A(z')$ as a function of surface elevation fluctuation zb' is plotted in Fig. 4.6. As Fig. 4. 6 shows, the distribution of the surface geometry elevations of the artificial gravel riverbed are near indistinguishable from those obtained by Shahla Nassrullah (personal communication, February 2018) and Nassrullah, et al. (2019) for natural gravel-bed surfaces, which were either 35 mm or 20 mm in diameter, respectively and were placed within a flume. The distribution of surface elevations found in a 2001 study (Nikora et al. 2001) for both unworked gravels placed within a flume and water-worked natural riverbed gravel also correspond well to that of the artificial gravel riverbed. Equally, the distribution of surface elevations of the artificial gravel riverbed is, as expected from the result of the skewness test shown in Table 4.2, close to a normal distribution. The work undertaken by Aberle (2007) and Aberle and Nikora (2006) confirmed that the surface elevations of natural gravel riverbeds are normally distributed, thus corroborating the assertion that the artificial gravel riverbed's surface elevation distribution is representative of that found in natural gravel riverbeds at large. Therefore, it seems reasonable to characterise the artificial riverbed as rough, with particles similarly distributed to natural gravel riverbeds. However, further analysis is required to determine how rough the artificial riverbed is in comparison to natural rivers.
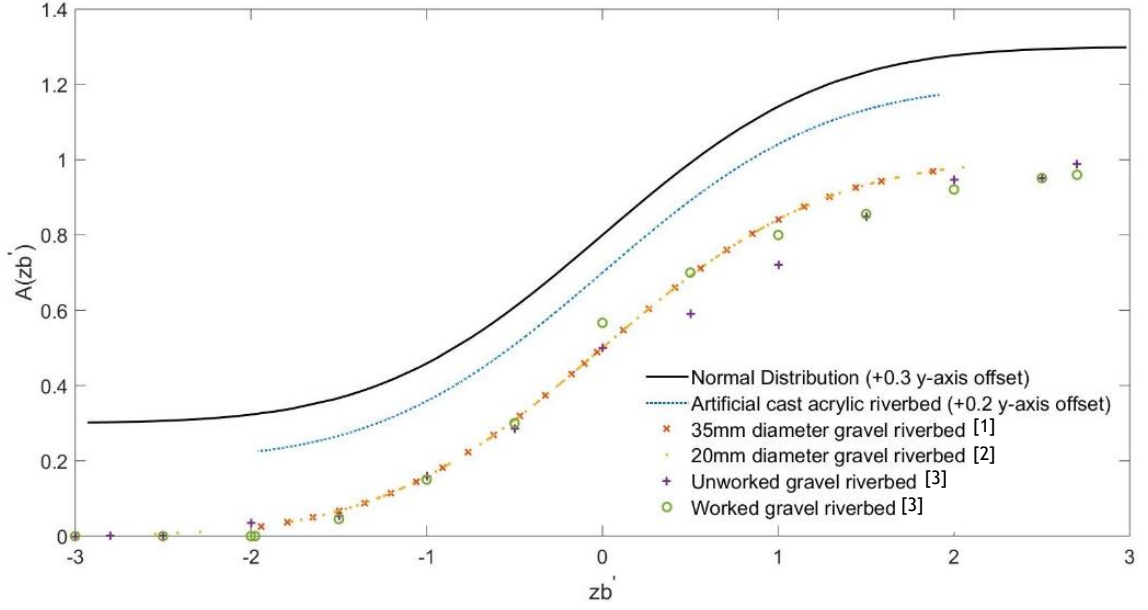
Figure 4.6. Cumulative probability distribution of surface elevations for natural and artificial gravel riverbeds of various studies: [1] (Shahla Nassrullah, personal communication, February 2018), [2] (Nassrullah et al. 2019), [3] (Nikora et al. 2001).

The Power Spectral Density (PSD) of a surface is often used to analyse surface roughness as it represents the amplitude of a surface's roughness as a function of the spatial frequency of the roughness. Thus, the contribution of different spatial frequencies, or wavevectors, to the roughness of a surface can be ascertained. The wavevector is the inverse of the wavelength of the surface roughness amplitude. Simplistically, the PSD of a surface provides a graphical representation of the distribution of roughness throughout a surface. Assuming a surface is randomly rough with a Gaussian distribution, then the PSD of that surface defines its roughness characteristics Persson et al. (2005). If such characteristics do not vary under magnification, then the surface can be considered self-affined, and will exhibit a power-law relationship (Persson, et al. 2005):

$$S(k_x) \sim k_x^{-(2H+1)} \tag{4.11}$$

where, H is the Hurst exponent related to the fractal dimension, D_f, by $H = 3 - D_f$. The relation expressed by Eq. (4.11) is only true within the region:

$$k_0 < k < k_1 \tag{4.12}$$

where, $k_0 = 2\pi/\lambda_0$ indicates the short distance cutoff that is equal to the smallest possible wavevector corresponding to the largest particle size used, λ_0, and k_1 is the long-distance, or maximal wavelength, cutoff equal to the largest possible wavevector.

As Persson et al. (2005) suggested, for many surfaces, a k_1 value does not exist in the strictest sense, as $S(k_x)$ tends to a constant, thus the long-wavelength component is in effect already removed from the PSD profile. Thus, using Eq. (4.11) H can be determined from the slope of a linear regression line fitted in the region $k > k_0$ of a PSD. Using a λ_0 value of 28 mm, the short distance, or minimal wavelength, cutoff was found to be 0.2244 for the artificial riverbed. By applying a Fast Fourier Transform (FFT) Matlab Function (Kanafi, 2016) to the same surface geometry used to calculate the bulk statistics of the riverbed, the PSD of the artificial riverbed was found, as shown in Fig. 4.7.

By applying a linear regression line to the PSD in the region expressed in Eq. (4.12), as shown in Fig. 4.7, the spectral slope was found to equal 2.94 and thus, using Eq. (4.11), the Hurst exponent was found to be 0.97. Since this value of H is less than unity, the artificial riverbed can be considered a fractal at some scales (Kanafi, 2016). Typically, $H = 0.79 \pm 0.04$ for natural gravel-bed streams, and $H = 0.50 \pm 0.07$ for gravel placed within a flume (Nikora et al. 1998)(p. 522).
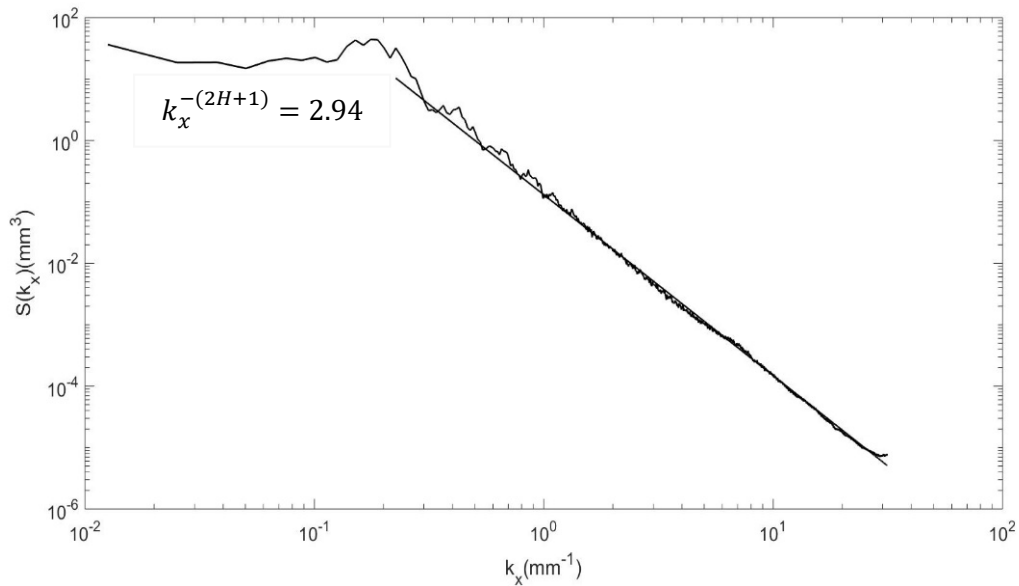
Figure 4.7. One-dimensional surface roughness PSD of the artificial gravel riverbed's surface and a regression line between k_0 and k_1 with spectral slope $k_x^{-(2H+1)}$, where H is the Hurst exponent.

Fig. 4.6 clearly shows that the distribution of roughness across the surface of the artificial gravel riverbed corresponds well with that found in nature. Equally, the Hurst exponent, though some 0.18 higher than that typically found on average in nature (Nikora et al. 1998), is comparable. As Stewart et al. (2018) pointed out, the friction factor and hydraulic resistance of a riverbed decrease as the Hurst exponent increases. Thus, it can be inferred (Stewart et al. 2018) that the degree of roughness of the artificial riverbed is slightly lower in magnitude than that found in nature. However, the value of H that was found for the artificial riverbed is similar to the H of 1.02 used by Stewart et al. (2018) (p. 7) for their R3 roughness design.

4.5. Experimental Set-up

As already explained, the experimental setup that is very briefly summarised here is mentioned only for completeness and is being conducted as an extension to the study that has already been carried out into flows over naturalistic gravel riverbed by Nassrullah et al. (2019), but now using the artificial riverbed developed in this study. All experiments are conducted in the narrow flume of Cardiff University's Hydro-Lab. This recirculating flume is glass-walled and measures 0.3 m wide and 10 m long and has a maximum flowrate of 27 l/sec, which translates to a maximum velocity of 0.9 m/sec with a bed surface slope of 1/1000.

The first layer of the artificial riverbed was positioned in the flume such that the start was 3.952 m from the inlet and the end 6 m from the inlet. Each of the four subsequent layers were then added on-top according to the orientation details shown in Table 4.1 found in Section 4.1. The artificial gravel was so positioned to ensure the flow was full developed within the test section, as explained in Section 4.1. Natural gravel with a nominal diameter of 20 mm and porosity of 38% (reduced to 35.8% after taking into account the true extent of what can be considered a part of the channel) was placed to a height of 0.12 m, the same as the artificial riverbed, down- and up-stream of the artificial riverbed, filling the rest of the flume, as shown in Fig. 4.8. A honeycomb lattice was placed at both the inlet and the outlet to prevent any gravel from entering either the header tank or the pump pipework, as well as to help stabilise the gravel and help reduce any turbulence entering the flume from the header tank. The water depth was controlled using a weir placed at the channel outlet and was measured using a gauge point.

Figure 4.8. Overview, looking downstream, showing the placement of the artificial riverbed and gravel within the narrow flume in Cardiff University's Hydro-Lab.

Two experimental test cases were conducted at different free-steam velocities and water depths. Measurements in both cases were taken using a Nortek AS side looking Acoustic Doppler Velocimeter (ADV) set at a sample rate of 25 Hz. The ADV was attached to an automated stepper motor allowing the ADV to be moved vertically at 3 mm ($\pm$0.05 mm) increments starting 10 mm from the bed surface. Measurements were taken at each elevation over a 5-minute period. Post-processing of the results was undertaken to ensure low correlation ratio and Signal Noise Ratio (SNR).

4.6. Summary

In this chapter, a CAD model of a gravel riverbed matrix 120 mm in depth, 300 mm wide, and 2.048 m long was created with an average particle diameter of 28 mm. Using a CNC machine, a novel physical representation of a gravel riverbed was manufactured from cast acrylic consisting of 23 components that assemble through interference fitting to create an artificial riverbed. The artificial riverbed was then analysed in comparison with both natural and artificial riverbed data found in the literature.

The main conclusions are:

- The porosity of the artificial riverbed was calculated as 31.5%, which compares well with the values found in the literature for natural gravel-bed surfaces. Combined with a void ratio of 0.46, which although at the extreme end due to the lack of smaller particles, is within the maximum and minimum range for typical gravels. Thus, the artificial riverbed's pore matrix is comparable to that of a natural gravel riverbed.

- The standard deviation of the artificial riverbed's surface elevations was found to be 3.81 mm. This suggests that the variance in particle diameter in the artificial riverbed is less than that found in natural rivers, yet larger than that used by studies found in the literature.

- The skewness and kurtosis of the artificial riverbed were calculated as –0.176 and –1.012, respectively. The skewness result suggests that the surface elevations of the artificial riverbed are normally distributed, which was confirmed by a cumulative probability distribution plot of the riverbed's surface elevations. The negative and relatively large kurtosis relates to the lack of variance in the particle diameters used in the artificial riverbed, and thus, the lack of irregularities in the surface elevations.

- A power spectral density function was applied to the surface elevations, giving a Hurst exponent of 0.97. Thus, the artificial riverbed can be considered as fractal at some scales. Also, the artificial riverbed exhibits a degree of roughness that is slightly lower than that found in nature, yet still comparable, meaning the hydraulic resistance and friction factor will, as a result, be slightly lower than desired.

The results presented in this chapter show that the developed method can offer the physical approximation of a gravel bed surface comparable to a natural gravel riverbed with comparable surface roughness, yet reduced particle size variance, comparable particle distribution, and porosity within limits, but at the extreme end of the scale. The results presented here also show that there is some potential for enhancement of the methodology developed in this chapter. Techniques such as photogrammetry or laser displacement scanning (e.g: Stewart et al. 2018) could provide a high-resolution 3D realisation of a natural water-worked gravel-bed surface. By importing the surface realisation into a CAD software package, the subsurface/pore matrix of the riverbed could then be modeled, using the methodology described in this chapter, which would likely result in a very close representation of a water-worked natural gravel riverbed.

Chapter 5

5. Numerical Representation of a Gravel Riverbed

5.1. Aims and Objectives

This chapter aims to provide an approach to numerically representing a gravel riverbed for application within the Large Eddy Simulation (LES) code Hydro3D (Ouro and Stoesser 2017) which utilises the Immersed Boundary (IB) method, as explained in Section 3.4 found in Chapter 3. In doing so, this chapter also aims to show how this approach could be used for the development of other, highly complex immersed boundary geometry. Firstly, this chapter provides detail on the CAD design for a large-scaled representation of a natural gravel riverbed. It then explains the methodology for meshing and importing the scaled riverbed geometry into Hydro3D (Ouro and Stoesser 2017). This chapter then details how this meshing methodology was used to develop both a coarse- and a fine-resolution mesh version of the scaled riverbed geometry. This chapter also offers statistical analysis by means of skewness, kurtosis, power spectral density, and a roughness geometry function to determine how well the characteristics of both mesh resolution versions of the scaled riverbed compare with the artificial riverbed developed in Chapter 4 and with natural gravel riverbed found in the literature. Lastly, this chapter presents analysis of to what degree the meshing process has changed the geometry and hence, discusses to what degree the coarse- and fine-resolution versions represent that originally designed and the implications for larger or more complex geometry meshed using the methodology developed here.

5.2. Large Scale Model Development

Having already developed a nominally 28 mm diameter representation of a gravel riverbed for an experimental study similar that conducted by Nassrullah et al. (2019), that model could have been processed using the methodology explained here and used directly for simulation within Hydro3D (Ouro and Stoesser 2017). However, the LES fluid mesh resolution required to capture the desired turbulence phenomena, as well as the riverbed geometry mesh resolution required for good definition and numerical representation, explained in more detail in Section 5.3, would both need to be very fine. For example, with a gravel particle diameter of 30 mm, to obtain even just 30 fluid cells per diameter, the fluid mesh would need to be 0.001 m in all axes. At such a fine resolution, the significance of rounding errors to the overall simulation are no longer negligible and may even result in the simulation becoming unstable. Equally, if the artificial riverbed geometry were directly used, the simulation would be dimensionalised and would thus, require all parameters to be matched to that used in the experimentation to allow robust comparison between them. However, gathering all the necessary data through experimentation to facilitate this would prove very difficult, if not impossible and very time consuming. Equally, the ability to readily compare the simulation results with the wider literature would be that much more difficult with a case specific setup rather than a more generalised version. Thus, it seemed logical to develop a non-dimensionalised, large scale simulation that was dimensionally optimised for use within Hydro3D (Ouro and Stoesser 2017).

In using a larger scale geometry, the fluid mesh resolution could be coarser resulting in insignificant rounding errors and a more stable and accurate simulation. For example, with a large-scale gravel particle diameter of 300 mm, the fluid mesh would only need to be 0.01 m in all axes to obtain the same 30 fluid cells per diameter as before. There is, however, a trade-off with computational effort in upscaling the geometry, and thus also the size of the computational domain. If the adopted scale is very large resulting in a domain larger than used in this study, the computational effort required would make the simulation unaffordable and impractical. Choosing the correct scaling factor is paramount in balancing computational effort with simulation accuracy along with the reasonability of both the fluid and geometry mesh resolutions.

In this study, the scaling between the riverbed for the simulation and the artificial riverbed for the experimentation was based upon the particle diameter. A

scale factor of 3.2 was used to provide a nominal large-scale particle diameter of 90 mm.

At this point, the artificial riverbed geometry could have been scaled up to suit the non-dimensionalised LES model. However, this would not have resulted in a domain size that would be large enough to ensure all scales of turbulent flow are captured, or geometry that would be suitable for use with periodic boundary conditions used in this study. Therefore, an entirely new representation of a gravel riverbed was created with idealised dimensions following the methodology, including plate orientation, laid out in Section 4.2 found in Chapter 4, with one key exception. Unlike in the artificial riverbed, the edge particles of this scaled riverbed are symmetrical and perfectly hemispherical, as shown in Fig's. 5.1(a) and 5.1(b), meaning the North and South faces of the riverbed are the same, as are the East and West faces, and are split at the centreline of the boundary particles. The edge particles were created first using CAD to provide a border for the internal particles to join to following the methodology laid out in Section 4.2 found in Chapter 4.

a)   b)
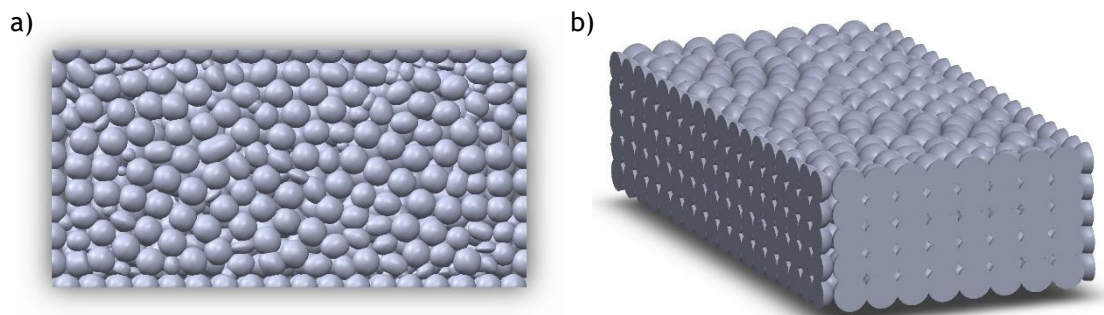
Figure 5.1. (a) Plan view of a section of the scaled riverbed model highlighting the symmetry between the North- and South-, and East- and West-edge particles; **(b)** Isometric view of a section of the scaled riverbed model highlighting the hemispherical design of the edge particles.

The symmetry of the edge particles allows the periodic boundary conditions applied in this study to be used, as explained in greater detail in Section 6.2 found in Chapter 6. Additionally, the edge particle detail allows the overall riverbed assembly to be split into smaller, self-similar sections (akin to the artificial riverbed previously described) each with this edge particle detail. By dividing the overall riverbed assembly into smaller, self-similar sections, only one section needs to be meshed, drastically reducing the computational effort and time required compared to meshing the entire riverbed assembly. The edge particles of each section

therefore also provide a seamless point of division between each section allowing the overall riverbed to be numerically assembled for use within Hydro3D (Ouro and Stoesser 2017).

The entire assembly of the scaled riverbed geometry is made up of 6 self-similar sections, each measuring 0.72 m long, 1.44 m wide, and 0.36 m tall with particles that are nominally 0.09 m in diameter. Thus, the overall assembly, as shown in Fig. 5.2, measures 4.32 m long, 1.44 m wide, and 0.36 m tall, which as will be explained in Chapter 6, is equivalent to $12h \cdot 4h \cdot h$ where h is the surface flow depth.
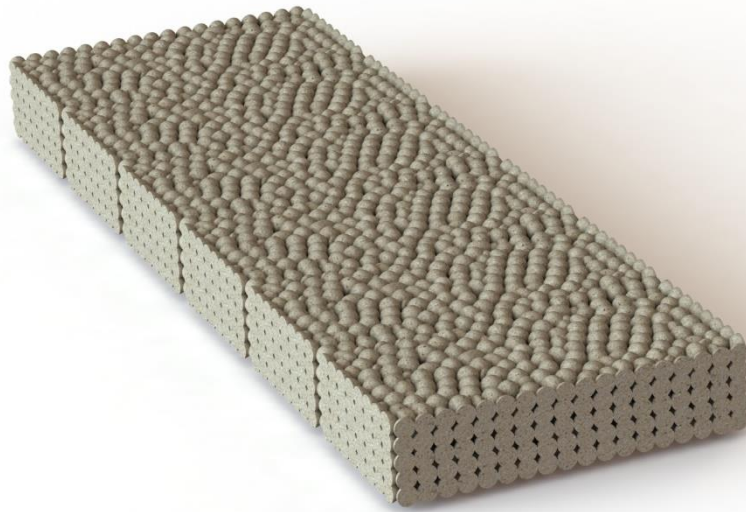
Figure 5.2. A rendered image of the entire scaled riverbed geometry assembly measuring $12h \times 4h \times h$ where h is the surface flow depth.

5.3. Gmsh2Hydro3D Methodology

The CAD model described in Section 5.2 cannot be directly imported into, or simulated in, a computational flow modeling program such as Hydro3D (Ouro and Stoesser 2017) and instead must first undergo meshing. Meshing takes the solid surfaces described by a .STEP file exported from the CAD program and applies a series of numerical algorithms that result in the surfaces being redrawn as a series of triangular shapes with vertices that are point nodes with x-, y-, and z-coordinates that describe a close approximation to the original CAD model surface geometry. The meshing of the scaled riverbed was undertaken using the meshing software Gmsh (Geuzaine et al. 2009) by applying the default settings of using a Blossum 2D recombination algorithm and a Delaunay 3D meshing algorithm, in addition to using recombination for all triangular meshes, and by setting minimum/maximum

element sizes of zero and one respectively. The output from Gmsh (Geuzaine et al. 2009), referred to hereafter as Gmsh-Raw, was an unstructured mesh of 24,686,021 nodes representing one section of the scaled riverbed with large clusters of nodes at the particle interfaces. Presently, Hydro3D's (Ouro and Stoesser 2017) flow solver cannot compute for an unstructured geometry mesh, as more than one node could exist within the structured hexahedral fluid domain cells. Thus, the solver cannot determine which node to work with, and Hydro3D (Ouro and Stoesser 2017) terminates. Therefore, an intermediary program was required to structure the Gmsh-Raw mesh before passing the now-structured hexahedral mesh nodes to Hydro3D (Ouro and Stoesser 2017). A Matlab code called Gmsh2Hydro3D was developed as part of this study to undertake this secondary meshing and could be employed beyond Hydro3D wherever the IB method is employed, and a structured hexahedral mesh is required.

Gmsh2Hydro3D can generate the required structured mesh nodes through two different functions, both of which are fully parallelised using Matlab's Parallel Computing Toolbox. The first function, so-called Function 1, structures the mesh nodes in such a way that then requires the distance between all nodes relative to one another to be checked to ensure that no two nodes are closer in any axis than the cell dimensions of the fluid solver mesh that will be used in the LES code. The second function, so-called Function 2, structures the mesh nodes in such a way that does not require checking. Thus, making Function 2 computationally superior to Function 1, but with a trade-off against how well the mesh nodes represent the original geometry created using CAD.

The output from both functions is not only in a suitable format for the LES code to read directly, it also negates the need to re-calculate origin offsets for the placement of the geometry within the fluid domain, i.e.: an offset of 0.0 m can be used, as the node co-ordinates originally specified in the CAD program are maintained throughout the meshing process. This helps with precise placement of complex geometry within the fluid domain. However, Hydro3D (Ouro and Stoesser 2017) does include a feature that allows the re-placement of the geometry within the fluid domain by a set displacement in each axis after the meshing process has been completed.

5.3.1. Function 1

Within Function 1, structuring of the nodes is undertaken by searching the Gmsh (Geuzaine et al. 2009) output and keeping only the nodes that are closest to the

centers of the Hydro3D (Ouro and Stoesser, 2017) fluid solver mesh cells, as shown in Fig. 5.3(a). This method retains the original node coordinates output by Gmsh (Geuzaine et al. 2009) to achieve the best possible representation of the CAD model. Therefore, the representation is entirely determined by the degree of refinement set for the fluid solver mesh.

Although adjacent cells contain a single node, the distance between neighboring nodes does not necessarily conform to that required by the Hydro3D (Ouro and Stoesser 2017) fluid solver. To overcome any such issue, the distance between the nodes relative to one another are then also checked. Where clusters of nodes are found using the criterion shown in Fig. 5.3(b), a new node is created, which is the centroid of that cluster. This new node, along with those already conforming, forms the array of nodes for the next iteration. Thus, the number of nodes that is retained reduces following each iteration. Iteration continues until the Euclidean distance between the node being checked and its non-conforming neighbour is within 1% of half of a cell apart, at which point they can be considered the same node. A less stringent measure of conformity might yield the same result in less time. However, it is only through trial and error with multiple datasets of a similar size that a more reasonable conformity level can be found.

a)

$$(C_i) \oplus \quad distance = \sqrt{\sum (P_i - C_i)^2}$$

$$(P_i) \bullet$$

b)

$$(N_2)$$
$$(N_1) \bullet$$

$$\sqrt{\sum (N_1 - N_2)^2} \geq \sqrt{\sum (\frac{dx}{2}, \frac{dy}{2}, \frac{dz}{2})^2}$$
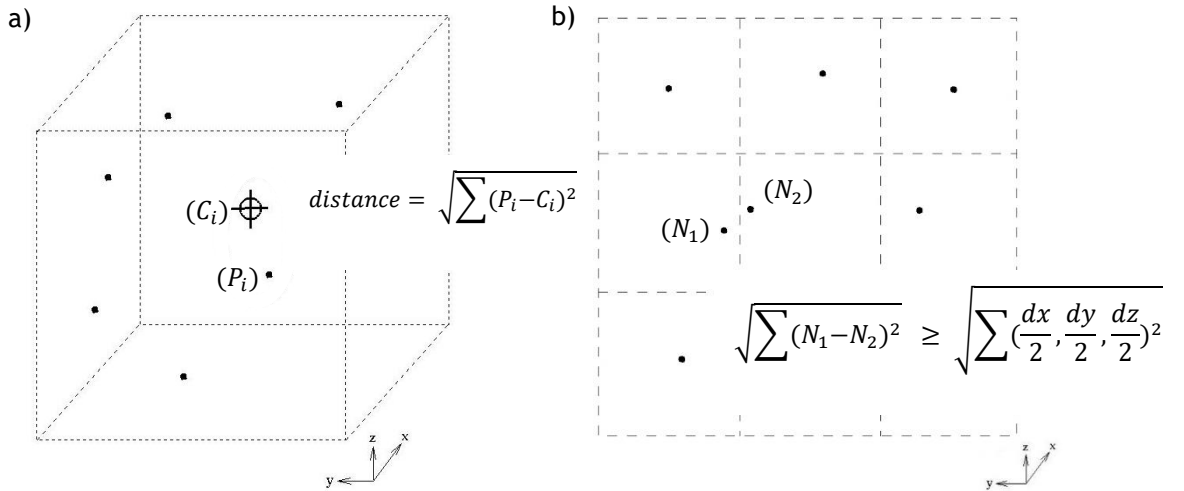
Figure 5.3. (**a**) A diagrammatic representation of a cell and the node structuring scheme where only the node $P_i(i_1, j_1, k_1)$ closest to the center of the cell $C_i(i_2, j_2, k_2)$ is saved; (**b**) A diagrammatic representation of the conformity scheme for several cells, each with dimensions dx, dy, and dz, where the nodes $N_1(i_1, j_1, k_1)$ and $N_2(i_2, j_2, k_2)$ are checked against the conformity criterion.

The output from this function is a fully structured mesh that describes the CAD geometry well and complies with the requirements of Hydro3D (Ouro and Stoesser

2017). However, the computational effort required to obtain this output is very high and is thus rendered unsuitable for large domains, complex geometry, and high resolutions, such as that used in this study.

5.3.2. Function 2

By comparison to Function 1, Function 2 is very simplistic. Structuring of the nodes is undertaken by searching the Gmsh (Geuzaine et al. 2009) output as before, however, upon finding a node within a fluid solver mesh cell, this function merely reassigns the node co-ordinates to match that of the center of the cell. Thus, negating the need to check whether the distance between all nodes relative to one another is less than the cell dimensions of the fluid solver mesh in any axis. Clearly this function is far less computationally demanding than Function 1 as it simply does not have anywhere near as many steps and processes to perform. However, as already mentioned, the greatly reduced processing time is traded-off against how well the structured mesh nodes represent the original CAD geometry. However, so long as the fluid solver mesh is sufficiently fine then the gain in reduced processing time outweighs any small deviation from the CAD output.

Within this study, Function 2 of the Gmsh2Hydro3D code was used to evaluate two different mesh resolutions, one coarse (MC) and one fine (MF) of the scaled riverbed. Table 1 provides a summary of the different meshing options that were applied in Gmsh2Hydro3D and the resulting number of immersed boundary nodes for one section of the scaled riverbed (the overall riverbed being 6 sections in total).

Table 5.1. Summary of the Gmsh2Hydro3D Function 2 meshing options applied in this study and the resulting coarse- and fine-resolution mesh versions for one section of the scaled riverbed. Both mesh versions start with 24,686,021 nodes from Gmsh (Geuzaine et al. 2009) and used 24 CPU's (12 physical Intel Xeon 2.30 GHz cores, each with 2 hyper-threads) to compute the structured nodes.

Mesh version	Resolution Description	Mesh resolution in each axis (m)			Final number of nodes from Gmsh2Hydro3D	Time taken to structure nodes (hrs)
		dx	dy	dz		
MC	Coarse	0.0100	0.0100	0.0050	338,490	2.60
MF	Fine	0.0050	0.0050	0.0025	1,411,468	21.50

The overall scaled riverbed assembly of six sections therefore consists of 2,030,940 nodes in the case of the MC coarse mesh version and 8,468,808 nodes in the case of the MF fine mesh version.

Fig. 6 shows the nodal point cloud of a representative particle of the MC mesh version for one section of the scaled riverbed, and Fig. 7 shows the same of the MF mesh version.
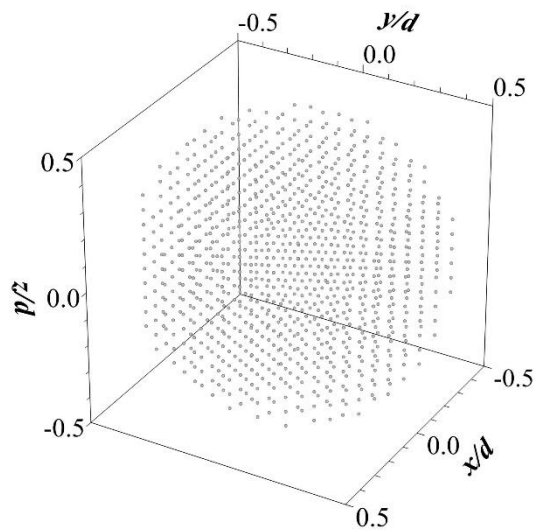
Figure 5.4. Isometric view of the nodal point cloud of a representative particle of the MC coarse mesh version following the Gmsh2Hydro3D process; the x-, y-, and z-axis are expressed in terms of particle diameters (d).
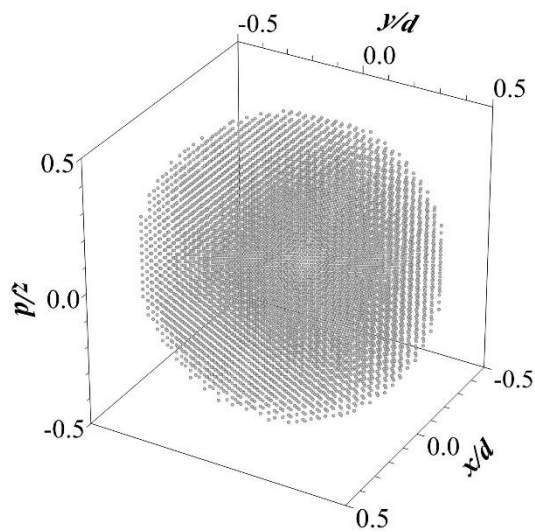
Figure 5.5. Isometric view of the nodal point cloud of a representative particle of the MF fine mesh version following the Gmsh2Hydro3D process; the x-, y-, and z-axis are expressed in terms of particle diameters (d).

Though each mesh appears visually to represent the particles well, by the very nature of the meshing process and the use of a structured hexahedral mesh combined with the use of Function 2 of Gmsh2hydro3D, the geometry will be somewhat altered from the scaled riverbed CAD model originally developed. Taking

the reasonable assumption that the Gmsh-Raw mesh represents the CAD model wholly with negligible difference, the deviation, or the Hausdorff distance, between this original mesh and the two mesh versions shown in Table 1 was calculated to provide an indication of how the Gmsh2Hydro3D process has altered the geometry compared to that originally intended.

The Hausdorff distance is a measure of the length between the point in A that is farthest from any point in B and vice versa. For which both $A = \{a_1, a_2, \ldots, a_n\}$ and $B = \{b_1, b_2, \ldots, b_n\}$ are sets of points that overlay one-another. A notable limitation of using the Hausdorff distance as opposed to other metrics of mesh similarity, such as the Fréchet distance, is that two dissimilar point sets, and thus dissimilar geometry, can present with a small Hausdorff distance and appear similar. This is because if the geometry represented by A shares numerous points of the geometry represented by B then there will be a small deviation from A to B even if the geometry is nothing alike. Given that the various mesh versions explored in this study are simplifications of the Gmsh-Raw mesh and are all therefore representing the same geometry, the Hausdorff distance was deemed suitable for use here.

The Hausdorff distance can be expressed as (Huttenlocher et al. 1993):

$$H_D(A, B) = \max\left(h(A, B), h(B, A)\right) \tag{1}$$

in which,

$$h_D(A, B) = \max_{a \in A} \min_{b \in B} \|a - b\| \tag{2}$$

where, $h_D(A, B)$ is the one-sided Hausdorff distance, $\|\cdot\|$ is the Euclidean norm of the point sets A and B.

MeshLab (Cignoni et al. 2008) was used in this study to calculate the one-sided Hausdorff distance between the two mesh versions, as well as the Gmsh-Raw mesh they originate from, as shown in Table 2.

As expected, Table 5.2 shows that the MC and MF mesh versions deviate from the original Gmsh-Raw mesh and thus, also the CAD generated scaled riverbed geometry. For the MC mesh, the maximum deviation from the Gmsh-Raw mesh is approximately 2.4%, 1.2%, and 4.7% of the section's x-, y-, and z-dimensions, respectively. Whereas, for the MF mesh, the maximum deviation from the Gmsh-Raw mesh is approximately 2.6%, 1.3%, and 5.2% of the section's x-, y-, and z-dimensions, respectively. Clearly such deviation from the original CAD design,

particularly in the z-direction of either case, is relatively large and undesirable. However, since the average deviation is significantly lower than the maximum for both cases this would suggest that there are far more nodes in either point cloud closer to the original geometry than there are further away.

Table 5.2. One-sided Hausdorff distance results for the various mesh versions calculated using MeshLab (Cignoni et al. 2008), where (A) is the sampled point set.

Compared Point Sets (A,B)	One-Sided Hausdorff Distance (mm)			
	Minimum	Maximum	Mean	RMS error
MC, Gmsh-Raw	0.00	17.05	3.02	3.51
MF, Gmsh-Raw	0.00	18.63	1.55	1.77
MC, MF	3.75	3.75	3.75	3.75

For the MC mesh, the average deviation from the Gmsh-Raw mesh is approximately 0.42%, 0.21%, and 0.84% of the section's x-, y-, and z-dimensions, respectively. For the MF mesh, the average deviation from the Gmsh-Raw mesh is approximately 0.22%, 0.11%, and 0.43% of the section's x-, y-, and z-dimensions, respectively. Such small deviations on average for both MC and MF would suggest that overall, both meshes are highly representative of the Gmsh-Raw mesh they originate from and in turn, the original CAD design. The significant difference between the average and maximum deviation for both MC and MF cases would suggest that there may exist a select region, or regions, of the geometry that are under-represented and that an even higher resolution would be required to represent that region better. However, given that on average the meshes can be deemed highly representative of the original CAD design, and the chosen mesh resolution suits not only the geometry, but also the LES and the available computational resources, the MC and MF mesh versions were deemed suitable for use in this study.

The deviation of MC from MF shown in Table 5.2 may at first appear erroneous as the maximum and minimum distance are the same value and thus, so is the mean distance and the RMS error. However, it must be remembered that the MF mesh is exactly twice as fine as the MC mesh and due to the Gmsh2Hydro3D process, the nodal coordinates of both meshes are regimented in the same fashion. Therefore, the distance from any given node in the MC mesh to the closest neighbour in the MF mesh will be the same. Hence, why the maximum and minimum distance shown in Table 5.2 are the same. This also shows that the apparent under-representation in

both meshes is equally under-represented in both, otherwise there would exist some nodes of the MC mesh that would be further/closer to their closest neighbour in the MF mesh than any other nodes and so the maximum and minimum distances could not have the same value. The deviation between the MC and MF meshes is approximately 3.75 mm, or 0.52%, 0.26%, and 1.04% of the section's x-, y-, and z-dimensions, respectively. Such a small deviation between the MC and MF meshes is important to ensure that the geometry used for the LES is similar and thus, comparable regardless of the Gmsh2Hydro3D process and the chosen resolutions.

The results of calculating the one-sided Hausdorff distance of the mesh versions used in this study shows that the Gmsh2Hydro3D process does have some effect on how well the resulting mesh represents the geometry originally designed. However, as Table 5.2 indicates, so long as the mesh resolution is sufficiently fine, the Gmsh2Hydro3D process can generate highly representative structured hexahedral nodal point clouds for use in Hydro3D, or other code that employs the IB method with a hexahedral rather than tetrahedral fluid mesh. The comparison of the MC and MF meshes with each other also indicates that the Gmsh2Hydro3D process can generate structured meshes of the same geometry at different resolutions that are similar and comparable.

The Gmsh2Hydro3D process could be further enhanced through the inclusion of Delaunay and Blossum meshing algorithms within the code. Such enhancement would negate the reliance on external meshing software to generate the initial unstructured tetrahedral mesh. Additionally, rewriting the Matlab based code to form a standalone executable written in Fortran, or other similar language, and utilising the Message Passing Interface (MPI) for parallelisation would allow very large and complex geometry to be more readily and quickly meshed using High Performance Computing (HPC) or similar technologies.

Having determined that the two different resolution nodal point clouds are highly representative of the original CAD developed scaled riverbed geometry; the degree to which the mesh versions succeed in representing a natural gravel riverbed now needs to be explored.

5.4. Porosity and Roughness Analysis

In this section, like Section 4.4 found in Chapter 4, the porosity and roughness of the large-scale riverbed CAD model are characterised in relation to natural gravel riverbeds. The roughness of the two different mesh resolution versions of the scaled

riverbed model is also evaluated to verify that the meshing process has not changed the macro characteristics from that designed and are comparable to both natural and artificial riverbeds found in the literature.

The CAD software's inbuilt volume calculator was used to aid calculation of the porosity of the large-scale riverbed model. As previously stated, the volume of voids formed on the surface of the riverbed are considered in this study to be part of the channel rather than the riverbed. As such, the uppermost volume of $0.25d \cdot l \cdot w$ was excluded from both the total volume occupied by the geometry and the overall volume of all the particles forming the bed. The total volume occupied by the geometry was found to be 0.35 m^3 and the overall volume of all the particles forming the bed was calculated as 0.24 m^3. Thus, the porosity of the scaled riverbed was found to be 32.5% using Eq. (4.1) in Section 4.4. This porosity is highly comparable to the 31.5% porosity found for the artificial riverbed, as previously discussed. Using Eq. (4.2) in Section 4.4, the void ratio of the scaled riverbed was found to be 0.48, which is not only highly comparable to that found earlier for the artificial riverbed of 0.46 but is also within the range 0.3-0.6 for natural gravels (Das, 2008), even if towards the extreme end. The high porosity combined with a void ratio towards the extreme upper end of the range found for typical natural gravel riverbeds, would suggest that the pore structure of the scaled riverbed is comparable to that of a loosely packed natural riverbed in volume, which is a key determinant of the interstitial flowrate.

So far it has been determined that the two different mesh versions are highly representative of the large-scale riverbed CAD model from which they originate, and that the porosity of that model is highly comparable to the artificial riverbed developed in Chapter 4 as well as natural riverbeds. Now the surface roughness characteristics of both the meshes and the CAD model need to be evaluated to ensure they are representative and comparable between themselves, the artificial riverbed, and natural riverbeds found in the literature.

The surface elevation data for the roughness evaluation of the scaled riverbed model was obtained from the surface of the uppermost layer of the geometry represented by the raw, extremely fine mesh resolution Gmsh (Geuzaine et al. 2009) output, or the so-called Gmsh-Raw mesh. The surface elevation data for the two different mesh resolution versions of the scaled riverbed processed by Gmsh2Hydro3D (MC and MF) was obtained by only using nodes with a z-axis coordinate greater than 315 mm (the total height of the geometry minus $0.5d$).

Table 5.3 summarises the number of nodes of each mesh version that describe only the surface under investigation.

Using Eq's. (4.3 – 4.10) in Section 4.4, the standard deviation, Fisher-Pearson coefficient of skewness, and excess kurtosis, as well as the confidence intervals and errors associated with such calculations were found for the surface elevations, $z(x, y)$, of each mesh version, as summarised in Table 5.4. Note that the standard deviations of the surface elevations of each mesh version shown in Table 5.4 were calculated using the entire population of the nodes and thus, confidence intervals need not be calculated.

Table 5.3. The number of nodes that describe the surface geometry of each of the mesh versions explored in this study.

Mesh Version	N
Gmsh-Raw	2,498,262
MC	37,084
MF	150,427

Table 5.4. Bulk statistics of the uppermost particle layer of the various mesh versions investigated in this study.

Mesh Version	σ_z (mm)	Sk_z (-)	Ku_z (-)
Gmsh-Raw	11.69	-0.028 (± 0.0015)	-1.011 (± 0.0031)
MC	11.31	-0.024 (± 0.0127)	-0.984 (± 0.0254)
MF	11.23	-0.007 (± 0.0063)	-0.946 (± 0.0126)

As Table 5.4 shows, all the mesh versions exhibit similar bulk statistics, which is to be expected as they are all derivatives of the Gmsh-Raw mesh, which again is reasonably assumed here to represent the scaled riverbed CAD geometry with negligible difference. The minor variability in the standard deviation of the surface elevations across the three mesh versions displayed in Table 5.4 makes sense due to the variation in the mesh resolutions employed for each version giving rise to different degrees of geometry capture, particularly at the extremes of surface roughness, ie: the crests and the troughs.

The standard deviation of the surface elevations of each mesh version shown in Table 5.4 may at first appear quite large, especially in comparison with the artificial riverbed explored in Chapter 4 with a standard deviation of just 3.81 mm. However, the scaled riverbed has an average particle diameter of 90 mm, over 3 times larger than the artificial riverbed. Therefore, some variance in the particle diameter of

approx. 12.5% seems reasonable and is congruent with 13.61% variability found in the surface elevations of the artificial riverbed described in Chapter 4.

The skewness of all the mesh versions shown in Table 5.4 is negative, but well below -0.5 and thus, the distribution of the surface elevations for all the mesh versions can be considered symmetrically distributed even with allowing for a margin of error. However, the negative kurtosis for all mesh versions shown in Table 5.4 gives a good indication that though the surface elevations may be symmetrically distributed, the variance of the distribution is less than found in a normal distribution with fewer irregularities in the surface elevations. This again corresponds well with that found for the artificial riverbed investigated in Chapter 4, as well as in comparison with each other, as all the mesh versions exhibit similar characteristics.

As explained for the artificial riverbed in Chapter 4, greater variability in the geometry and therefore reduced skewness and kurtosis and increased standard deviation of the surface elevations for all the mesh versions would be desirable to better represent a natural gravel riverbed with well graded particle sizes. However, with a need to create immersed boundary geometry that was a scaled approximate of the artificial riverbed applied in experimentation, statistical characteristics that were alike were of greater need than a more realistic representation of a natural gravel riverbed which otherwise could have been achieved.

It therefore appears that in terms of the bulk statistics the two different resolution mesh versions compare very well with each other, the artificial riverbed, and scaled riverbed CAD model geometry that they represent, irrespective of the meshing process. However, that is not to say that if different mesh resolutions, or different levels of simplification, were to be used that the statistical characteristics of the geometry would remain unchanged. It would seem logical that some simplification of complex geometry, such as the scaled riverbed model, would result in some change in the surface roughness as it becomes less well defined and geometric extremes, which greatly influence surface roughness, become less pronounced as a result. Therefore, a roughness geometry function $A(z')$ (Stoesser, 2010 and Nikora et al. 2001), which describes the cumulative probability distribution of $z(x, y)$, was employed to further investigate the roughness characteristics of the various mesh versions of the scaled riverbed.

Fig. 5.6 shows $A(z')$ plotted as a function of surface elevation fluctuation zb' for all the mesh versions as well as an idealised normal distribution at various offsets to allow distinguishability between the data plots. As expected from the skewness

results shown in Table 5.4, the distribution of surface elevations for all mesh versions are indeed normal and near indistinguishable. Thus, it seems reasonable to consider the scaled riverbed, in all guises, as having a distribution of surface elevations that is representative of that found in natural gravel riverbeds at large (Aberle, 2007 and Aberle and Nikora, 2006). Equally, it seems reasonable to suggest that the meshing process has had little to no effect on the distribution of surface elevations even at disparate mesh resolutions. It is therefore also reasonable to characterise the surface of the Reynolds riverbed in all guises as rough. However, further analysis is required to determine the degree of roughness.

Calculation of the Power Spectral Density (PSD), similarly undertaken in Section 4.4 found in Chapter 4, of the surfaces of the various mesh versions of the scaled riverbed allows for graphical representation of the distribution of the roughness. As previously explained, the Hurst exponent, H, which is a key determinant of surface roughness, is given by the slope of a linear regression line fitted to data within the region $k > k_0$ of a PSD, where $k_0 = 2\pi/\lambda_0$ is the short distance cutoff and λ_0 is the largest particle size used. Since all the mesh versions of the scaled riverbed originate from the same geometry with a particle diameter of 90 mm, they all have the same short distance cutoff of 0.038. By applying a Fast Fourier Transform (FFT) Matlab function (Kanafi, 2016) to the surfaces of the two mesh versions of the scaled riverbed, the PSD of each was found, as shown in Fig. 5.7.
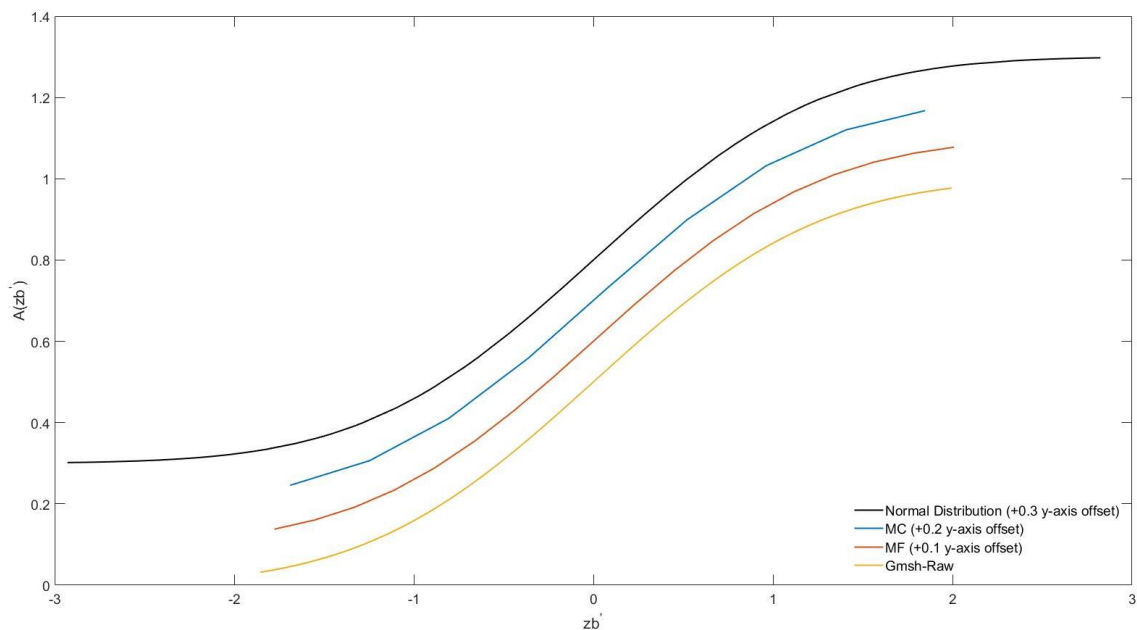
Figure 5.6. Cumulative probability distribution of surface elevations for all mesh versions at various offsets for distinguishability.

For ease of comparison, Fig. 5.7 also shows the PSD of the surface of the artificial riverbed that was calculated earlier in Section 4.4. The Hurst exponent that was found for each mesh version and is summarised in Table 5.5.
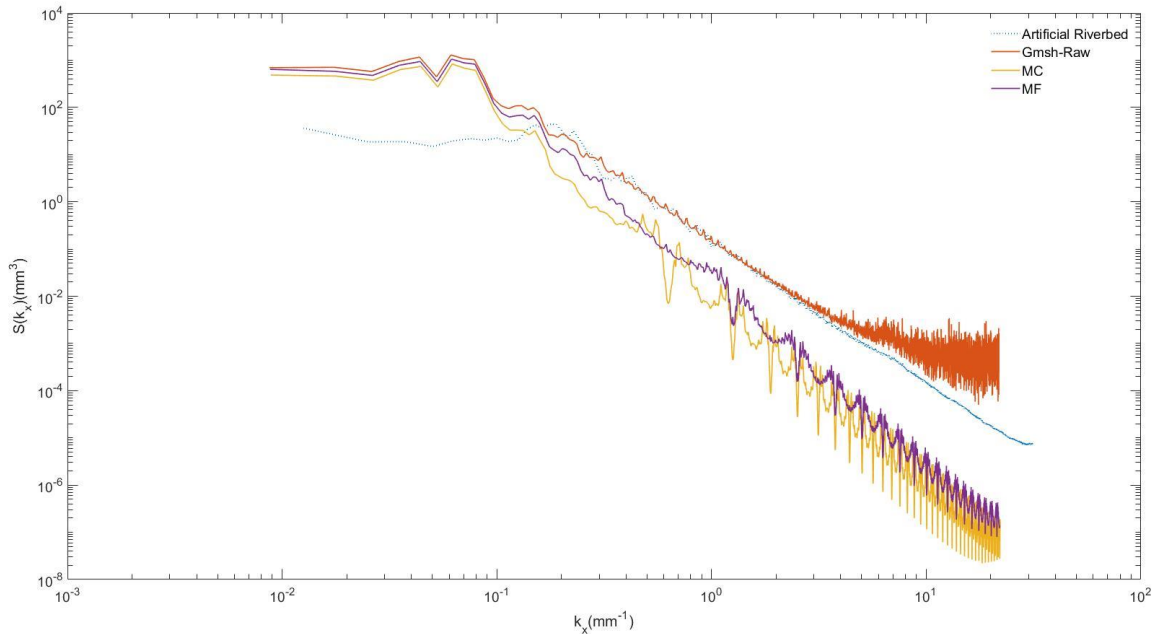
Figure 5.7. One-dimensional surface roughness PSD of the surfaces of the scaled riverbed mesh's Gmsh-Raw, MC, and MF, as well as the PSD of the surface of the artificial gravel riverbed.

As Table 5.5 shows, the value of H for the Gmsh-Raw mesh version is less than unity and can be considered fractal at some scales (Kanafi, 2016). However, the MC and MF mesh versions cannot be considered fractal at any scale with H values greater than unity. Though the H of the Gmsh-Raw mesh version is highly representative of gravel placed within a flume (0.50 ± 0.07) the Hurst exponents of the MC and MF meshes are almost twice that found in natural gravel-bed streams (0.79 ± 0.04) (Nikora, et al. 1998) (p. 522).

It is therefore clear that though the distribution of the roughness elements making up the surface of the different mesh versions may well be very similar to natural gravel riverbeds; and though the Gmsh-Raw mesh may exhibit a highly comparable roughness magnitude to that found in nature; once processed through the Gmsh2Hydro3D routine, the MC and MF meshes exhibit a roughness magnitude that is far less than that found in nature.

It therefore seems reasonable to characterise the scaled riverbed, in terms of the MC and MF mesh versions that will be used in CFD simulations discussed in Chapter 6, as having a pore structure and surface roughness distribution

61

representative of a natural gravel riverbed, whilst exhibiting a surface roughness magnitude lower than that found naturally.

Table 5.5. The Hurst exponent for various mesh versions of the scaled riverbed given by the slope of linear regression line fitted to the PSD of the corresponding surface.

Mesh Version	H
Gmsh-Raw	0.5185
MC	1.4330
MF	1.4305

As shown in Table 5.5, the Hurst exponent varies considerably across the mesh versions of the scaled riverbed. It appears that the meshing process, in particular the chosen mesh resolution, has a large influence on the H of the resulting surface, so much so that the MC and MF meshes have H value's some 76% higher than the Gmsh-Raw mesh they originate from and thus, exhibit a lower surface roughness. Though it should be noted that the H values of the MC and MF meshes are only approx. 48% higher than the artificial riverbed suggesting somewhat more comparable surface roughness. Equally, and perhaps most importantly, the meshes exhibit almost the exact same magnitude of surface roughness. Therefore, when applied to the study of turbulent flow using LES in Chapter 6, it is likely that with all else being the same, the turbulent phenomena generated as a result of the surface geometry, regardless of the mesh version used, will be comparable and in similar proportion.

Since all the mesh versions have the same distribution of roughness throughout their surface, as shown in Fig. 5.6, and the H values of both the MC and MF mesh versions are the same, the results shown in Table 5.5 suggest that either the process of structuring the nodes described in Section 5.3.2 significantly changes the surface roughness characteristics of the geometry, or something else is happening. As already determined through the calculation of the Hausdorff distances in Section 5.3.2, neither mesh versions deviate greatly from the Gmsh-Raw mesh even with disparate resolutions and thus, approximate the scaled riverbed CAD model very well. Instead, the very nature of structuring the nodes to remove clusters at particle interfaces may be the cause of the variations in H shown in Table 5.5. By completely removing node clusters, Gmsh2Hydro3D also removes any influence vast numbers of nodes with very similar elevations (as the interface between particles would tend to be around the same point on most particles given, they are of similar size) could

have on the PSD calculation from which H is obtained. As shown in Table 5.3, the number of nodes that represent the surface of the MC and MF meshes is between 1.4% and 6.0%, respectively of that representing the surface of the Gmsh-Raw mesh. Though so few nodes may be able to represent the original scaled riverbed CAD model very well and at a resolution suitable for the LES, as will be explained further in Chapter 6, it appears that an even finer resolution would be required to better represent the roughness surface in mathematical terms. However, with comparable geometry, porosity, and bulk statistical characteristics, as well as a need to balance computational effort in terms of the LES, and highly comparable roughness between the two mesh versions, it appears reasonable that both mesh versions are considered ideal for use in this study.

For future work a far rougher riverbed geometry would be highly desirable to better represent a natural gravel riverbed but may require an even finer resolution than applied here, or the application of a sharp interface immersed boundary method, to be realised in the LES or reflected in the statistical analysis undertaken here.

5.5. Summary

In this chapter, a CAD model of a gravel riverbed matrix 0.36 m in depth, 1.44 m wide and 0.72 m long was created with an average particle diameter of 90 mm. A numerical approximation was generated by applying a meshing algorithm to the CAD model geometry using the open-source program Gmsh (Geuzaine et al. 2009). The resulting unstructured, tetrahedral mesh was then re-meshed using the code Gmsh2hydro3D, which was developed as part of this study, to give two structured, hexahedral mesh versions at different resolutions suitable for application in the LES code Hydro3D (Ouro and Stoesser, 2017). The two different resolution mesh versions, MC and MF, were analysed in comparison to the geometry from which they originate, which was assumed here to be wholly represented by the extremely fine resolution output from Gmsh, the so-called Gmsh-Raw mesh, as well as natural and artificial riverbed data found in the literature.

The main conclusions are:
- The Hausdorff distance was calculated and showed that the average deviation of the MC mesh from the Gmsh-Raw mesh is approximately 0.42%, 0.21%, and 0.84% of the section's x-, y-, and z-dimensions, respectively. In a similar

fashion, the average deviation of the MF mesh from the Gmsh-Raw mesh is approximately 0.22%, 0.11%, and 0.43% of the section's x-, y-, and z-dimensions, respectively. Such small deviations for both MC and MF suggest that both meshes are highly representative of the Gmsh-Raw mesh they originate from and in turn, the original scaled riverbed CAD design.

- The Hausdorff distance was also used to show that the deviation between the MC and MF meshes is 0.52%, 0.26%, and 1.04% of the section's x-, y-, and z-dimensions, respectively. Such a small deviation between the MC and MF meshes shows that regardless of the difference in the resolution, both geometries are similar and comparable.

- The results of calculating the Hausdorff distances for the geometry used in this study also highlights that, so long as the mesh resolution is sufficiently fine, the Gmsh2Hydro3D process can generate highly representative structured hexahedral nodal point clouds that are ideally suited for use in Hydro3D (Ouro and Stoesser, 2017).

- The porosity of the scaled riverbed CAD model was calculated as 32.5%, which compares well with the values found in the literature for natural gravel-bed surfaces as well as the artificial riverbed previously developed as part of this study. Additionally, the void ratio was found to be 0.48, which although at the extreme end due to the lack of smaller particles, is within the maximum and minimum range for typical gravel riverbeds and therefore shows that the scaled riverbed's pore structure is comparable to that of a natural gravel riverbed.

- The standard deviation of the Gmsh-Raw surface elevations was found to be 11.69 mm. Thus, suggesting that the variance in particle diameter in the scaled riverbed CAD model is less than that found in natural rivers, yet highly comparable to that found for the artificial riverbed by percentage of the particle diameter used for each model.

- The standard deviation of the MC and MF mesh versions was found to be 11.31 mm and 11.23 mm respectively which is very similar to the Gmsh-Raw mesh from which they originate showing the Gmsh2Hydro3D process had little effect on the bulk statistical characteristics of the geometry.

- The skewness and kurtosis of the Gmsh-Raw mesh was calculated as –0.028 and –1.011, respectively. Similarly, the skewness and kurtosis of the MC and MF mesh versions was calculated as -0.024 and -0.984, and -0.007 and -0.946, respectively. These skewness results suggest that the surface elevations of the Gmsh-Raw and the MC and MF derivatives are normally distributed and

symmetrical, as confirmed by a cumulative probability distribution plot of the surface elevations of each. The negative and relatively large kurtosis relates to the lack of variance in the particle diameters used in the scaled riverbed CAD model, and thus, the lack of irregularities in the surface elevations.

- A power spectral density function was applied to the surface elevations of the Gmsh-Raw, MC and MF meshes, giving a Hurst exponent of 0.5185, 1.4330, and 1.4305, respectively. Thus, the MC and MF mesh versions that will be used in CFD simulations discussed in Chapter 6 exhibit a degree of roughness lower than that found in nature, meaning the hydraulic resistance and friction factor will, as a result, be lower than desired. However, these characteristics are sufficiently comparable to the artificial riverbed previously created in the study and thus, deemed appropriate for use in the LES investigation explored further in Chapter 6.

The results presented in this chapter show that the developed Gmsh2Hydro3D process can offer the numerical approximation, so long as the resolution is sufficiently fine, of highly complex geometry without significantly changing the characteristics of that geometry. Also, the results of analysing the developed scaled riverbed show that it is somewhat comparable to the previously created artificial riverbed. The scaled riverbed can be characterised as being like a natural gravel riverbed with a lower surface roughness, as well as reduced particle size variance, comparable particle distribution, and porosity within limits, but at the extreme end of the scale.

Chapter 6

6.   LES of Porous Bed Turbulent Flow

6.1. Aims and Objectives

This chapter aims to further explore near-bed and interstitial turbulent flows associated with porous media through numerical simulation using the LES code Hydro3D (Ouro and Stoesser, 2017) with the goal of quantifying the effects of porosity and roughness on the flow characteristics. This will be achieved through spectral analysis of the velocity fluctuations, analysis of statistics associated with turbulent momentum flux at the surface-bed interface, as well as the TKE budget terms both in the near-bed region and within the bed itself.

The following section describes in detail the numerical setup of the simulations. This is followed by validation of the characteristic flow statistics, such as the mean velocity profile, Reynolds stresses, skewness, and kurtosis against experimental data found in the literature. An exploration of Taylor's hypothesis then follows including presentation of the convection velocity profile, correlation coefficient profile, the variance of spatial and temporal derivatives with elevation, as well as spectra profiles and contours. Analysis of the mean velocity TKE and TKE budget terms are then shown. Finally, conclusions are drawn and areas for future research are highlighted.

6.2. Numerical Setup

Two simulations of the same scenario, both but at different resolutions, one at a coarse resolution, LES-C and the other at a fine resolution, LES-F are conducted in this study. The overall domain for both cases measures in the x-, y-, and z-

directions $48d$, $16d$, and $8d$, respectively as shown in Fig. 6.1(a), where d is the nominal particle diameter of 0.09 m. In terms of the bed depth, it should be noted that there are 5-particle layers in the z-direction as shown in Fig's. 6.1(a) and (b), but due to the jointing between layers the overall bed depth is only equal to $4d$, as highlighted in Fig. 6.1(a) by the z-axis range.

In terms of surface flow depth, h, defined in Fig. 6.1(b), the domain measures $12h \cdot 4h \cdot 2h$. The domain used in this study is significantly larger, particularly in the x-direction, than the typically applied dimensional criterion of $2\pi h \cdot \pi h \cdot h$ to ensure all scales of turbulent flow are captured within the computational domain. This is because the flow in this study is expected to be highly turbulent and the typically applied criterion is considered somewhat conservative to capture all scales of turbulent motion (Bomminayuni et al. 2014). That said, the applied domain dimensions still might not be sufficient to capture so-called Very Large-Scale Motions (VLSM), but the computational effort required to further increase the domain size was beyond that available to this study.
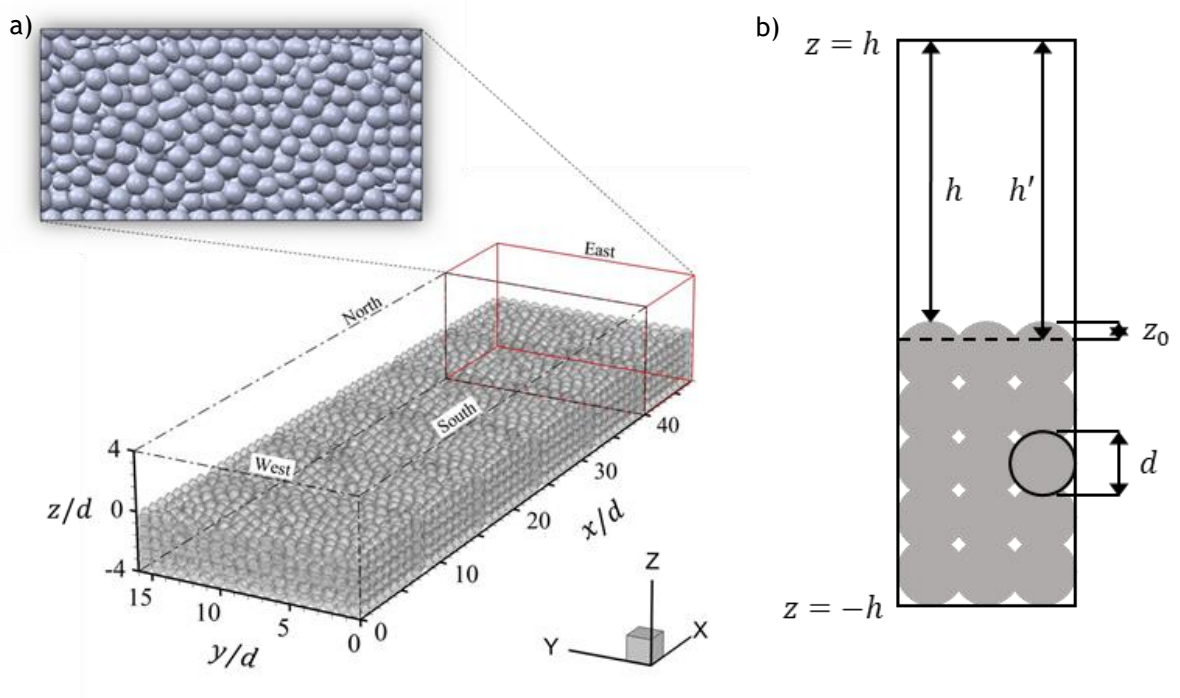
Figure 6.1. (a) A diagram showing the computational domain with the scaled riverbed geometry in place, boundary labels and x,y,z dimensions expressed in terms of the particle diameter, d. The streamwise direction is in the positive x-direction, or from the West boundary towards the East; **(b)** Definition of flow depth (h), particle diameter (d), zero-plane displacement (z_0), and flow depth accounting for the zero-plane displacement (h').

The naturalistic bed geometry, of height h, was generated following the methodology explained by Stubbs et al. (2018) and laid out in Chapter 5 with a porosity of 32.5%. The LES-C case used the MC mesh geometry described in Chapter 5 with a Hurst exponent, which is an indicator of surface roughness characteristics (Nikora et al. 2001 and Stoesser, 2010), of 3.866. Similarly, the LES-F mesh used the MF mesh geometry described in Chapter 5 with a Hurst exponent of 3.861. Additionally, the degree to which the bed geometry deviated from that originally designed using CAD was found, as explained in Chapter 5, through calculation of the Hausdorff distance between the nodal point clouds of the respective meshes and was found to be approximately 0.42%, 0.21%, and 0.84% of the section's x-, y-, and z-dimensions for the MC mesh and approximately 0.22%, 0.11%, and 0.43% for the MF mesh. The Hausdorff distance was also calculated to show that the average deviation of the MC mesh from the finer MF mesh is 0.52%, 0.26%, and 1.04% of the section's x-, y-, and z-dimensions, respectively. Such a small deviation on average between the two meshes and from the CAD model they originate from highlights that regardless of the difference in the resolution, both geometries are geometrically similar, representative, and most critically, highly comparable.

For the coarse LES-C case, the number of uniformly spaced computational cells in the streamwise direction, N_x was 432; in the spanwise direction, N_y was 144; in the vertical direction, N_z was 144 giving approximately 8.96 x 10^6 computational cells in total. Similarly, for the fine LES-F case, the domain was discretised by 864 x 288 x 288 cells in the streamwise, spanwise, and vertical directions, respectively giving approximately 71.66 x 10^6 computational cells in total. For both simulations, the domain was split into 108 sub-domains with $18 \cdot 6 \cdot 1$ divisions in the x-, y-, and z-directions, respectively for the purpose of spreading the computational effort across multiple processor cores. In having only one division in the vertical direction, each sub-domain and thus in turn each processor, had equal portions of channel and bed, as well as similar numbers of immersed boundary nodes. This is an important factor in trying to balance both the memory and processing requirements of the simulations overall across all the processors. In both cases 2 Intel Xeon Gold 6248 2.5 GHz physical processor nodes with a total of 80 cores were utilised. Each node had a memory allocation of 192 GB of 2933 MHz DDR4 RAM with the LES-C case requiring approximately 6 GB of RAM per core spread across 54 cores and the LES-F case requiring approximately 22 GB of RAM per core spread across 12 cores. The number of cores employed by each case was determined by the RAM requirements of the IB routine within Hydro3D. Due to the present lack of scalability of the IB

routine within Hydro3D, when the total number of immersed boundary markers exceeds approximately 1 million, increasing the number of sub-domains and thus, the number of cores they are spread over, exponentially increases the RAM required to run the simulation. This is due to the present broadcasting of all IB markers to all processors regardless of whether that processor needs all the marker information to process the IB routine. Changing the way slave processors communicate with the master processor would dramatically improve the scalability of Hydro3D when using large numbers of IB markers. For cases with few IB markers Hydro3D remains scalable as the increased RAM requirements scale within reason of the available computational resource. With close to 8.5 million IB markers, the LES-F simulation was highly limited in terms of scalability which dramatically increased the runtime of the case thus making it highly computationally expensive.

Table 6.1. Modelling options for both LES-C and -F simulations.

Case	Nx	Ny	Nz	dx+	dy+	dz+	Multi-grid
LES-C	432	144	144	31.00	31.00	15.50	3
LES-F	864	288	288	16.48	16.48	8.24	4

where, dx+, dy+, and dz+ are the grid spacings expressed in wall units in the x-, y-, and z-directions, respectively.

The computational resolution and sub-domain divisions allowed 3 multigrid steps to be used in the LES-C case and 4 in the LES-F case. The chosen number of multigrid steps helps the simulation to reach a converged solution to the Poisson equation at each timestep with less computational effort. This is a particularly important factor during the initialisation of the simulations. As explained in Section 3.3 found in Chapter 3, Hydro3D (Ouro and Stoesser, 2017) enforces the Courant-Friedrichs-Lewy (CFL) condition to ensure model stability through a CFL number which was set to 0.3 for the LES-C case, and 0.5 for the LES-F case. The various modelling options applied in both simulations are summarised in Table 6.1.

Periodic boundary conditions were applied in both the streamwise and spanwise directions; the geometry also has matching periodic faces. The top of the domain was defined by a frictionless planar rigid lid and a slip boundary condition was applied to the bottom of the domain. A free-surface approach using such methodology as the Level-Set Method could have been applied as opposed to a rigid-lid. However, with both cases already being highly computationally expensive it was far beyond the computational resource available to this study to investigate the same cases under free-surface conditions. The boundary conditions that were

applied here allow the domain to be considered as a part of a larger entity and thus, the mean flow can be considered two-dimensional and without secondary currents. A no-slip boundary condition was also applied to the surfaces of the scaled riverbed geometry through the forcing implemented through the IB method and rigorously validated by Cevheri et al. (2016). The flow was driven by a pressure-gradient, $\frac{dp}{dx}$ arising from the component of gravitational acceleration parallel to the channel bed. Importantly, the pressure-gradient is calculated in this study based solely upon the surface flow region, defined as $z/h > 0$.

Table 6.2. Prescribed hydraulic parameters for both LES-C and -F simulations.

h (m)	U_s (m/s)	U_B (m/s)	S_0	Re_b	$1/\upsilon$	h/d	b/h	Fr
0.36	1	0.1	0.001	15,000	41,667	4	4	0.53

where, S_0 is the bed slope, υ is kinematic viscosity and $1/v = Re_b/(U_s h)$, b is the channel width, and Fr is Froude number given by $U_s/\sqrt{gh}$, in which g is gravitational acceleration.

A uniform free-stream velocity could have been applied at the inlet boundary (the West wall as shown in Fig. 6.1(a)) (e.g. Fang et al. (2018)). However, such a condition would result in bed flow being of the same magnitude as the surface flow during the initialisation of the simulations. The bed flow would only reduce to a more reasonable level over the course of the simulation due to the effects of having a no-slip boundary condition at the surfaces of the bed geometry. The computational effort required to reach a more reasonable bed flow condition is beyond the resources available during this study. As such, during the initialisation of both simulations the surface and bed flows were split at the uppermost crest of the bed geometry and for $z/h > 0$, the surface bulk velocity, U_S was set to 1 m/s and distributed across the surface flow inlet through the application of a 1/7th power law, as shown in Fig. 6.2. For $z/h \leq 0$ the bed bulk velocity, U_B was set to 0.1 m/s, or 10% of the free-stream velocity, and linearly distributed in two distinct regions across the bed flow inlet based upon the elevation, as shown in Fig 6.2. The bulk Reynolds number, Re_b based upon the surface bulk velocity and the free-stream channel depth of h was 15,000 for both cases. The hydraulic parameters of both simulations are summarised in Table 6.2.
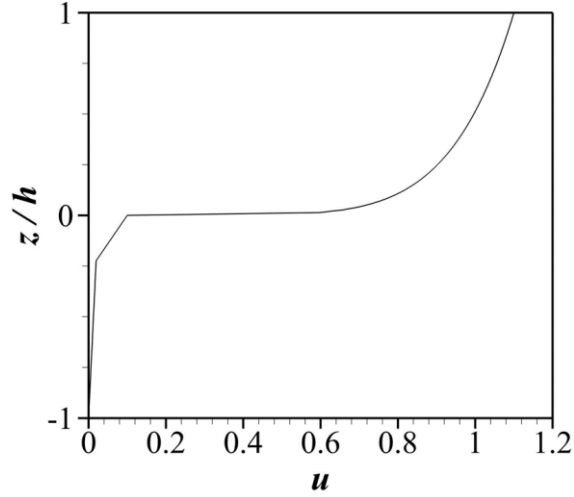
Figure 6.2. The vertical distribution of the inlet streamwise velocity profile applied during initialisation of both simulations.

The permeability Reynolds number, Re_K for both cases was calculated using Eq. 1 (Breugem et al. 2006) and found to be 6.07 for LES-C with a shear velocity, u_* of 0.0744 m/s, and 6.45 for LES-F with u_* = 0.0791 m/s, as shown in Table 6.3.

$$Re_K = K^{0.5}u_*/\upsilon \tag{6.1}$$

in which,

$$K = d_p^2\varepsilon_c^3(1 - \varepsilon_c)^{-2}/180 \tag{6.2}$$

and,

$$u_* = (\tau/\rho)^{0.5} \tag{6.3}$$

where, K is permeability, in which $d_p = \frac{6V_p}{A_p}$ is mean particle diameter, V_p is geometry volume, A_p is geometry surface area, and ε_c is porosity; and u_* is shear velocity, in which $\tau = H\frac{dp}{dx}\rho$ is bed shear stress, and ρ is fluid density; and υ is kinematic viscosity.

71

Table 6.3. Derived hydraulic parameters for both LES-C and -F simulations.

Case	u_*	Re_K	Re_D	Re_F
LES-C	0.0744	6.07	279	1116
LES-F	0.0791	6.45	299	1196

where, Re_D is the roughness Reynolds number given by $\frac{u_* d}{v}$ and Re_F is the friction Reynolds number given by $\frac{u_* h}{v}$.

Both simulations were initially run with variable timesteps for approx. 100 FT, where FT is the flow through period equal to (L_x/U_S), to allow the flow to become fully developed and the simulations well converged. LES-C was then run for a further 200 FT with a fixed timestep of 0.0015. LES-F was also run for a further 40 FT with a fixed timestep of 0.001. Further running of LES-F would be desirable but was beyond the computational resource available in this study. The chosen timesteps were based upon the average timestep of the preceding simulation runs. First- and second-order turbulence statistics were gathered whilst the simulations were operating with fixed timesteps and continued through to the end. Instantaneous velocity and pressure data were also gathered during the final 40 FT of both simulations through the application of planes and probes. Streamwise data was gathered using 4 longitidunal planes (P1-P4) positioned $4d$ apart starting at $1d$ in the y-direction, as shown in Fig. 6.3. Spanwise data was gathered at $1.5H$ with 2 cross-sectional lines (L1 and L2) positioned at $12d$ and $28d$ in the x-direction, respectively, as shown in Fig. 6.3.
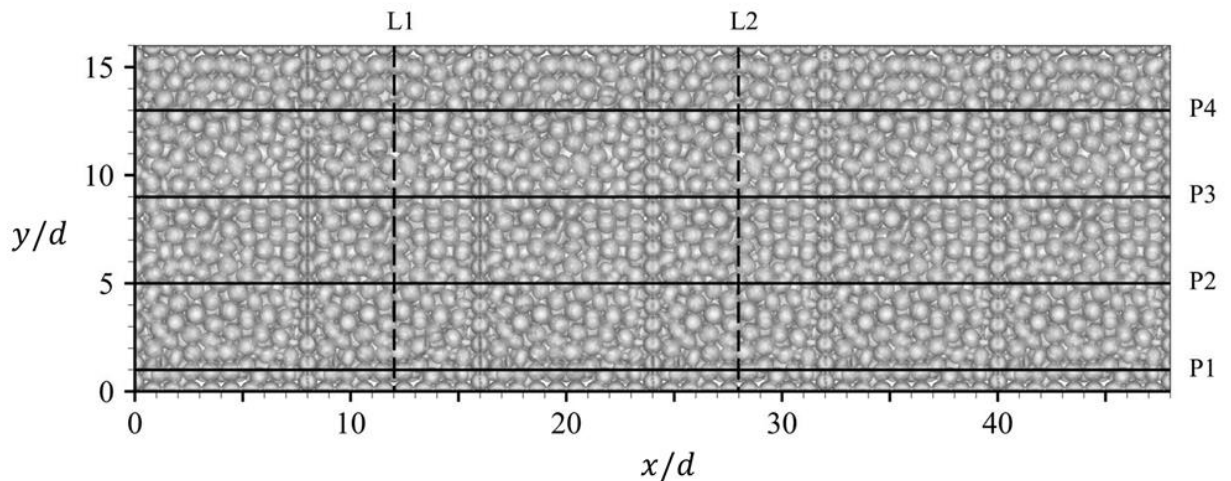
Figure 6.3. A diagram showing the layout of the planes (P1-P4) and lines (L1 and L2) used to gather instantaneous data during both cases LES-C and LES-F for 40 FT.

Table 6.4. Time series probe x- and y-axis coordinates for Section 1 of the domain.

Time Series Probe	x (m)	y (m)		Time Series Probe	x (m)	y (m)	
T1	0.250	0.320		T71	0.295	1.140	
T2	0.460	0.850		T72	0.475	1.110	
T3	0.340	0.800		T73	0.225	0.675	
T4	0.360	0.450		T74	0.470	0.245	
T5	0.180	0.790	Applied in both LES-C and LES-F	T75	0.455	0.050	
T6	0.480	0.450		T76	0.320	0.330	
T7	0.230	1.110		T77	0.405	0.465	
T8	0.470	0.370		T78	0.465	0.690	
T9	0.190	0.200		T79	0.415	0.715	
T10	0.530	0.640		T80	0.410	1.180	Applied only in LES-F
T61	0.195	1.010		T81	0.325	1.225	
T62	0.350	1.000		T82	0.045	1.190	
T63	0.450	1.405		T83	0.115	1.405	
T64	0.445	0.780		T84	0.220	1.175	
T65	0.585	0.920	Applied only in LES-F	T85	0.535	1.005	
T66	0.635	0.185		T86	0.655	1.155	
T67	0.160	0.915		T87	0.605	1.055	
T68	0.670	0.645		T88	0.580	0.270	
T69	0.475	0.915		T89	0.495	1.295	
T70	0.195	1.095		T90	0.535	0.615	

Table 6.5. Time series probe x-axis coordinate offsets per domain section.

Domain Section - Probes	x-axis offset (m)		Domain Section - Probes	x-axis offset (m)	
Section 1 – T1-T10	+ 0.00		Section 1 – T61-T90	+ 0.00	
Section 2 - T11-T20	+ 0.72		Section 2 – T91-T120	+ 0.72	
Section 3 - T21-T30	+ 1.44	Applied in both LES-C and LES-F	Section 3 – T121-T150	+ 1.44	Applied only in LES-F
Section 4 - T31-T40	+ 2.16		Section 4 – T151-T180	+ 2.16	
Section 5 - T41-T50	+ 2.83		Section 5 – T181-T210	+ 2.83	
Section 6 - T51-T60	+ 3.60		Section 6 – T211-T240	+ 3.60	

Point data was also gathered at 60 probe locations throughout the depth of the domain for both cases. The domain was divided into 6 similar sections in the streamwise direction, each $8d$ long, with 10 probes positioned in each. The x- and y-axis coordinates of probes T1-T10 positioned in the first section are shown in Table 6.3.

Probes T11-T60 have the same y-coordinates as shown in Table 6.3, but are offset in the x-axis, as shown in Table 6.4. During the LES-F case an additional 180 probes (giving 240 probes in total) were also applied in a similar fashion with the x-y-coordinates of the additional probes T61-T90 positioned in the first section also shown in Table 6.3. and the sectional offsets of probes T91-T240 shown in Table 6.4. These additional 180 probes were positioned to best capture the velocities within the pores of the bed geometry, particularly within the uppermost layers of the bed particles.

6.3. Results and Discussion

6.3.1. Validation and Grid Sensitivity

For validation and statistical analysis of the simulation results, spatial averaging $\langle \cdot \rangle$ over the $x - y$ plane of the temporarily averaged $(\overline{\cdot})$ flow quantities were undertaken before secondary averaging of the resulting $y - z$ plane provided Double Averaged (DA) profiles, denoted by $\langle \overline{\cdot} \rangle$, throughout the flow depth.

Following the methodology of Nikora et al. (2002), the log-law fitting undertaken here was provided unambiguously through the relation $(\delta \langle \overline{u} \rangle / \delta z)^{-1} = \kappa(z + z_0)/u_*$ which allows direct determination of the existence and bounds of the logarithmic region and the values of z_0, the zero-displacement, and κ, von Karman's constant. As Fig. 6.4(a) shows, the velocity gradient derivatives of LES-C and LES-F fit the logarithmic equation, as indicated by the dashed linear profile, very well in the region $0.125 \leq (z + z_0)/h' \leq 0.5$ with $\kappa = 0.36$, and zero-displacements of 6.2 mm and 13.5 mm, respectively. It is not surprising that the von Karman's constant deviates from the expected norm for boundary layer flow (i.e. $\kappa = 0.38$) due to the low-relative submergence conditions ($h/d = 4$) the simulations were conducted under and the inverse relation between increasing Re_k and decreasing κ as shown by (Dittrich and Koll, 1997). This relationship was additionally shown by Suga et al. (2010) and Fang et al. (2018) and appears to be reflected in the results shown here.

Like Cameron et al. (2017) also noted for a range of cases with different relative submergences and Reynolds numbers, the upper bound of the agreement between the LES results and the log-law highlighted in Fig. 6.4(a) is more than three times that commonly found ($z/h \approx 0.15$) for smooth-bed flow, or rough bounded flows under intermediate or high-relative submergence. The reason behind the observed agreement with the log-law so far from the bed in flows with low relative submergence is an area requiring further study.
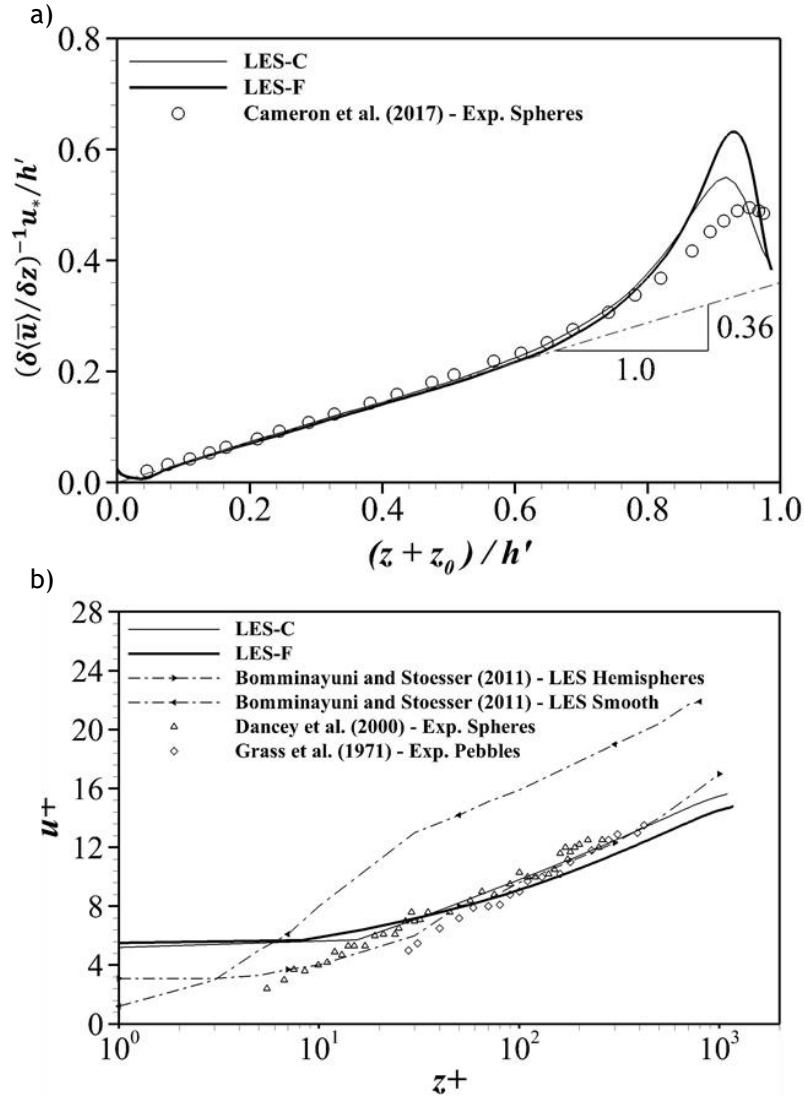
Figure 6.4. (a) Normalised inverse velocity derivative against normalised elevation for LES-C and LES-F, as well as case H050 of Cameron et al. (2017); **(b)** $u^+ = \langle \bar{u} \rangle / u_*$ against $z^+ = z u_* / v$ for LES-C and LES-F as well as the literature.

The relatively small z_0 ($0.07d$) found for LES-C appears to reflect the lack of variance in the surface roughness heights (Shen et al. 2020) highlighted by the standard deviation of the particles in the surface layer of the geometry mesh being 12.5% of the nominal particle diameter. However, at approximately twice the displacement, the z_0 of $0.15d$ obtained for the LES-F case appears somewhat less dependent upon the surface elevations and may be more of a function of the higher resolution.

As Fig. 6.4(a) shows, there is good agreement between the experimental results of Cameron et al's. (2017) H050 case, which was conducted over a single permeable layer of spherical particles, and both the LES-C and LES-F results in the region (z +

$z_0)/h' \leq 0.7$. Beyond this region, as the elevation tends towards the surface, the inverse velocity derivative increases to a slightly higher peak level than that observed by Cameron et al. (2017). This higher peak is in part due to the higher value of U_S at 1 m/s being used compared to Cameron et al. (2017) at 0.463 m/s. Equally, the relative submergence of Cameron et al.'s (2017) H050 is less than that applied here at 3.1 and has greater Reynolds number at 21000 compared to that applied here.

In the region $(z + z_0)/h' \geq 0.9$, the inverse velocity derivative declines, tending back towards the logarithmic profile, as shown in Fig. 6.4(a). The peakedness and decline of the simulated results may be influenced to some degree by the slip boundary condition set at the surface and would go some way to explain why the peak occurs at a lesser elevation for both simulations compared to the results of Cameron et al. (2017). If a free-surface approach had been applied using the Level-Set Method for example, it is possible that this region of the velocity profile would be more closely aligned to the results of Cameron et al. (2017) as any free-surface deformation could be fully taken into account.

Fig. 6.4(b) presents the Clauser plot of normalised velocity, $u^+ = \langle \bar{u} \rangle / u_*$ against normalised elevation, $z^+ = zu_*/v$ for LES-C and LES-F as well as other cases found in the literature. The viscous length scale is used for normalisation in this case even though the flow is above a rough surface, whereby the roughness length may be a more appropriate normalisation, to allow direct comparison with a smooth bed case and the wider literature which would otherwise be impossible. Like the results of Bomminayuni and Stoesser (2011) and Grass et al. (1971), Fig. 6.4(b) shows that the velocity profile of the LES-F case exhibits a transition from the virtual zero-plane to $z^+ \cong 50$ that follows a polynomial function. Fig. 6.4(b) also shows that the logarithmic regions of the velocity profiles for both LES-C and LES-F fit well with a variety of flows over different roughness surfaces and under different flow conditions explored both experimentally and numerically in the literature. The profiles also exhibit the expected trend of a downshift in the velocity profile from that of a smooth bed, as presented by Bomminayuni and Stoesser (2011). Fig. 6.4(b) also highlights that the velocity profile that was applied at initialisation, and thus also the mass within the system, was indeed appropriately apportioned and resulted in such representative velocity profiles.

The normalised double averaged Reynolds normal and shear stresses are presented in Fig's. 6.5(a) and (b), respectively against normalised elevation and show how well the stress characteristics of both the LES-C and LES-F cases fit with

the literature. As Fig. 6.5(a) shows, the normal stress in the spanwise and wall-normal directions fit particularly well with that of Cameron et al's. (2017) H050 case. However, there is some deviation in the streamwise direction compared to the experimental results. Not only do the results of the LES cases exhibit a higher peak normal stress, but that stress also decays non-linearly and at an increased rate compared to the H050 case. The difference in the normal stress in the streamwise direction could be due to the high porosity of the bed used in this study which may alter the pressure field within the channel flow giving rise to the reduction in normal stress observed in Fig. 6.5(a). The effect of bed porosity on channel flow is an area requiring much further study to be fully understood.

Fig. 6.5(b) shows that the shear stress approaches the linear trend exhibited by the results of Bomminayuni and Stoesser (2011), Cameron et al. (2017) and Grass et al. (1971). The flow can therefore be considered two-dimensional, as expected with the boundary conditions applied here, and the influence of secondary currents negligible.
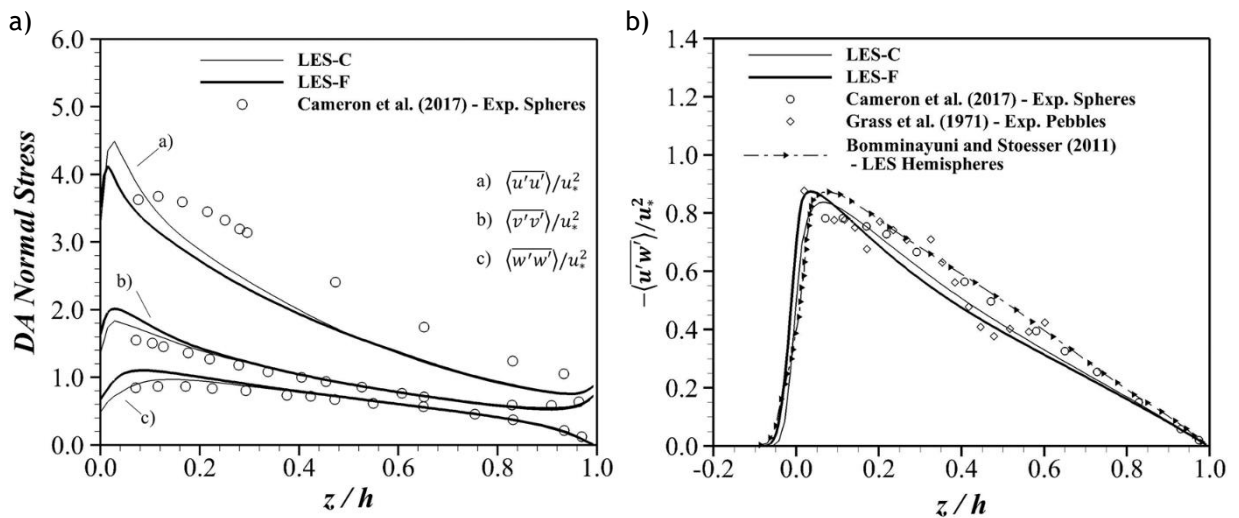
Figure 6.5. (a) Normalised DA Reynolds normal stresses against normalised elevation for LES-C and LES-F, as well as case H050 of Cameron et al. (2017); **(b)** Normalised DA Reynolds shear stress against normalised elevation for LES-C and LES-F, as well as the experimental H050 case of Cameron et al. (2017), the rough hemisphere LES case of Bomminayuni and Stoesser (2011), and the experimental pebble case of Grass et al. (1971).

The normalised double averaged streamwise and wall-normal turbulence intensities displayed in Fig's. 6.6(a) and 6.6(b), respectively further highlighting how well the velocity components of the LES case's fit with the results of the wider literature. Both Fig. 6.6(a) and 6.6(b) shows that the turbulence intensity for the

LES cases propagates into the bed but appears to decay in the near-bed region at a greater rate than that observed by Bomminayuni and Stoesser (2011) above a layer of hemispheres. The peak streamwise turbulence intensity shown in Fig. 6.6(a) appears highly comparable to the literature. However, the peak wall-normal turbulence intensity, shown in Fig. 6.6(b), is slightly reduced compared to the literature, but fits the overall trend very well. It appears then that the highly porous roughness geometry used in this study may result in some damping of the turbulent intensity components, particularly in the wall-normal direction, compared with an impermeable roughness surface.
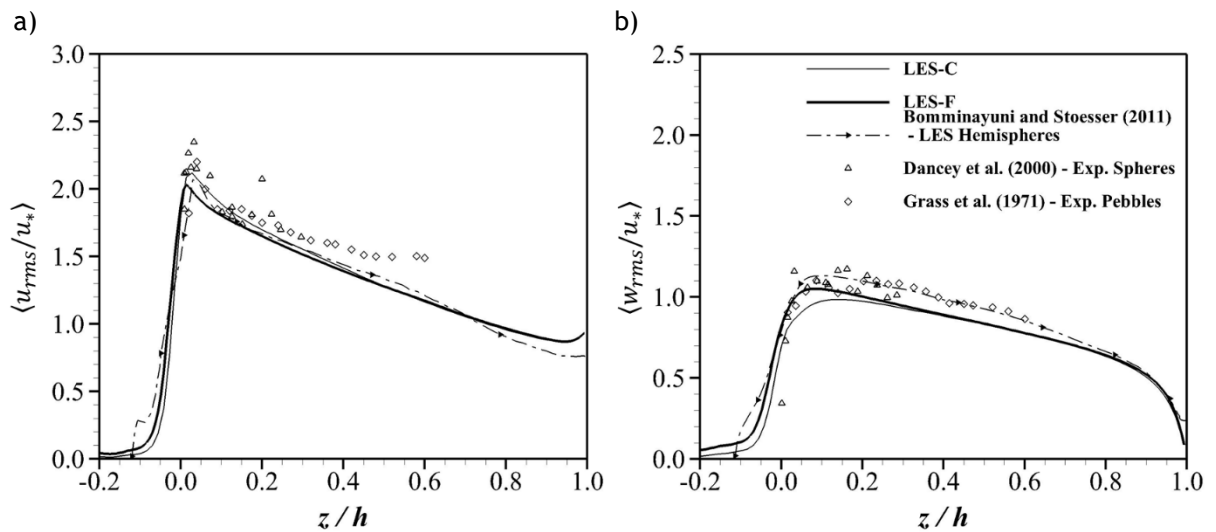
Figure 6.6. (a) Normalised DA streamwise turbulence intensity against normalised elevation for LES-C and LES-F, as well as the literature; **(b)** Normalised DA wall-normal turbulence intensity against normalised elevation for LES-C and LES-F, as well as the literature, also including the legend for both Fig's. 6.6(a) and 6.6(b).

As Cameron et al. (2017) remark, there is not a vast amount of skewness and kurtosis data available for open channel flows, let alone above porous roughness surfaces. However, Fig's. 6.7(a) and 6.7(b) do show good agreement with the data of Cameron et al's. (2017) H050 experimental case. The DA skewness shown in Fig. 6.7(a) agrees particularly well for both LES cases in all three component directions in the region $z/h \geq 0.1$.

The ratio between streamwise and wall-normal velocity skewness, S_u/S_w, for the LES-C case somewhat agrees with the data of Cameron et al. (2017). However, in the region $z/h \leq 0.2$, the LES-C S_u/S_w is increasingly negative, whereas Cameron et al's. (2017) is increasingly positive. However, this increasingly positive trend in the skewness ratio in the region $z/h \leq 0.2$ is observed in the LES-F results. The LES-

F skewness ratio also approaches a constant value of approx. -0.9 within the region $0.3 \leq z/h \leq 0.7$ before gradually tending towards the positive with increased elevation in a similar fashion to that of Cameron et al. (2017).
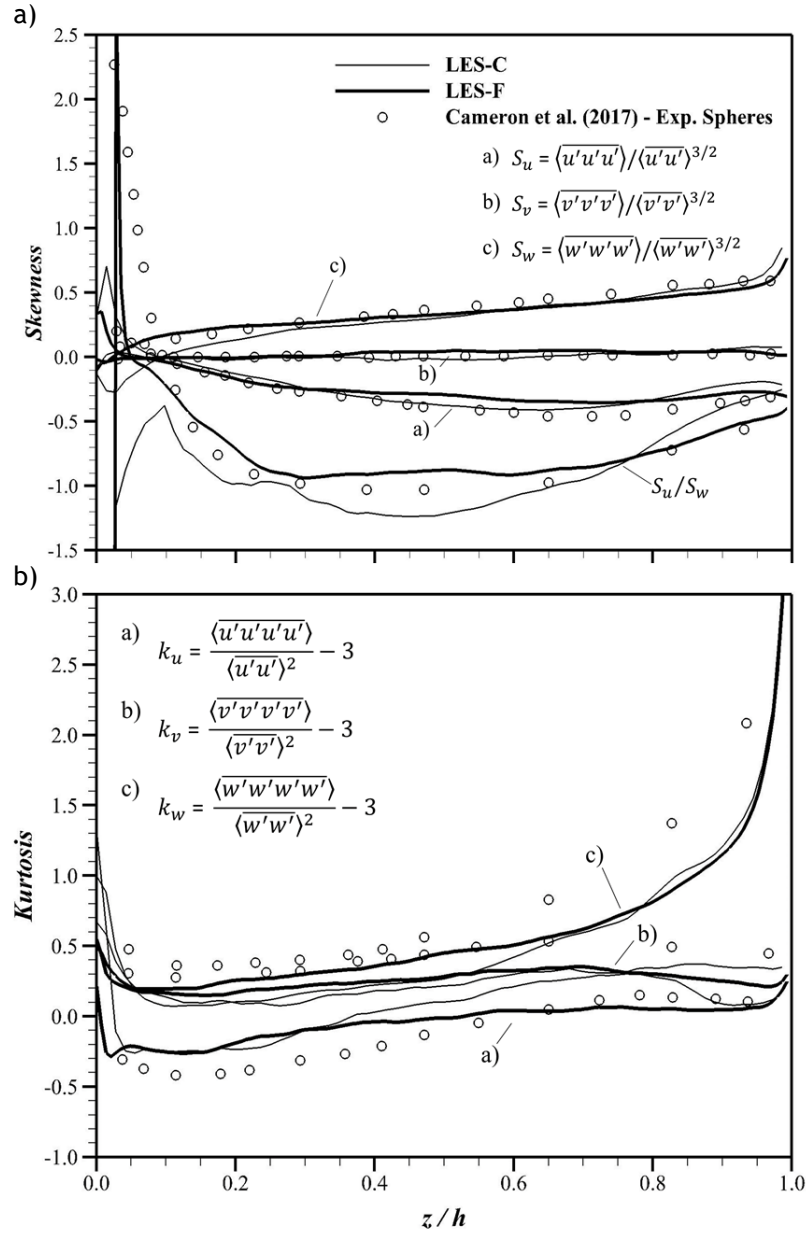
Figure 6.7. (a) DA Skewness for the three velocity components $u, v,$ and w in the x-, y-, and z-directions, respectively against normalised elevation for LES-C and LES-F, as well as case H050 of Cameron et al. (2017); **(b)** DA Kurtosis for $u, v,$ and w against normalised elevation for LES-C and LES-F, as well as case H050 of Cameron et al. (2017).

The kurtosis in each component direction, as shown in Fig. 6.7(b), for both LES cases deviates somewhat from Cameron et al's. (2017) data. However, there is

agreement in the general trends; kurtosis in the wall-normal direction is increasingly positive with an increase in elevation; kurtosis in the spanwise direction is near constant and small in magnitude but remains positive; kurtosis in the streamwise direction starts negative but tends towards positive with increasing elevation.

As Fig. 6.7(b) shows, the kurtosis for both LES cases in the streamwise and spanwise directions largely agree with each other. However, the wall-normal kurtosis for LES-C becomes positive after just $0.35h$ and continues to increase with increasing elevation. Whereas the wall-normal kurtosis for LES-F is much flatter, and though it becomes positive after $0.55h$, remains below 0.1 until beyond $0.95h$. Interestingly there appears to be some downshift in k_v of both the LES cases closer to zero compared to the experimental H050 case (Cameron et al. 2017).

Clearly, the simulated channel flows in both the LES cases investigated here are highly representative of that found above other permeable roughness elements found in the literature. Given that turbulent channel flow drives the pressure and energy flux across the bed interface, which in turn propagates into the bed and influences interstitial phenomena, it can be assumed that the bed flow must also be highly representative. Thus, allowing for further exploration of the relationship between channel and bed flows. The small statistical differences in the disparate resolution flow fields of the LES-C and LES-F cases also makes it clear that the chosen grid resolutions are sufficiently fine and further grid division is not required. For the remainder of this chapter and for further, more in-depth analysis of the flow field, only the fine grid LES-F results are utilised.

6.3.2. Taylor's Hypothesis

Under the assumption of Taylor's hypothesis (Taylor, 1938), convection velocities, which are the velocity at which turbulent eddies propagate downstream (del Alamo and Jimenez, 2009), can be considered as close to, and thus the same as, local mean velocities so long as the turbulence intensity is sufficiently small (Moin, 2009). This assumption has proved highly useful where spatial-temporal data is unavailable or very difficult to obtain. However, for high shear turbulent flows, such as those near a boundary, Taylor's hypothesis has been shown to not always be wholly applicable (Geng et al. 2015; Piomelli et al. 1989; Zaman and Hussain, 1981; Fisher and Davies, 1964; and Lin, 1953). This section investigates velocity fluctuations to further understand the characteristics of turbulent eddies above rough, porous bed geometry.
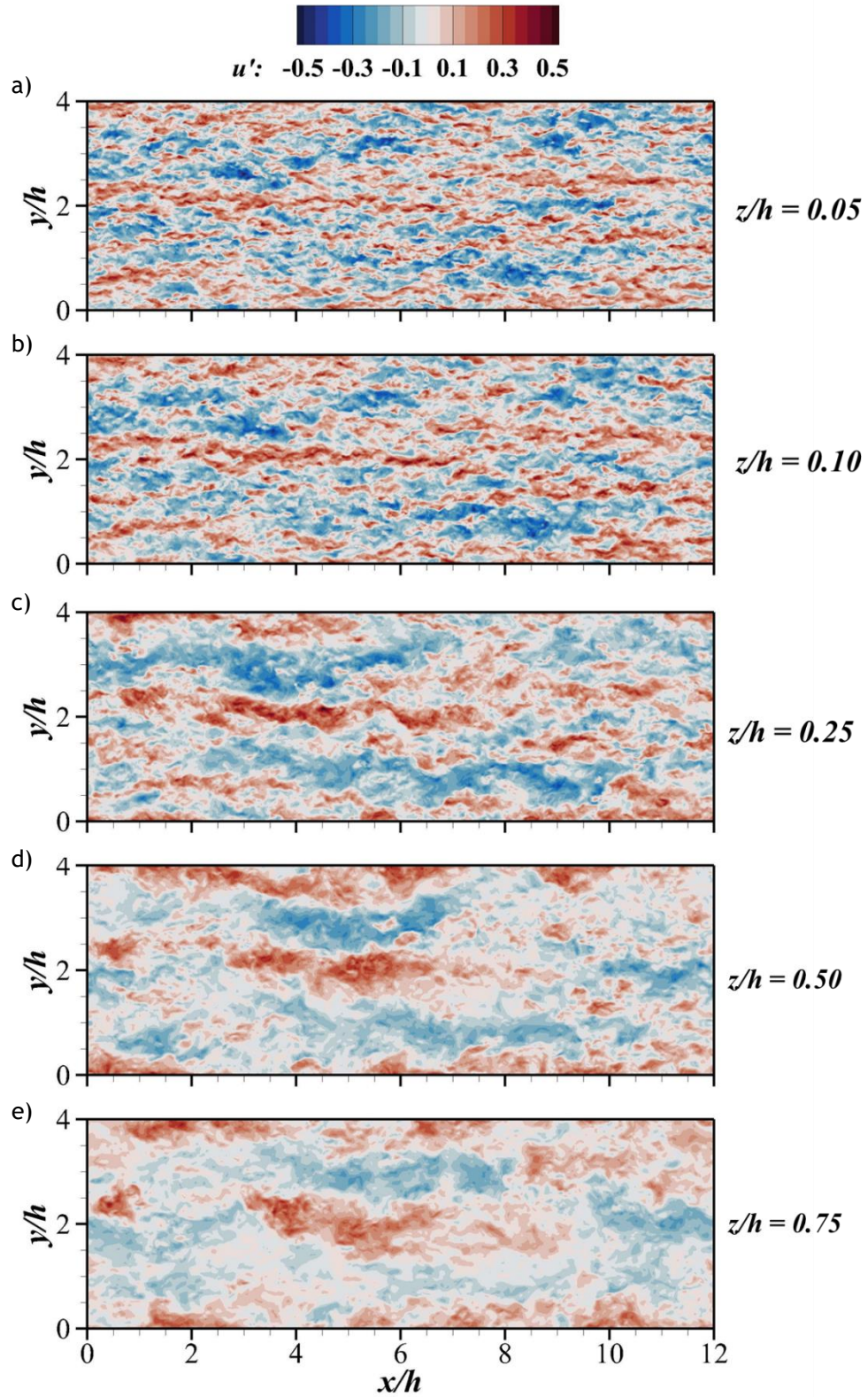
Figure 6.8. (a)-(e) LES-F distribution of instantaneous velocity fluctuations in the $x - y$ plane at various elevations at $140FT$.

The contours of instantaneous velocity fluctuations of LES-F in the $x - y$ plane at $140FT$ shown for various elevations in depth in Fig's. 6.8(a)-(e) highlight the high

and low turbulent streaks typically found above roughness surfaces (eg. Cameron et al. 2017). It is clear that very near the bed, as shown in Fig's. 6.8(a) and (b), numerous structures of differing wavelength exist about seemingly random locations. Fig. 6.8(c) shows that $6h$ appears be the largest wavelength for a turbulent eddy at this moment in time and assuming that such an eddy is representative of the largest wavelengths throughout the simulation, then a domain length of $12h$ should be sufficient to capture all scales of turbulent motion. However, as Cameron et al. (2017) point out, it is very difficult to reliably quantify the characteristics of such structures from plots like Fig's. 6.8(a)-(e) and that further quantitative analysis is required.

Spectral analysis is often used to quantifiably characterise and analyse turbulent eddies. Following Taylor's hypothesis, local mean velocities are employed as convective velocities in the spectral calculations even though Taylor's hypothesis is not always applicable, as previously discussed. Therefore, this study conducts spectral analysis of the LES-F flow field using convective velocities (U_{cu_i}) for the velocity component fluctuations defined as (Geng et al. 2015):

$$U_{cu_i} = \frac{\overline{(-\partial u_i' / \partial t)(\partial u_i' / \partial x)}}{\overline{(\partial u_i' / \partial x)^2}}$$ (6.4)

where, $\frac{\partial u_i'}{\partial t}$ is the temporal velocity derivative, $\frac{\partial u_i'}{\partial x}$ is the spatial velocity derivative, in which u_i' is the instantaneous velocity fluctuation and the i, j, and k notation is used interchangeably with u', v', and w' to denote velocity components in the x-, y-, z-directions, respectively.

Fig. 6.9 shows the DA convection velocities for the three velocity component fluctuations for LES-F alongside the DA velocity profile previously presented in Fig. 6.4(a). DA convective velocities were obtained by first calculating U_{cu_i} using Eq. 6.4 at each probe location, as laid out in Tables 6.4 and 6.5, at each fluid cell in the z-direction above the roughness surface. The U_{cu_i} values were then time averaged across the 6 sections with probes with corresponding y-direction coordinates, as shown in Table 6.5. The resulting time-averaged U_{cu_i} values for each group of 6 probes were then averaged in space across the domain.

Interestingly, Fig. 6.9 highlights that throughout the depth of the channel in LES-F, eddies propagate in the streamwise direction slower than the mean velocity. This is contrary to the observations of Kim and Hussain (1993) and Geng et al. (2015) who found that for smooth bed turbulent flows convective velocities tend towards

the mean when $z+\geq 20$, and that below this level in the viscous sublayer, convective velocities are higher than the mean. Similar observations were also made by del Alamo and Jimenez (2009) who showed that convection velocities across several different flow conditions tend towards the mean flow velocity. However, del Alamo and Jimenez (2009) also show the effect small and large wavelength eddies have on the convective velocities about the mean flow velocity and that without the contribution of large wavelength eddies, the convective velocities remain below, almost parallel to, the local mean velocity. This phenomenon appears to also be shown in Fig. 6.9. However, the difference between the local mean velocity and convective velocity is far higher (approx. 6 times higher) in this study than shown by del Alamo and Jimenez (2009). This could be due to the apparent lack of large wavelength eddies because of the chosen extent of the domain whereby large-scale eddies simply cannot be captured as their wavelength far exceeds the streamwise length of the computational domain.
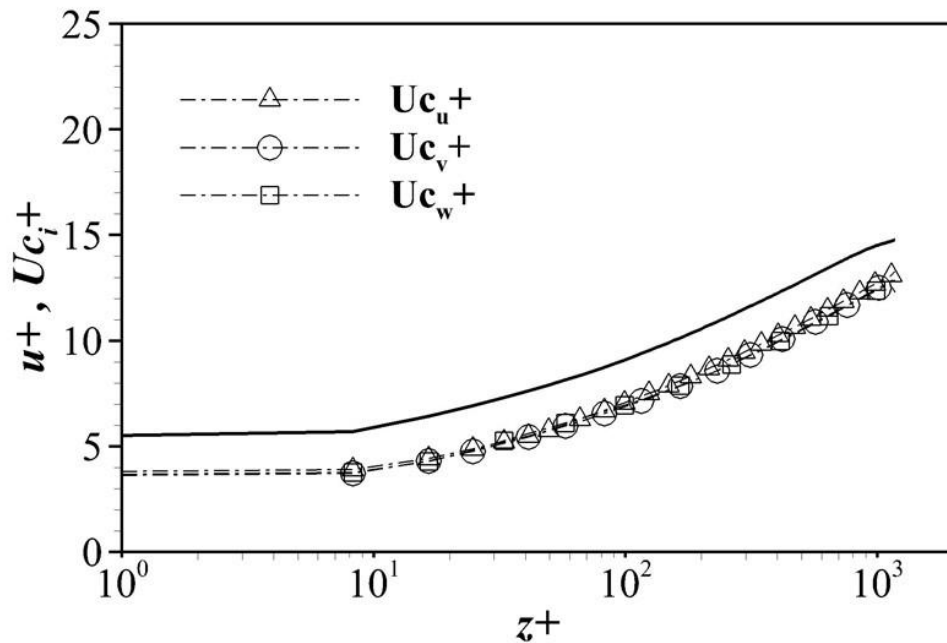
Figure 6.9. Normalised DA convection velocities, U_{cu_i} for the three velocity component fluctuations u', v', and w' in the x-, y-, and z-directions, respectively, and normalised DA streamwise velocity profile ($u^+ = \langle \bar{u} \rangle / u_*$) against normalised elevation ($z^+ = zu_*/v$) for LES-F.

The cross-correlation coefficient ($R_{\partial u_i}$) between the spatial and temporal derivatives of the velocity fluctuations is given by (Geng et al. 2015):

$$R_{\partial u_i} = \frac{\overline{(-\partial u_i' / \partial t)(\partial u_i' / \partial x)}}{\left[\overline{(\partial u_i' / \partial t)^2}\right]^{\frac{1}{2}} \left[\overline{(\partial u_i' / \partial x)^2}\right]^{\frac{1}{2}}} \tag{6.5}$$

$R_{\partial u_i}$ is a useful indicator for the rate of decay of turbulent eddies whereby it equals unity for a perfectly frozen wave and zero for eddies that have fully decayed, or dissipated, over the wavelength. Thus, under Taylor's hypothesis, $R_{\partial u_i}$ would equal unity outside of the viscous sublayer.

Fig. 6.10 shows that for the LES-F case, $R_{\partial u_i}$ for all three velocity fluctuation components is significantly below unity and though tending towards it, $R_{\partial u}$ peaks at 0.91, $R_{\partial v}$ peaks at 0.87, and $R_{\partial w}$ peaks at 0.86. Such a result is significantly different to that found for turbulent channel flows above smooth beds by Geng et al. (2015) and Piomelli et al. (1989) where the three correlation coefficient components are 0.89 at their lowest and above 0.97 when $z+ \geq 50$.
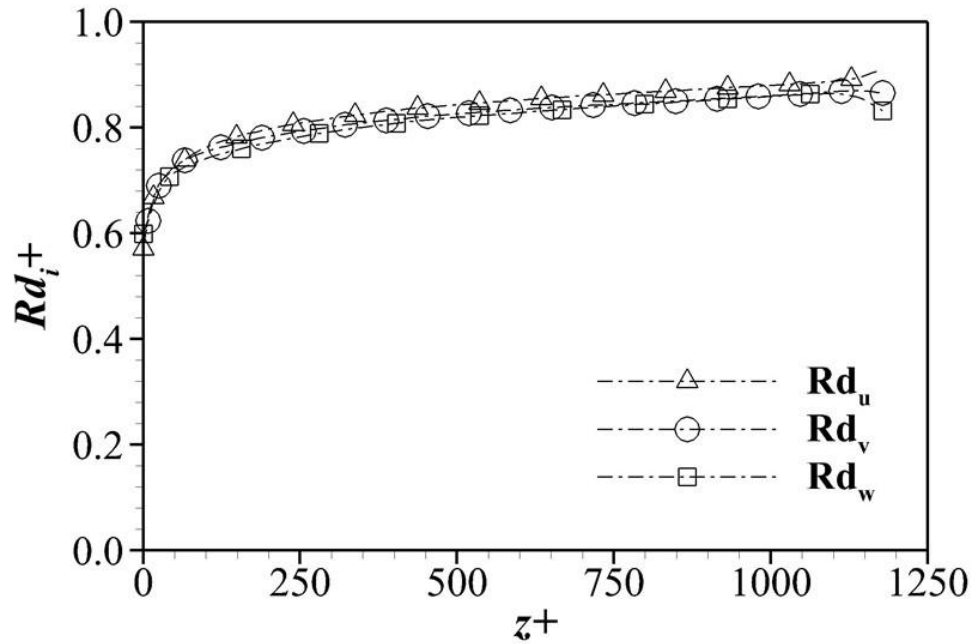
Figure 6.10. Corelation coefficients, $R_{\partial u_i}$ for the three velocity component fluctuations u', v', and w' in the x-, y-, and z-directions, against normalised elevation ($z^+ = z u_* / v$) for LES-F.

However, it is worth remembering that LES only fully resolves the large wavelength eddies with the small wavelengths being handled by a subgrid-scale (SGS) model, as explained in Section 3.1. Therefore, as Piomelli et al. (1989) concluded, the effects of the small wavelength eddies, which highly affect velocity derivates, might not be fully appreciated in the LES results shown here. However,

the SGS cutoff wavenumber should be sufficiently small given the high resolution of the LES-F case that the effects of the SGS model on the statistics shown here are at the very least minimalised.

The variance of the velocity fluctuation spatial derivative against the variance of the velocity fluctuation temporal derivative is shown in Fig's. 6.11(a-l) for probes 135, 150, and 24 for $z/h = 0.021$, 0.181, 0.5, and 0.736. The slope of the solid linear least-square fit lines on Fig's. 6.11(a-l) is equal to $1/U_{cu_i}$ at that elevation for that particular probe.
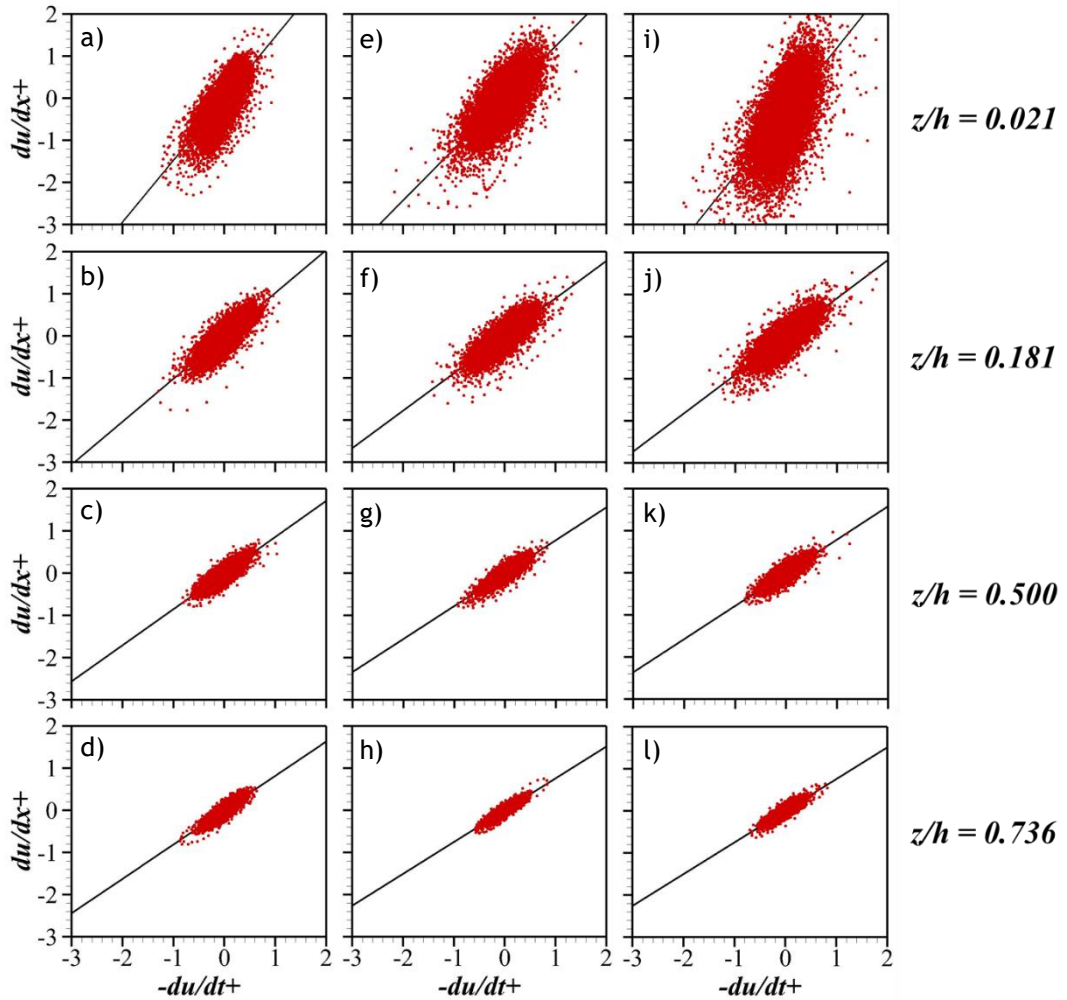
Figure 6.11. (a-l) The variance of the velocity fluctuation spatial derivative against the variance of the velocity fluctuation temporal derivative for probes 135 (a-d), 150 (e-h), and 24 (i-l) of the LES-F case at $z/h = 0.021$, 0.181, 0.5, and 0.736. The spatial and temporal derivatives are normalised by v/u_*^3. The slope of the solid linear least-square fit lines for all panels is equal to $1/U_{cu_i}$.

The variance in the spatial and temporal velocity fluctuation derivatives recorded by probe 135 at $z/h = 0.021$, as shown in Fig. 6.11(a), are above a pore

space within the surface of the riverbed geometry. Whereas the derivatives recorded by probe's 150 and 24 at $z/h = 0.021$, as shown in Fig's. 6.11(e) and (i) respectively, are 6 and 3 fluid cells, respectively above bed particle crests.

As expected, the greatest variance in the spatial and temporal derivatives is closest to the bed in general, but greater still in proximity to a bed particle crest as opposed to a pore, as shown in Fig's. 6.11(a), (e), and (i). With increased elevation, the variance in the spatial and temporal derivatives shown in Fig's. 6.11(a-l) quickly reduces and becomes highly similar. Even at $z/h = 0.181$, the variance in the derivatives is highly similar between the three probes, as shown by Fig's. 6.11 (b), (f), and (j). As the water surface is approached at $z/h = 0.736$, the variance in the derivatives across the three probes is almost identical, though with slightly different scatter arrangements about the upper and lower limits. Therefore, suggesting that localised geometric changes, ie. pore vs. crest, only directly affect the downstream propagation of eddies within the immediate vicinity of the change and within the region $z/h \leq 0.2$. This means that within the region $z/h \leq 0.2$, the spatial variance of the convection velocities is largely determined by the geometric characteristics of the roughness surface.

The convective velocities obtained using Eq. 6.4 were used to perform Welch's power spectral density analysis of the velocity fluctuation time series of specific probe groups of LES-F to generate the pre-multiplied normalised wavenumber spectra contours shown in Fig's. 6.12 (a-c), the wavenumber energy frequency spectra profiles at different elevations shown in Fig's. 6.13 (a-e), and the pre-multiplied normalised wavenumber spectra profiles at different elevations shown in Fig's. 6.13 (f-j). The three probe groups (PGs) (8, 21, and 35) used for Fig's. 6.12 and 6.13 are made up of 6 similar probes with the same y-direction coordinates but spaced $2h$ apart in the x-direction, giving 1 probe in each section of the domain, as shown in Table 6.5. The velocity fluctuation time series for each probe group is simply the velocity fluctuations at each timestep for each fluid cell in the z-direction of each individual probe concatenated together to provide a 'probe group' time series six times longer than that for a single probe that could be used for the spectral analysis.
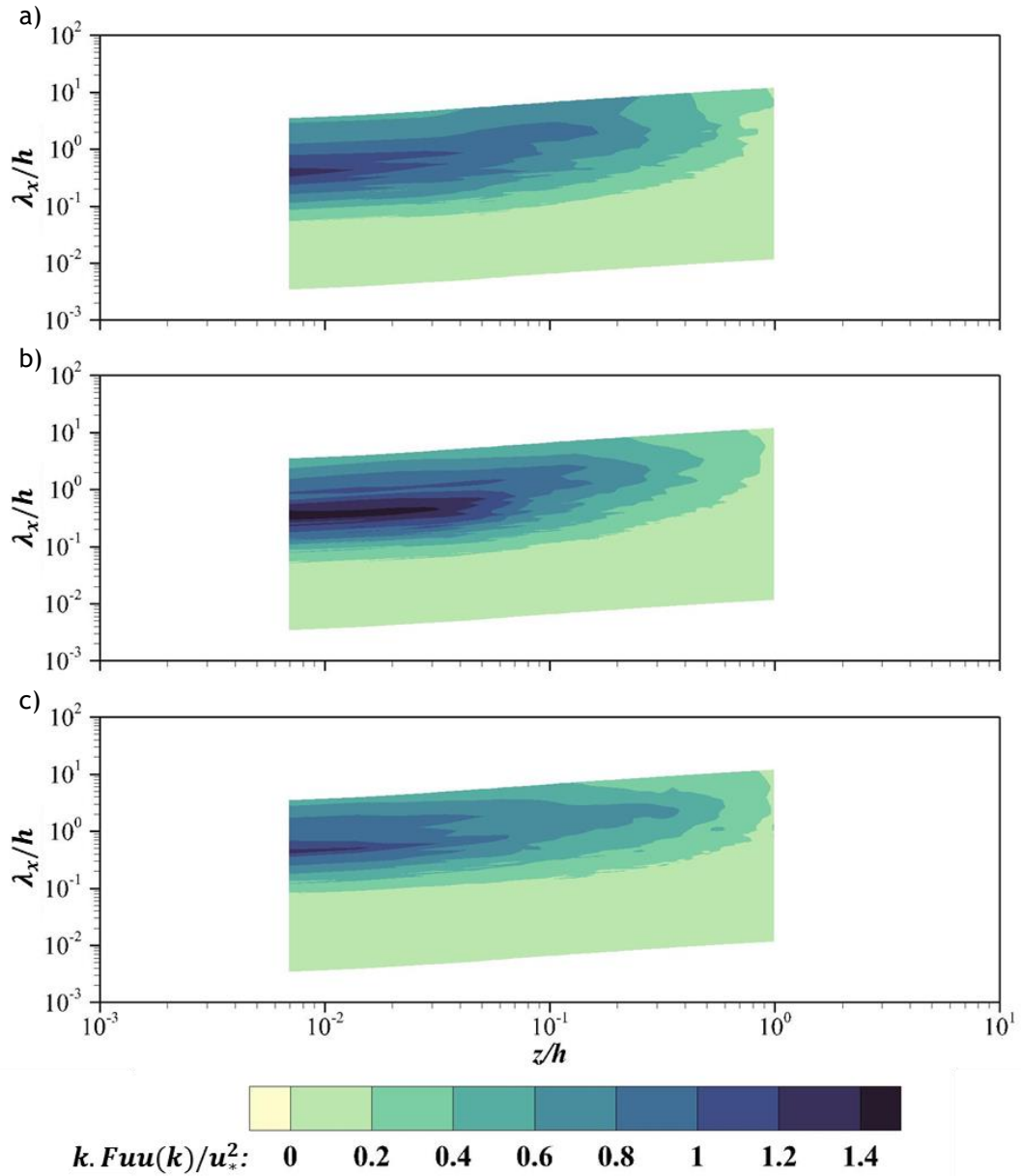
Figure 6.12. Pre-multiplied normalised wavenumber spectra contours of the velocity fluctuation time series of PGs **(a)** 8, **(b)** 21, and **(c)** 35 of LES-F. The legend is the same for all panels.

The pre-multiplied normalised wavenumber spectra contours displayed in Fig's. 6.12(a-c) show that in the LES-F case some turbulent eddies with relatively high energy exist within the region between the bed surface and approximately $z/h = 0.4$. In comparison to the experimental cases undertaken by Cameron et al. (2017), similar energetic eddies were only found to propagate up from the bed surface to approximately $z/h = 0.2$, but have wavelengths in the order of one magnitude greater. However, Cameron et al. (2017) did provide evidence of very large-scale motions, as opposed to only large-scale motions, through secondary peaks seen in

their similarly constructed spectra contours. Any secondary observed peaks in Fig's. 6.12(a-c) are more likely in this study to be due to the convergence scheme of the simulation rather than evidence of very large-scale motions. As already alluded to, the length of the domain used in this study would likely need to be several times longer to fully encapsulate and quantify the emergence of very large-scale motions. Further research on such phenomena above porous, rough beds using LES and DNS alike, as well as experimentation is needed. Fig's. 6.12(a-c) also show that high energy eddies are confined to the region $z/h < 0.06$, and far less in the cases of probe groups 8 and 35. PG 21 was chosen to display here due to the probes encompassing a large pore space extending down from the bed surface by $0.3h.$ As Fig. 6.12(b) shows, such a large and deep pore results in very high energy, yet relatively small wavelength $(\sim 0.03h)$, eddies propagating from the bed surface.

As shown in Fig's. 6.13(c-e), the wavenumber energy frequency spectra of each probe group in the region $z/h \geq 0.25$ collapse onto one another indicating that the contribution of the various wavelengths to the turbulent kinetic energy (TKE) is spatially invariant in the upper 75% of the channel depth. However, Fig's. 6.13(a) and (b) show that near the bed there are some small differences in the wavenumber energy frequency profiles indicating the relative contribution of various wavelengths to TKE in the region $z/h < 0.25$ does vary spatially to some degree.

The Kolmogorov -5/3 power law for the distribution of turbulent eddies of various wavelengths that cascade from production to dissipation is shown in Fig's. 6.13(a-e) by the dashed linear line. Though the Reynolds number is relatively low in this study at 15,000, as shown by Moser et al. (1999) and Han et al. (2017) the emergence of the inertial subrange can occur at even lower Reynolds numbers over smooth surfaces as well as similar Reynolds numbers over rough, porous surfaces, respectively. Fig's. 6.13(a-e) all show that for any elevation discrete spectral peaks do not exist for frequencies less than 2 Hz highlighting the extent of the production range and large-scale motions. Beyond the production range, in the region $f > 2$, pure turbulence propagates. At the elevation $z/h = 0.05$, Fig. 6.13(a) shows that only a small inertial subrange exists in the approximate region $2 > f > 10$ before the wavenumber energy frequency profiles depart from the Kolmogorov scale and the energy is dissipated by the SGS model. Fig's. 6.13(b-e) show that the inertial subrange exists in the approximate regions $2 > f > 25$, $2 > f > 30$, $2 > f > 30$, and $2 > f > 20$ at the elevations $z/h = 0.10, 0.25, 0.50,$ and 0.75, respectively.
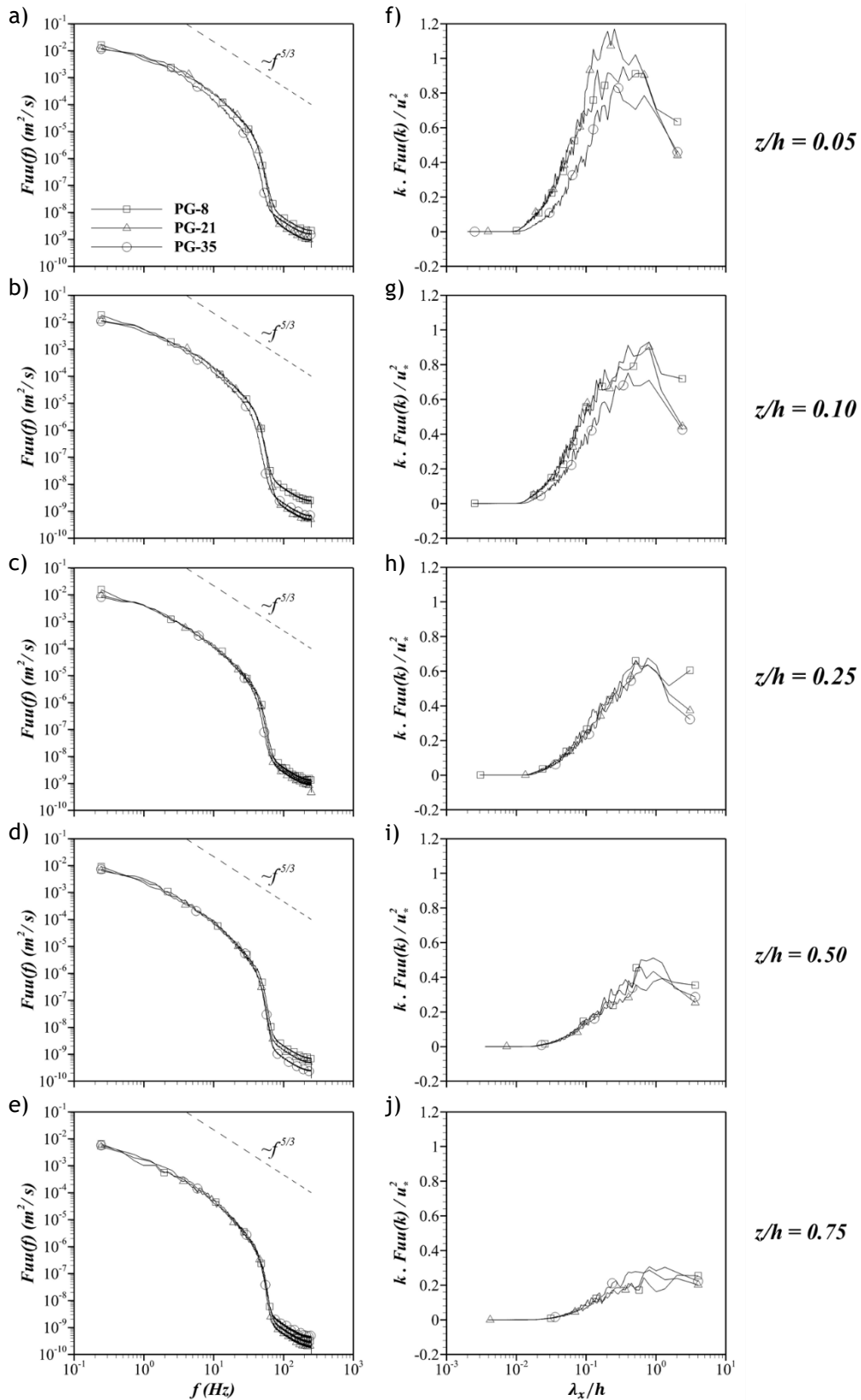
Figure 6.13. (a)-(e) wavenumber energy frequency spectra; and **(f)-(j)** normalised one-dimensional pre-multiplied streamwise wavenumber spectrum, for select spatially averaged PGs of LES-F at various elevations. The legend shown in Fig.

6.13(a) is the same for all panels of Fig. 6.13. The Kolmogorov -5/3 power law is displayed as a dashed line in Fig's 6.13(a)-(e).

The pre-multiplied normalised wavenumber spectra, shown in Fig's. 6.13(f-j) make evident that near the roughness surface, in the lower layers of the channel flow, larger wavelengths make a greater contribution to the TKE than in the upper layers of the flow. The pre-multiplied normalised wavenumber spectra shown in Fig's. 6.13(f-j), highlight the changing distribution and magnitude of energy with increased elevation. Fig's 6.13(h-j) also show that the distribution and magnitude of energy throughout the upper layers of the channel flow is not spatially variant given the spectra of each probe group collapse onto one another. However, Fig's. 6.13(f) and (g) show that the distribution and magnitude of energy in the lower layers of the flow depth, close to the roughness surface, is highly spatially variant with a wide range in the spectra profiles of the three PG's. Of note is that the wavelengths shown in Fig's. 6.13(f-j) are of lesser magnitude than that typically found in the literature (eg: Cameron et al. 2017). This suggests that the simulations performed here might only be capturing the smaller scales of turbulent motion. Thus, the computational domain of any future study would need to be several times larger than that applied here, particularly in the streamwise direction, to fully appreciate all scales of turbulent motion.

6.3.3. Mean Velocity Turbulent Kinetic Energy

Turbulent Kinetic Energy (TKE), k, of the time-averaged flow field can be described as (Mignot et al. 2008):

$$\bar{k} = \frac{1}{2}\left(\overline{u'^2} + \overline{v'^2} + \overline{w'^2}\right) \tag{6.6}$$

where, u', v', and w' are the streamwise, spanwise and wall-normal velocity fluctuations, respectively, expressed by $u'_i = u_i - \bar{u}_i$, in which, u_i is the instantaneous velocity and the i, j, and k notation is used interchangeably with u, v, and w to denote velocity components in the x-, y-, z-directions.

Fig. 6.14(a) presents contours of normalised time averaged TKE for LES-F in an $x - z$ plane at the centreline of the domain, across the full depth of the domain, for the first two sections of the domain ($x/h \leq 4$) in the streamwise direction. Since the domain is formed of six similar sections, any phenomena observed in the two sections shown in Fig. 6.14(a) are also seen in the other four sections not shown

here for brevity. Fig. 6.14(b) plots the vertical distribution of normalised DA TKE. Fig's. 6.14(c) and 6.14(d) present contours of normalised time averaged TKE in an $x - z$ plane at the centreline of the domain and a $y - z$ plane at $x/h = 1.5$, respectively, highlighting the near-bed region, in sections $1.6 \leq x/h \leq 2.6$ and $2.0 \leq y/h \leq 3.0$, respectively with streamwise normal stress vectors also displayed.
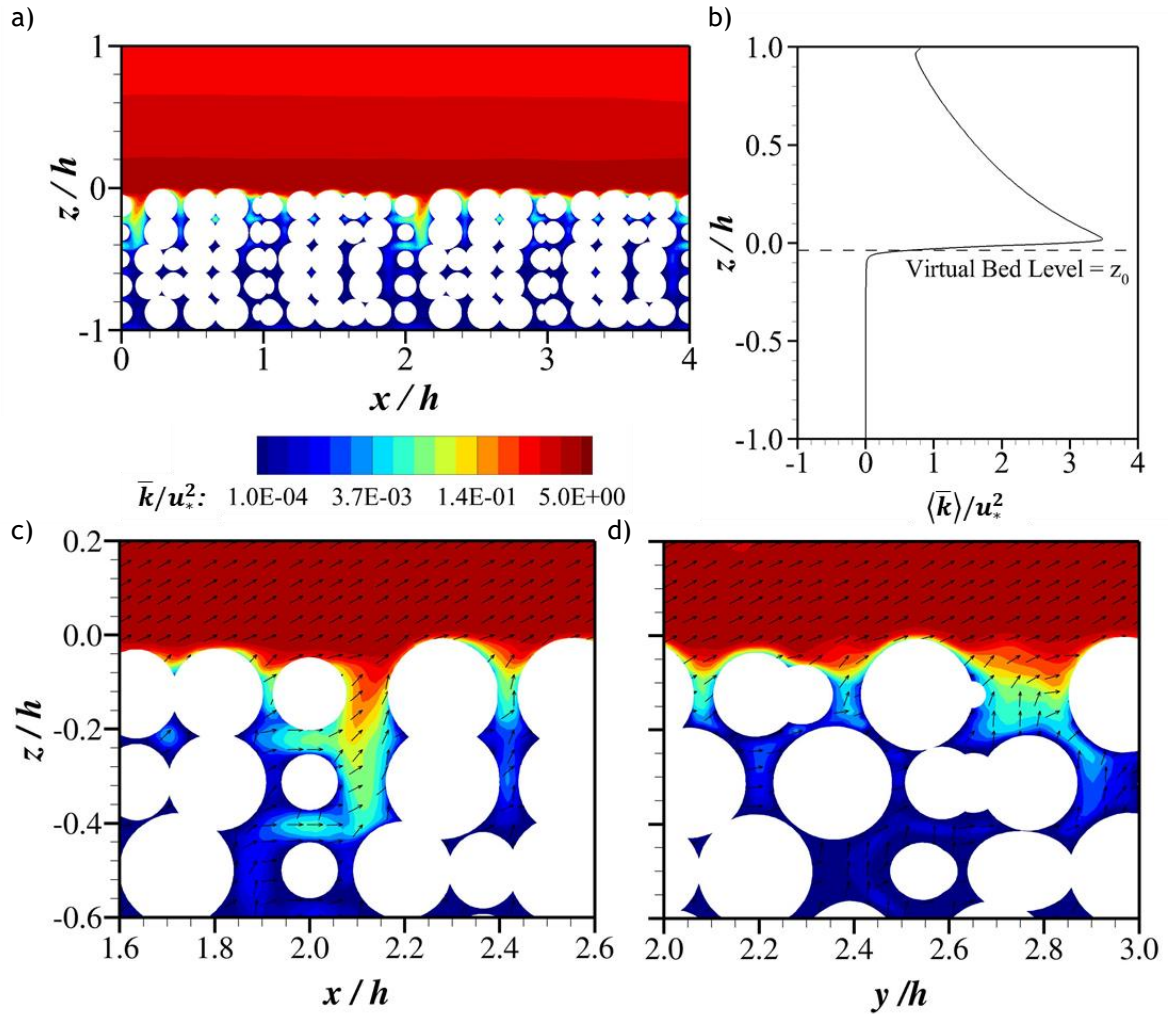
Figure 6.14. (a) contours of normalised time averaged TKE in a centreline $x - z$ plane, across the full depth of the domain for LES-F; **(b)** vertical distribution of normalised DA TKE for LES-F; **(c)** contours of normalised time averaged TKE in a centreline $x - z$ plane, highlighting only the near-bed region, at a select section of the domain with streamwise normal stress vectors also displayed for LES-F; and **(d)** contours of normalised time averaged TKE in a $y - z$ plane at $x/h = 1.5$, highlighting only the near-bed region, at a select section of the domain with streamwise normal stress vectors also displayed for LES-F. The legend for Fig's. 6.9(a), 6.9(c), and 6.9(d) are the same as displayed below Fig. 6.9(a).

The contours of Fig's. 6.14(a), 6.14(c), and 6.14(d) highlight the lack of local maxima that might be expected from a highly rough surface (McSherry et al. 2017), and instead show the uniformity of the contours in the near-bed region. In particular, the invariance in the change in elevation over which TKE peaks and then rapidly declines above any give bed particle.

The depth above the bed surface in which the TKE distribution was affected by the bed topography was found above a spatially heterogenous fractal roughness surface to be $0.2h$ by McSherry et al. (2017). However, the uniformity of the contours in the near bed region shows that the influence of the bed topography on the TKE distribution in this study with a relatively invariant bed topography was confined to within just $0.05h$. Thus, the influence of the spatial variance of the roughness surface topography on the TKE distribution appears to not only be confined to the near bed region but also determines the elevation over which the TKE distribution is affected.

It remains unclear from these results whether porosity also has some influence on the TKE distribution above the surface roughness crests. However, it does appear from Fig's. 6.14(c) and 6.14(d) that pores in the surface layer of the bed particles (e.g: at $x/h \approx 2.1$) have a large effect on the TKE distribution below the surface roughness. Large pores in the surface topography, as shown in Fig. 6.14(c), allow the propagation of TKE deep within the bed, even up to 3 particle layers deep.

The vertical distribution of normalised DA TKE presented in Fig. 6.14(b) shows that TKE is negligible in the region $z/h < -0.1$, peaks at 3.5 at $z/h \approx 0.03$, and declines to 0.8 at the water surface.

The normalised DA streamwise TKE flux, F_{ku} and the normalised DA wall normal TKE flux, F_{kw} can be described as (Han et al. 2017):

$$F_{ku} = \left\langle \frac{1}{2}\left(\overline{u'^3} + \overline{u'v'^2} + \overline{u'w'^2}\right) \right\rangle / u_*^3 \qquad (6.7)$$

$$F_{kw} = \left\langle \frac{1}{2}\left(\overline{u'^2w'} + \overline{v'^2w'} + \overline{w'^3}\right) \right\rangle / u_*^3 \qquad (6.8)$$

As Fig's. 6.15(a) and 6.15(b) show for LES-F, the normalised DA streamwise and wall normal TKE fluxes are negligible in the region $z/h < -0.08$. The positive peak F_{ku} of 2.0 occurs at $z/h \approx z_0$, as shown in Fig. 6.15(a). From its positive peak, F_{ku} rapidly declines to a minimum peak of -0.6 at $z/h \approx 0.24$ before increasing gradually towards 0.0, yet remaining negative, with increasing z/h. The negative F_{ku} in the upper layers of the flow, shown in Fig. 6.15(a), indicates that the TKE flux transports

in the streamwise direction slower than $\langle \bar{u} \rangle$ (Han et al. 2017). Whereas, in the near-bed region of the flow (ie: $-0.08 < z/h < 0.04$) where F_{ku} is strongly positive, the TKE flux transports in the streamwise direction faster than $\langle \bar{u} \rangle$ (Han et al. 2017).

As highlighted by Fig. 6.15(b), the negative peak F_{kw} of -0.58 occurs at $z/h \approx z_0$. From its negative peak, F_{kw} rapidly increases to a maximum of 0.38 at $z/h \approx 0.22$ before decreasing at a steady rate towards 0.0, yet remaining positive, with increasing z/h. The positive F_{kw} in the upper layers of the flow, shown in Fig. 6.15(b), indicates that the TKE flux transports in the wall-normal direction faster than $\langle \bar{w} \rangle$ (Han et al .2017). Whereas, in the near-bed region of the flow (ie: $-0.08 < z/h < 0.04$) where F_{kw} is strongly negative, the TKE flux transports in the wall-normal direction slower than $\langle \bar{w} \rangle$ (Han et al. 2017).
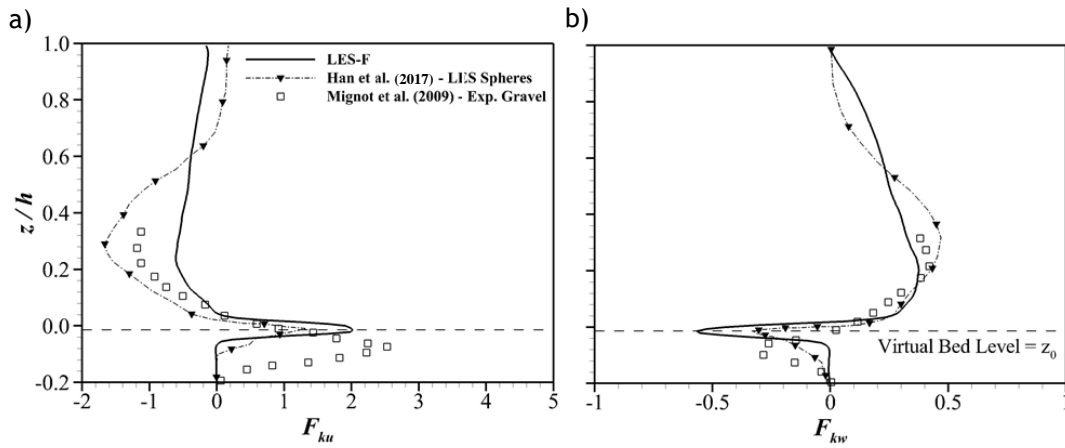
Figure 6.15. Normalised vertical elevation against normalised DA **(a)** streamwise; and **(b)** wall normal, TKE flux for LES-F.

The overall trends of the LES-F TKE flux results are very similar to that of Mignot et al. (2009) and Han et al. (2017) with peak flux occurring below the roughness crests and tending from positive to negative and vice-versa. However, it should be noted that the study undertaken by Mignot et al. (2009) featured macro roughness elements that provided an undulating bed surface. Thus, explaining why the peak TKE fluxes in their study seemingly occur so much further below the roughness crest compared to the results of either this study or that by Han et al. (2017). Fig's. 6.15(a) and (b) also show that in comparison with the results of Han et al. (2017), the TKE fluxes for LES-F have greater magnitude in the near-bed region and lesser in the upper flow depth. This reapportion of TKE flux is potentially due to the bed composition whereby the cubically packed spheres employed by Han et al. (2017)

would have likely resulted in smaller pores and overall lesser porosity compared with the relatively high porosity riverbed geometry employed in this study.

6.3.4. Turbulent Kinetic Energy Budget

The TKE of the time-averaged flow field, expressed by Eq. 6.6, can be decomposed into several different components to give a fuller description of the so-called TKE budget. Using the derivation by Mignot et al. (2008) for the TKE budget of open channel flows over rough beds, following the derivation of Raupach and Shaw (1982) for flows over vegetation canopies, the DA TKE budget in the streamwise direction, excluding any fluid cells containing IB markers, can be described by:

$$\underbrace{-\langle\overline{u'w'}\rangle\frac{\partial\langle\bar{u}\rangle}{\partial z}}_{P_s} \underbrace{-\langle\overline{u'w'}\rangle\langle\frac{\partial\tilde{u}}{\partial z}\rangle}_{P_m} \underbrace{-\langle\widetilde{\overline{u'w'}}\frac{\partial\tilde{u}}{\partial z}\rangle}_{P_w} \underbrace{-\frac{\partial\langle\overline{k'w'}\rangle}{\partial z}}_{T_D} \underbrace{-\frac{\partial\langle\tilde{k}\tilde{w}\rangle}{\partial z}}_{T_w} \underbrace{-\frac{\partial\langle\overline{P'w'}\rangle}{\partial z}}_{T_p} \underbrace{+v\frac{\partial^2\langle k\rangle}{\partial z^2}}_{T_v} - \in = 0$$

(6.9)

where, P_s is the shear production, P_m is the work of the bed induced velocity fluctuation against DA shear stress, P_w is wake production, T_D is vertical diffusion transport, T_w is form-induced diffusion transport, T_p is pressure transport in which, P is pressure, T_v is viscous transport, $\in$ is viscous dissipation which is approximated here by the residual of the sum of all the budget other terms, and $\tilde{}$ denotes the form-induced velocity component given by $\tilde{u}_i = \bar{u}_i - \langle\bar{u}_i\rangle$.

It should be noted that the normally quoted turbulent transport component, T_t has been further decomposed here and is provided through the sum of the T_D and T_w components of the TKE budget.

Expressions analogous to Eq. (6.9) can also be used to define the DA TKE budget in the spanwise and wall-normal directions.

Fig's. 6.16(a), (b), and (c) present the vertical distribution of the normalised DA streamwise, spanwise, and wall-normal TKE budgets for LES-F, respectively. The TKE budgets in the spanwise and wall-normal direction are shown here for completeness rather than to offer extensive analytical insight. The overall trends of the streamwise TKE budget, shown in Fig. 6.16(a), are very similar to that found in the literature (Yuan and Piomelli 2014, Mignot et al. 2009, and McSherry et al. 2017) with shear production and viscous dissipation being the dominant terms and peak viscous dissipation occurring just below the roughness crests. However, the peak shear production occurs just above, rather than below, the roughness crests

at $z+ = 10$ which is markedly different to that observed in the literature. In fact, the peak viscous dissipation, though occurring just below the roughness crests at $z+ = -10$, might be expected to occur deeper into the top layer of the bed. The transport terms for the streamwise TKE budget described in Fig. 6.16(a) are as expected in that they are negligible above the roughness sub-layer. Equally, the viscous transport and the work of the bed induced velocity fluctuation against DA shear stress terms show negligible influence throughout the depth in line with the assumptions that allow them to be customarily omitted. Interestingly, the form-induced diffusion transport is also negligible throughout the depth, and it appears that the normally stated turbulent transport term ($T_t = T_D + T_w$) is wholly dominated by vertical diffusion transport. Surprisingly, the wake production term appears to have little, if any, influence on the TKE budget in the LES-F case even though its peak magnitude is generally found to be somewhere between 5% (Yuan and Piomelli 2014) and 15% (McSherry et al. 2017) of the peak shear production. However, if the time averaged velocity tends towards the double averaged velocity, then the resulting wake production, which is calculated based upon the form-induced velocity components, would be very low, such as that observed in Fig. 6.16(a).

The spanwise TKE budget presented in Fig. 6.16(b) shows that vertical diffusion transport and viscous dissipation terms dominate, but to a much lesser degree (> 3 times less) than how the shear production and viscous dissipation terms dominate in the streamwise direction. Also, due to the relative magnitude of T_D to T_p, the pressure transport has a far greater overall influence in the spanwise direction than in the streamwise direction where it was greatly surpassed in magnitude by the P_s and T_D terms many times over.

The wall normal TKE budget presented in Fig. 6.16(c) is shown for completeness. However, Fig. 6.16(c) does highlight the significance of the pressure transport in the wall-normal direction due to the relative magnitude of T_p to the dominant P_s.

Spanwise and wall-normal TKE budget data are scarce in the literature due to most studies, including this one, being assumed two-dimensional and thus, the spanwise and wall-normal component contributions to the overall TKE of the flow field assumed negligible. As shown in Fig. 6.16(b), this may well be the case in the upper layers of the channel flow, but in the near-bed region ($z+ \leq 60$), the spanwise and wall-normal contributions to TKE, though admittedly small, are far from negligible and should still be taken into consideration. This may be especially true

in the presence of highly spatially variant porous roughness surfaces where the wake production would also play a significant role.
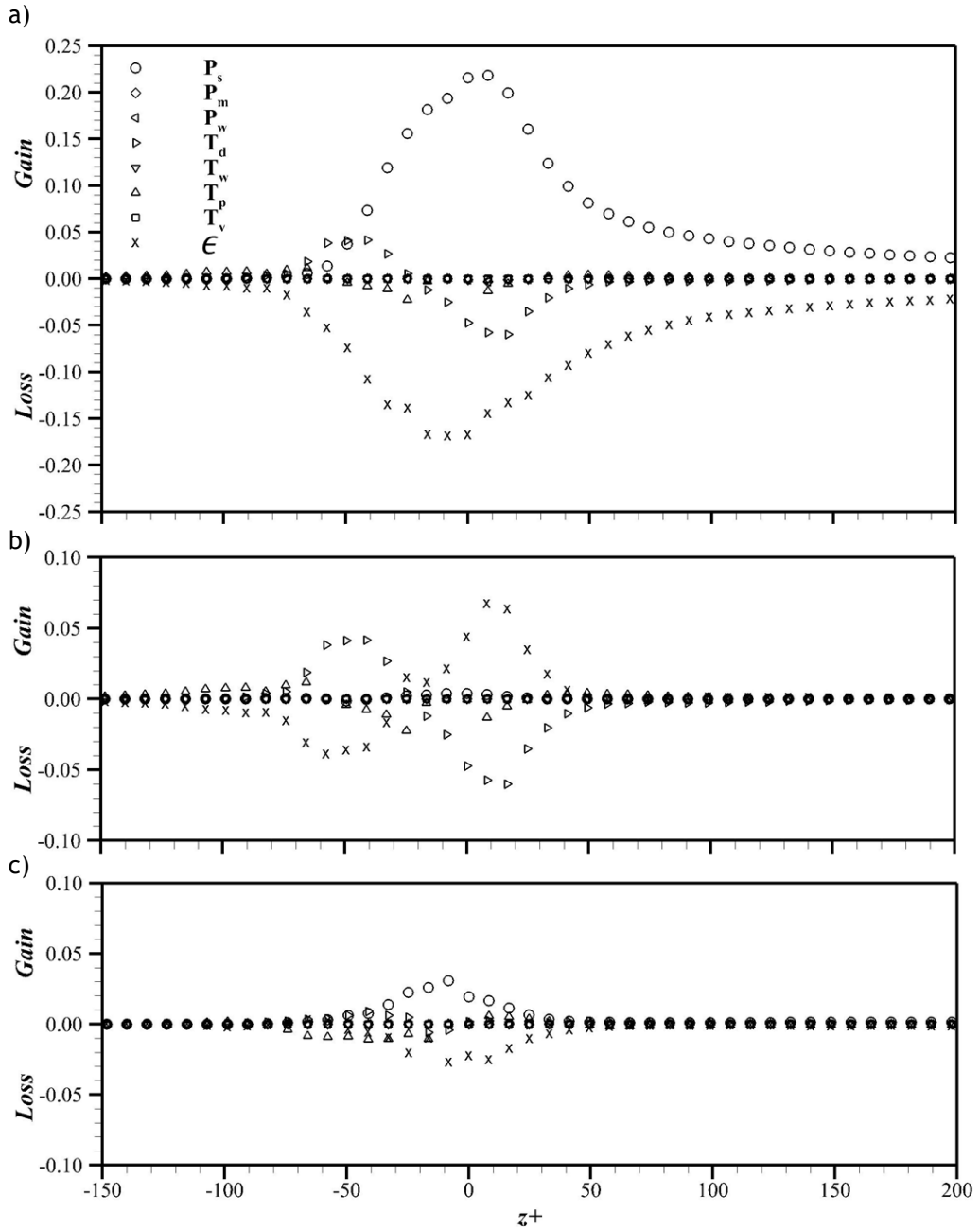
Figure 6.16. LES-F DA TKE budget terms normalised by u_*^4/υ against $z^+ = zu_*/\upsilon$ in the **(a)** streamwise direction, including the legend used for Fig's. 6.16(a-c); **(b)** spanwise direction; and **(c)** wall-normal direction.

The magnitude of the non-negligible streamwise TKE budget terms (excluding $\in$ as it is expressed here as the residual of the other terms) of the LES-F case, namely P_S, T_D, and T_p, are further explored in isolation in Fig's. 6.17(a)-(c). Using the same spatially averaged probe group's (PG's) as applied earlier in Fig's. 6.12 and 6.13,

for brevity, the spatial variance of the vertical distribution of the TKE budget terms is highlighted in Fig's. 6.17(a)-(c) for LES-F.
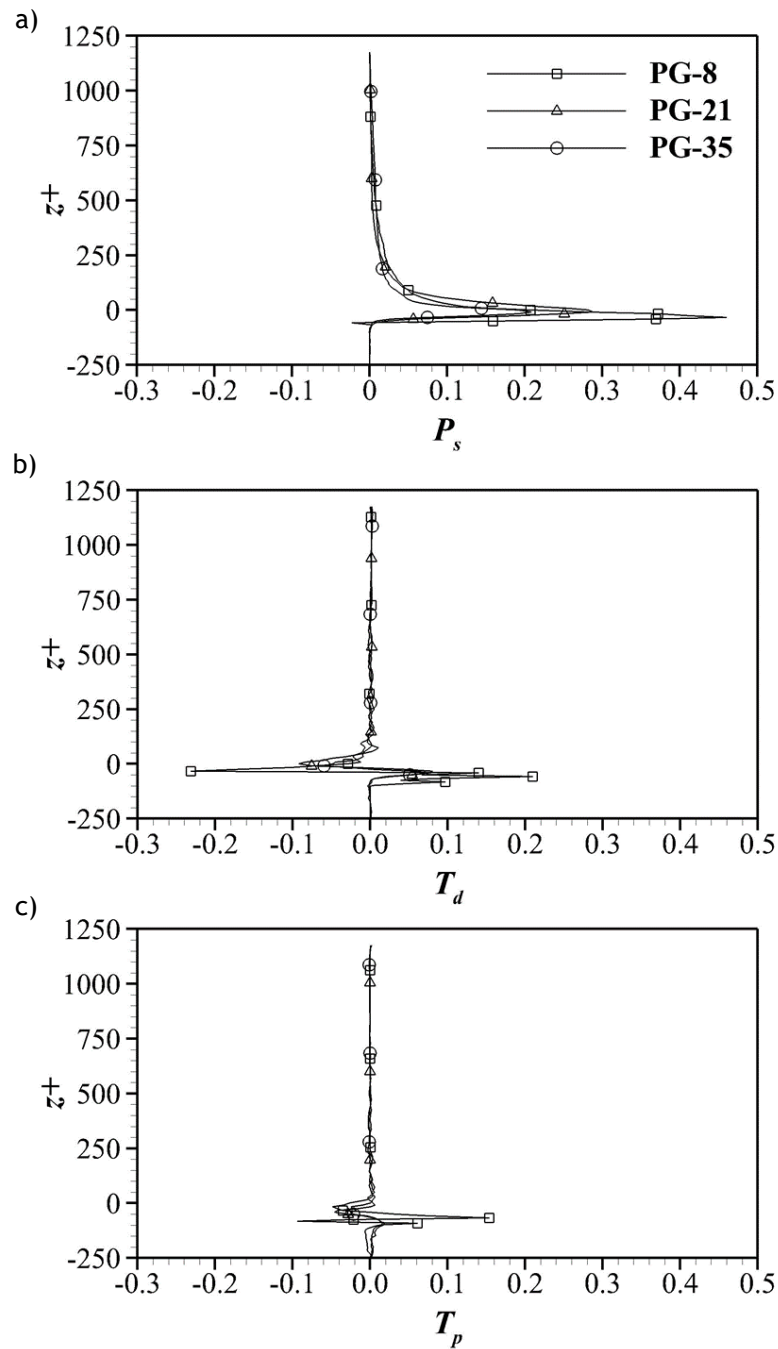
Figure 6.17. Vertical distribution of **(a)** shear production; **(b)** vertical diffusion transport; and **(c)** pressure transport, DA TKE budget terms for LES-F in the streamwise direction normalised by u_*^4/υ against $z^+ = zu_*/\upsilon$ for specific probe groups (PG). The legend for Fig's. 6.17(a)-(c) is the same as displayed in Fig. 6.17(a).

The peak shear production shown in Fig. 6.17(a) is highly spatially variant in the near-bed region with PG-8 having a peak P_s of 0.46 (twice the DA P_s shown in Fig. 16(a)) and PG-35 with a peak P_s of 0.21. The 6 probes within PG-8 are all positioned such that in the near-bed region they are above a pore of approximate depth $0.07h$ within the uppermost layer of the bed geometry. Whereas, in the case of PG-35, the probes are positioned above a pore approximately $0.21h$ in depth.

Clearly, the shear production is highly affected by the porosity of the bed surface and could be related to increased wall-normal velocity within the vicinity of bed particles. However, the P_s profiles do all collapse upon one another beyond $z+ \geq 250$, again suggesting that the influence of the roughness surface upon the TKE distribution is confined to the near-bed region. A similar trend of any spatial variance in the TKE quickly converging with increased elevation beyond the near-bed region is observed for all the other significant TKE budget terms shown in Fig's. 6.12(b) and (c).

The pressure transport term, T_p, of the LES-F case presented in Fig. 6.12(c) is particularly interesting in comparison to the other TKE budget terms as it appears to be the only non-negligible term that propagates deep into the bed beyond $z+ \geq -150$. Though only small in magnitude, being the only non-negligible term, the influence of T_p on the interstitial characteristics of the bed could well be highly significant, particularly in the region below 2 particle layers from the roughness surface.

6.4. Summary

In this chapter, the LES of flow with low relative submergence was conducted above a porous roughness surface characteristically representative of a natural gravel riverbed with lesser surface roughness. The bulk flow statistics were analysed against the wider literature before a more in-depth investigation into the effects of porosity and roughness upon the mean velocity TKE as well as the TKE fluxes in the streamwise and wall-normal directions was conducted. Spectral analysis was also conducted using derived convection velocities. The TKE budget was also explored in both the streamwise and spanwise directions in terms of the flow field at large by means of applying double averaging. Through application of only streamwise spatial averaging of the various probe groups used in this study, the non-negligible TKE budget terms were analysed in isolation to highlight any spatial variation in the magnitude of the budget terms and thus also their relative contribution.

The main conclusions are:

- The simulated channel flow was found to be highly representative of flows found above other permeable roughness elements found in the literature regardless of grid resolution in terms of velocity profile, Reynolds normal and shear stresses, turbulence intensity, skewness, and kurtosis.

- The logarithmic region of the velocity profiles of both the LES-C and LES-F cases were found to match very well with a von Karman's constant of 0.36 and a zero-displacement of approx. 6.2 mm, and 13.5 mm, respectively.

- Turbulent eddies above rough, porous naturalistic riverbeds have small wavelengths, high velocity, and high inertia resulting in upwards, rather than downstream propagation. Therefore, the convection velocities of such eddies are lower than the local mean velocity and must be considered in spectral analysis. It was also shown that turbulent eddies decay faster above porous, rough beds than that above smooth, impermeable beds and that this may be due to their small wavelength.

- The wavenumber energy frequency spectra analysis for the LES-F case made clear that near the roughness surface, in the lower layers of the channel flow, larger wavelengths make a greater contribution to the turbulent kinetic energy than in the upper layers of the flow. Also, through analysis of the pre-multiplied streamwise wavenumber spectra, the magnitude of the TKE reduces as the elevation increases away from the roughness surface for the LES-F case.

- The influence of the spatial variance of the roughness surface topography on the TKE distribution in the LES-F case was found to not only be confined to the near bed region but also determines the elevation over which the TKE distribution is affected.

- The shear production term of the TKE budget for the LES-F case was found to be highly affected by the porosity of the bed surface being far larger in magnitude above shallow pores compared to relatively deep pores.

- The pressure transport term for the LES-F case appears to be the only non-negligible term that propagates deep into the bed beyond $z+ \geq -150$. Though only small in magnitude, being the only non-negligible term, the influence of T_p on the interstitial characteristics of the bed could well be highly significant, particularly in the region below 2 particle layers from the roughness surface.

The results presented in this chapter show that the large-eddy simulation undertaken here, using novel bed geometry also developed in this study, are highly

representative of flows above naturalistic and artificial riverbeds found in the literature. In simulating such flows this study, in comparison with the literature, is able to show the influence bed characteristics, such as porosity and roughness, have upon the terms of the turbulent kinetic energy budget within both channel and bed elements of the domain throughout the water depth. The results presented here also show how turbulent kinetic energy penetrates the bed and that the most dominant budget term within the bed itself is the pressure transport term. This chapter also highlights that even at relatively coarse resolutions, the large eddy simulation code can resolve to a high degree complex turbulent flow field-bed interaction where the bed is represented by a nodal point cloud generated by Gmsh2Hydro3D.

Chapter 7

7. Conclusions, Contributions, and Future Research

7.1. Conclusions

This thesis is composed of three distinct bodies of work, namely the design and manufacture of a physical representation of a gravel riverbed matrix, the design and generation of a numerical representation of a gravel riverbed matrix, and the Large Eddy Simulation (LES) of a gravel riverbed.

For the development of a physical riverbed, a CAD model of a gravel riverbed matrix 120 mm in depth, 300 mm wide, and 2.048 m long was created with an average particle diameter of 28 mm. Using a CNC machine, a novel physical representation of a gravel riverbed was manufactured from cast acrylic consisting of 23 components that assemble through interference fitting to create an artificial riverbed. The artificial riverbed was then analysed in comparison with both natural and artificial riverbed data found in the literature. The results show that the developed method can offer the physical approximation of a gravel bed surface similar to a natural gravel riverbed with comparable surface roughness, yet reduced particle size variance, comparable particle distribution, and porosity within limits, but at the extreme end of the scale.

In the generation of a numerical riverbed, a CAD model of a gravel riverbed matrix 0.36 m in depth, 1.44 m wide and 0.72 m long was created with an average particle diameter of 90 mm. A numerical approximation was generated by applying a meshing algorithm to the CAD model geometry using the open-source program Gmsh (Geuzaine et al. 2009). The resulting unstructured, tetrahedral mesh was then

re-meshed using the code Gmsh2hydro3D, which was developed as part of this study, to give two structured, hexahedral mesh versions at different resolutions suitable for application in the LES code Hydro3D (Ouro and Stoesser, 2017). The two different resolution mesh versions, MC and MF, were also analysed in comparison to the geometry from which they originate, as well as natural and artificial riverbed data found in the literature. The results show that the developed Gmsh2Hydro3D process can offer the numerical approximation of highly complex geometry without significantly changing the characteristics of that geometry. Also, the results of analysing the developed scaled riverbed show that it is comparable to the previously created artificial riverbed and thus, can also be characterised as being similar to a natural gravel riverbed with low surface roughness, as well as reduced particle size variance, comparable particle distribution, and porosity within limits, but at the extreme end of the scale.

The LES of flow with low relative submergence was conducted above the MC (LES-C) and MF (LES-F) mesh versions of the gravel riverbed. The bulk flow statistics were analysed against the wider literature before a more in-depth investigation into the effects of porosity and roughness upon the mean velocity TKE as well as the TKE fluxes in the streamwise and wall-normal directions was conducted. Spectral analysis was conducted using derived convection velocities allowing both contours and profiles to be plotted. The TKE budget was also explored in both the streamwise and spanwise directions in terms of the flow field at large by means of applying double averaging. Through application of only streamwise spatial averaging of the various probe groups used in this study, the non-negligible TKE budget terms were analysed in isolation to highlight any spatial variation in the magnitude of the budget terms and thus also their relative contribution. The results of the LES are highly representative of flows above naturalistic and artificial riverbeds found in the literature. In simulating such flows this study shows the influence bed characteristics, such as porosity and roughness, have upon the terms of the turbulent kinetic energy budget within both channel and bed elements of the domain throughout the water depth. The results presented here also show how turbulent kinetic energy penetrates the bed and that the most dominant budget term within the bed itself is the pressure transport term. This study also highlights that even at relatively coarse resolutions, the LES code is able to resolve to a high degree complex turbulent flow field-bed interaction where the bed is represented by a nodal point cloud generated by Gmsh2Hydro3D.

7.2. Contributions

The contributions of the current thesis to the research topic of near-bed and interstitial turbulent flow phenomena are as follows:

- From an experimental point of view, the novel methodology presented in this thesis allows for the creation of a physical artificial riverbed that is highly representative of a natural gravel riverbed that allows for the study of numerous turbulent flow phenomena. The physical artificial riverbed was manufactured from CNC'd cast acrylic to within a very high tolerance of a CAD generated model of a gravel riverbed. The demonstrated methodology could be followed to generate other highly complex hydraulic structures for very different investigations.

- A novel methodology has also been developed in this thesis for numerically representing a CAD generated model of a gravel riverbed in a nodal point cloud form that is suitable for use with the immersed boundary method (IBM). This methodology has been shown in this thesis to generate highly accurate nodal representations of complex geometries at disparate resolutions. The developed methodology could be followed to numerically represent other highly complex geometries for use in CFD code, such as Hydro3D (Ouro and Stoesser, 2017), that also employ the IBM.

- Using large-eddy simulation this thesis has also presented analysis of turbulent flow within the near-bed and interstitial regions of a representative gravel riverbed. The bulk flow statistics, wavenumber spectra, pre-multiplied wavenumber spectra, mean velocity turbulent kinetic energy (TKE), TKE fluxes, and TKE budget are all analysed and show the effects of roughness and porosity on the flow characteristics, in particular, the vertical distribution of TKE throughout the flow field.

7.3. Future Research

The present study has demonstrated the capability of two new methodologies for the representation of complex geometries for fluid dynamic studies both physically and numerically. These methodologies can be further extended to improve the geometric representation. Through the use of technologies such as photogrammetry or laser displacement scanning, a high-resolution 3D realisation of

any surface could be obtained. By importing the surface realisation into a CAD software package, effectively any complex geometry could then be modeled. Then, that same geometry could be generated using the methodologies outlined in this thesis in either physical or numerical form for either experimental or computational study. With such a combination of technologies it would be possible to generate a highly accurate numerical representation of a water-worked gravel riverbed yet to be seen in LES studies such as that undertaken here.

The LES cases investigated in this thesis are highly computationally expensive due to the resolution being set at the same level throughout the domain. Any future research of this ilk should include the addition of Local Mesh Refinement (LMR) methodologies to maintain high resolutions in the near bed region but coarsen the fluid solver mesh where such fine resolution is simply not needed. This would greatly reduce the computational effort and expense of conducting such research.

Additionally, only one set of flow conditions is investigated in this thesis at a bulk Reynolds number of 15,000 and at low relative submergence. The natural next step for the current study would be to run several further simulations across a range of conditions including lower and higher bulk Reynolds number as well as different flow depths and see the affect such changes have on the TKE distribution throughout the domain. Equally, the simulations conducted in this thesis use the same bed geometry model of relatively high porosity. To further understand the affect porosity has on the distribution of TKE throughout the domain, several further simulations should now be performed with bed geometry of higher and lower porosity under then same flow conditions.

The future application of free-surface boundary conditions through use of approaches such as the Level Set Method would further enhance such simulations and would improve understanding of the effects of near-bed turbulence on the free surface above porous beds.

A specific body of work looking at convection velocities above various highly porous, rough bed configurations under different flow conditions would also go some way to fully explain the systematic differences in convection velocities highlighted by this study.

The future comparison of the LES results presented here against the results of the experimental study (as briefly outlined in Chapter 4) conducted using the cast acrylic riverbed designed and manufactured in this study would also be a logical next step for this body of research. Such comparison would allow rigorous validation

and verification of the LES results as well as the elucidation of specific aspects of turbulent flow through further comparative analysis.

Ultimately, the future aim of the study presented in this thesis should be the simulation of a bed with mobile particles that suspend, settle, and resuspend on top and within an immobile bed matrix. Through implementation of a Euler-Lagrangian model, the tracking of individual sediment particles under turbulent conditions would be possible, but the computational cost of such a study may prove to be too expensive for existing technologies though the work by Maitri et al. (2020) and Papadopoulos et al. (2020) is making great strides in this area.

References

Aberle, J. 2007. Measurements of armor layer roughness geometry function and porosity. *Acta Geophyscia* 55, 23-32. doi: 10.2478/s11600-006-0036-5.

Aberle, J. and Nikora, V. 2006. Statistical properties of armored gravel bed surfaces. *Water Resources Research* 42. doi: 10.1029/2005WR004674.

Ackers, P. and White, W. R. 1973. Sediment transport: New approach and analysis. *Journal of the Hydraulics Division, American Society of Civil Engineers* 99, pp. 2041-2060.

Alfonsi, G. Ferraro, D. Lauria, A. and Gaudio, R. 2020. Numerical Investigation of Natural Rough-Bed Flow. In: Sergeyev, Y. D. and Kvasov, D. E. (eds). *Numerical Computations: Theory and Algorithms*. Switzerland: Springer, pp. 1-9. doi: 10.1007/978-3-030-40616-5_21.

Amsden, A. A. O'Rourke, P. J. and Butler, T. D. 1989. *KIVA-II: A Computer Program for Chemically Reactive Flows with Sprays*. Los Alamos National Laboratory Report LA-11560-MS, Los Alamos, New Mexico. doi: 10.2172/6228444.

Anderson, W. and Meneveau, C. 2011. Dynamic roughness model for large-eddy simulation of turbulent flow over multiscale, fractal-like rough surfaces. *Journal of Fluid Mechanics* 679, 288-314. doi: 10.1017/jfm.2011.137.

Baker, M. J. 2011. *CFD simulation of flow through packed beds using the finite volume technique*. PhD Thesis, University of Exeter.

Barros, J. M. Schultz, M. P. and Flack, K. A. 2018. Measurements of skin-friction of systematically generated surface roughness. *International Journal of Heat and Fluid Flow* 72, pp. 1-7. doi: 10.1016/j.ijheatfluidflow.2018.04.015.

Bartzke, G. Kuhlmann, J. and Huhn, K. 2016. Flow above and within granular media composed of spherical and non-spherical particles – using a 3D numerical model. *Continental Shelf Research* 117, pp. 67-80. doi: 10.1016/j.csr.2016.02.006.

Bear, J. 2007. *Hydraulics of Groundwater*. New York: Dover Publications, INC.

Best, J. Bennett, S. Bridge, J. and Leeder, M. 1997. Turbulence modulation and particle velocities over flat sand beds at low transport rates. *Journal of Hydraulic Engineering* 123(12), pp. 1118-1129. doi: 10.1061/(ASCE)0733-9429(1997)123:12(1118).

Blois, G. Smith, G. S. Best, J. L. Hardy, R. J. and Lead, J. R. 2012. Quantifying the dynamics of flow within a permeable bed using time-resolved endoscopic particle imaging velocimetry (EPIV). *Experiments in Fluids* 53 (1), 51-76. doi: 10.1007/s00348-011-1198-8.

Bomminayuni, S. and Stoesser, T. 2011. Turbulence Statistics in an Open-Channel Flow over a Rough Bed. *Journal of Hydraulic Engineering*, 137(11), 1347-1358. doi: 10.1061/(ASCE)HY.1943-7900.0000454.

Bomminayuni, S. Stoesser, T. and Ruether, N. 2014. Dispersion of a passive scalar in turbulent open channel flow. In: Schleiss, A. J. De Cesare, G. Franca, M. J. and Pfister, M. (eds). *River Flow*. CRC Press, pp. 147-154. doi: 10.1201/b17133-25.

Breugem, W.P. Boersma, B,J. and Uittenbogaard, R.E. 2006. The influence of wall permeability on turbulent channel flow. *Journal of Fluid Mechanics* 562, 35-72. doi: 10.1017/S0022112006000887.

Buffin-Belanger, T. Reid, I. Rice, S. Chandler, J. H. and Lancaster, J. 2003. A Casting Procedure for Reproducing Coarse-Grained Sedimentary Surfaces. *Earth Surface Processes and Landforms* 28, pp. 787-796. doi: 10.1002/esp.490.

Cameron, S.M. Nikora, V.I. and Stewart, M.T. 2017. Very-large-scale motions in rough-bed open-channel flow. *Journal of Fluid Mechanics* 814, 416-429. doi:10.1017/jfm.2017.24.

Cao, Z. 1997. Turbulent bursting-based sediment entrainment function. *Journal of Hydraulic Engineering* 123(3), pp. 233-236. doi: 10.1061/(ASCE)0733-9429(1997)123:3(233).

Carling, P. A. Whitcombe, L. Benson, I. A. Hankin, B. G. and Radecki-Pawlik, A. M. 2006. A new method to determine interstitial flow patterns in flume studies of sub-

aqueous gravel bedforms such as fish nests. *River Research and Applications* 22, pp. 1-12. doi: 10.1002/rra.930.

Cevheri, M. McSherry, R. and Stoesser, T. 2016. A local mesh refinement approach for large eddy simulations of turbulent flows. *International Journal for Numerical Methods in Fluids* 82(5):261–285. doi: 10.1002/fld.4217.

Chorin, A.J. 1968. Numerical Solution of the Navier-Stokes Equation. *Mathematics of Computation* 42(3), 490-507. doi: 10.1023/A: 1021973025166.

Cignoni, P. Callieri, M. Corsini, M. Dellepiane, M. Ganovelli, F. and Ranzuglia, G. 2008. MeshLab: an Open-Source Mesh Processing Tool. *Eurographics Italian Chapter Conference*. doi: 10.2312/LocalChapterEvents/ItalChap/ItalianChapConf2008/129-136.

Dark, A. L. 2017. *Numerical Modelling of Groundwater–Surface Water Interactions with the Double-Averaged Navier-Stokes Equations*. Ph.D. Thesis, University of Canterbury, Christchurch, New Zealand.

Das, B. M. 2008. *Advanced Soil Mechanics*. 3rd ed. Taylor and Francis, Abingdon, UK.

Del Alamo, J. C. and Jimenez, J. 2009. Estimation of turbulent convection velocities and corrections to Taylor's approximation. *Journal of Fluid Mechanics* 640, pp. 5-26. doi: 10.1017/S0022112009991029.

Dittrich, A. and Koll, K. 1997. Velocity field and resistance of flow over rough surfaces with large and small relative roughness. *International Journal of Sediment Research* 12(3), 21-33.

Dwivedi, A. Melville, B. and Shamseldin, A. Y. 2010. Hydrodynamic forces Generated on a Spherical Sediment Particle During Entrainment. *Journal of Hydraulic Engineering* 136(10), pp. 756-769. doi: 10.1061/(ASCE)HY.1943-7900.0000247.

Elliott, A. H. and Brookes, N. H. 1997. Transfer of nonsorbing solutes to a streambed with bedforms: theory. *Water Resources Research* 33, pp. 123-136.

Fang, H. Han, X. He, G. and Dey, S. 2018. Influence of permeable beds on hydraulically macro-rough flow. *Journal of fluid Mechanics* 847, 552-590. doi:10.1017/jfm.2018.314.

Fee, C. 2017. 3D-printed porous bed structures. *Current Opinion in Chemical Engineering* 18, pp. 10-15. doi: 10.1016/j.coche.2017.07.003.

Ferraro, D. Coscarella, F. and Gaudio, R. 2016. Scales of turbulence in open-channel flows with low relative submergence. *Physics of Fluids* 31, 125114. doi: 10.1063/1.5127562.

Ferziger, J. H. ad Peric, M. 2002. *Computational Methods for Fluid Dynamics*. doi: 10.1016/S0898-1221(03)90046-0.

Fischer, P. F. Lottes, J. W. and Kerkemeier, S. G. *Nek5000* [Online]. Available at: http://nek5000.mcs.anl.gov [Accessed: 05 March 2021].

Fisher, M. J. and Davies, P. O. A. L. 1964. Correlation measurements in a non-frozen pattern of turbulence. *Journal of Fluid Mechanics* 18(97). doi: 10.1017/S0022112064000076.

Fraga, B. and Stoesser, T. 2016. Influence of bubble size, diffuser width, and flow rate on the integral behaviour of bubble plumes. *Journal of Geophysical Research: Oceans* 121, 3887-3904. doi: 10.1002/2014JC010066.

Fraga, B. Stoesser, T. Lai, C.C.K. and Socolofsky, S.A. 2016. A LES-based Eulerian-Lagrangian approach to predict the dynamics of bubble plumes. *Ocean Modelling* 97, 27-36. doi: 10.1016/j.ocemod.2015.11.005.

Fukuda, T. and Fukuoka, S. 2019. Interface-resolved large eddy simulations of hyperconcentrated flows using spheres and gravel particles. *Advances in Water Resources* 129, pp. 297-310. doi: 10.1016/j.advwatres.2017.10.037.

Garcia, M. H. 1999. Sedimentation and Erosion Hydraulics. In: Mays, L. W. eds. *Hydraulic Design Handbook*. New York: McGraw-Hill Education, pp. 180-292.

Geng, C. He, G. Wang, Y. Xu, C. Lozano-Duran, A. and Wallace, J. M. 2015. Taylor's hypothesis in turbulent channel flow considered using a transport equation analysis. *Physics of Fluids* 27, 025111. doi: 10.1063/1.4908070.

Geuzaine, C. Remacle, J.F. 2009. Gmsh: A Three-Dimensional Finite Element Mesh Generator with Built-In Pre-and Post-Processing Facilities. *International Journal for Numerical Methods in Engineering* 79, 1309-1331. doi: 10.1002/nme.2579.

Goharzadeh, A. Khalili, A. and Jorgensen, B.B. 2005. Transition layer thickness at a fluid-porous interface. *Physics of Fluids* 17(5), pp. 57-102. doi: 10.1063/1.1894796.

Goyeau, B. Lhuillier, D. Gobin, D. and Velarde, M.G. 2003. Momentum transport at a fluid-porous interface. *International Journal of Heat and Mass Transfer* 46, 4071-4081. doi: 10.1016/S0017-9310(03)00241-2.

Grass, A. J. 1971. Structural features of turbulent flow over smooth and rough boundaries. *Journal of Fluid Mechanics* 50(2), pp. 233-255. doi: 10.1017/S0022112071002556.

Guo, J. 1998. *Turbulent velocity profiles in clear water and sediment-laden flows*. PhD Thesis, Colorado State University, Fort Collins, Colorado.

Han, X. He, G. and Fang, H. 2017. Double averaging analysis of turbulent kinetic energy fluxes and budget based on large-eddy simulation. *Journal of Hydrodynamics* 29(4), 567-574. doi: 10.1016/S1001-6058(16)60769-2.

Hardy, R. J. Best, J. L. Lane, S. N. and Carbonneau, P. E. 2009. Coherent flow structures in a depth-limited flow over a gravel surface: The role of near-bed turbulence and influence of Reynolds number. *Journal of Geophysical Research* 114, F01003. doi: 10,1029/2007JF000970.

Huttenlocher, D. P. Klanderman, G.A. and Rucklidge, W.J. 1993. Comparing images using the Hausdorff distance. *IEEE Transactions on Pattern Analysis and Machine Intelligence* 15(9), 850-863. doi: 10.1109/34.232073.

Kanafi, M. M. 2016. *1-Dimensional surface roughness power spectrum of a profile or topography* [Online]. Available at: https://uk.mathworks.com/matlabcentral/fileexchange/54315-1-dimensional-surface-roughness-power-spectrum-of-a-profile-or-topography?s_tid=prof_contriblnk [accessed on 30 September 2020].

Khalili, A. Basu, A.J., Pietrzyk, U. and Raffel, M. 1999. an experimental study of recirculating flow through fluid-sediment interfaces. *Journal of Fluid Mechanics* 383, 229-247. doi: 10.1017/S0022112098003942.

Kim, J. and Hussain, F. 1993. Propagation velocity of perturbations in turbulent channel flow. *Physics of Fluids A* 5, p. 695. doi: 10.1063/1.858653.

Kim, T. Blois, G. Best, J.L. and Christensen, K. T. 2019. PIV measurements of turbulent flow overlying large, cubic- and hexagonally-packed hemisphere arrays. *Journal of Hydraulic Research* 58(2), 363-383. doi: 10.1080/00221686.2019.1581671.

Kim, T. Blois, G. Best, J.L. and Christensen, K. T. 2020. Experimental evidence of amplitude modulation in permeable-wall turbulence. *Journal of Fluid Mechanics* 887, A3. doi: 10.1017/jfm.2019.1027.

Kline, S. J. Reynolds, W. C. Schraub, F. A. and Runstadler, P. W. 1967. The structure of turbulent boundary layers. *Journal of Fluid Mechanics* 30, pp. 741-773. doi: 10.1017/S0022112067001740.

Kuwahara, F. Yamane, T. and Nakayama, A. 2006. Large eddy simulation of turbulent flow in porous media. *International Communications in Heat and Mass Transfer* 33, pp. 411-418. doi: 10.1016/j.icheatmasstransfer.2005.12.011.

Lee, D. Y. Lick, W. and Kang, S. W. 1981. The entrainment and deposition of fine-grained sediment in Lake Erie. *Journal of Great Lakes Research* 7, pp. 224-233. doi: 10.1016/S0380-1330(81)72049-5.

Leonard, A. 1975. Energy Cascade in Large-Eddy Simulations of Turbulent Fluid Flows. *Turbulent Diffusion in Environmental Pollution Proceedings of a Symposium held at Charlottesville* 18, 237-248. doi: 10.1016/S0065-2687(08)60464-1.

Lian, Y. P. Dallmann, J. Sonin, B. Roche, K. R. Liu, W. K. Packman, A.I. and Wagner, G. J. 2019. Large eddy simulation of turbulent flow over and through a rough permeable bed. *Computers and Fluids* 180, pp. 128-138. doi: 10.1016/j.compfluid.2018.12.015.

Lin, C. C. 1953. On Taylor's hypothesis and the acceleration terms in the Navier-Stokes equations. *Quarterly of Applied Mathematics* 10, p. 295.

Liu, Y. Stoesser, T. Fang, H. Papanicolalou, A. and Tsakiris, A.G. 2016. Turbulent flow over an array of boulders on a rough, permeable bed. *Computers and Fluids* 158, 120-132. doi: 10.1016/j.compfluid.2017. 05.023.

Maitri, R. V. et al. 2020. Lift-off of multiple particles in a narrow channel. *Chemical Engineering Science X* 8, pp. 2590-1400. doi: 10.1016/j.cesx.2020.100086.

Manes, C. Pokraac, D. McEwan, I. and Nikora, V. 2009. Turbulence structure of open channel flows over permeable and impermeable beds: a comparative study. *Physics of Fluids* 21, 125109. doi: 10.1063/1.3276292.

McSherry, R. Chua, K.V. Stoesser, T. and Mulahasan, S. 2018. Free surface flow over square bars at intermediate relative submergence. *Journal of Hydraulic Research* 1-19. doi: 10.1080/00221686.2017.1413601.

McSherry, R. Stoesser, T. and Falconer, R. 2017. Turbulent kinetic energy budget in open channel flows with fractal bed roughness. *37th IAHR World Congress*. August 13-18, Kuala Lumpur, Malaysia.

Mignot, E. Barthelemy, E. and Hurther, D. 2008. Turbulent kinetic energy budget in a gravel-bed channel flow. *Acta Geophysica* 56(3), 601-613. doi: 10.2478/s11600-008-0020-3.

Mignot, E. Bathelemy, E. and Hurther, D. 2009. Double-averaging analysis and local flow characterisation of near-bed turbulence in gravel-bed channel flows. *Journal of Fluid Mechanics* 618, 279-303. doi:10.1017/S0022112008004643.

Mohajeri, S. H. 2014. *Hydrodynamics of Gravel Bed Flows (Implication on Colmation)*. PhD Thesis, Queen Mary University of London.

Moin, P. 2009. Focus on fluids: Revisiting Taylor's hypothesis. *Journal of Fluid Mechanics* 640(1). doi: 10.1017/S0022112009992126.

Monaghan, J. J. 1992. Smoothed particles hydrodynamics. *Annual Review of Astronomy and Astrophysics* 30, pp. 543-574. doi: 10.1146/annurev.aa.30.090192.002551.

Morad, M. R. and Khalili, A. 2009. Transition layer thickness in a fluid-porous medium of multi-sized spherical beads. *Experiments in Fluids* 46, 323-330. doi: 10.1007/s00348-008-0562-9.

Moser, R. D. Kim, J. and Mansour, N. N. 1999. Direct numerical simulation of turbulent channel flow up to Re_τ=590. *Physics of Fluids* 11(4), pp. 943-945. doi: 10.1063/1.869966.

Nassrullah, S. Stubbs, A. Stoesser, T. Wilson, C.A. 2019. The validation of the logarithmic velocity profiles above rough-bed flows. *38th IAHR World Congress*. September 1-6, Panama City, Panama. doi: 10.3850/38WC092019-0421.

Nicoud, F. and Ducros, F. 1999. Subgrid-scale stress modelling based on the square of the velocity gradient tensor. *Flow, Turbulence and Combustion* 62(3), 183-200. doi: 10.1023/A:1009995426001.

Nield, D.A. and Bejan, A. 2017. *Convection in Porous Media*. 5th ed. Springer: New York, NY, USA.

Nikora, V. Goring, D.G. and Biggs, B.J.F. 1998. On gravel-bed roughness characterisation. *Water Resources Research* 34, 517-527. doi: 10.1029/97WR02886.

Nikora, V. I. and Goring, D. 2000. Flow turbulence over fixed and weakly mobile gravel beds. *Journal of Hydraulic Engineering* 126(9), pp. 679-690. doi: 10.1061/(ASCE)0733-9429(2000)126:9(679).

Nikora, V. Goring, D. McEwan, I. Griffiths, G. 2001. Spatially Averaged Open-Channel Flow Over Rough Bed. *Journal of Hydraulic Engineering* 127, 123-133. doi: 10.1061/(ASCE)0733-9429(2001)127:2(123).

Nikora, V. McEwan, I. McLean, S. Coleman, S. Pokrajac, D. and Walters, R. 2007. Double-Averaging Concept for Rough-Bed Open-Channel and Overland Flows: Theoretical Background. *Journal of Hydraulic Engineering* 133(8), pp. 873-883. doi: 10.1061/(ASCE)0733-9429(2007)133:(873).

Nikora, V. I. Stoesser, T. Cameron, S. M. Stewart, M. Papadopoulos, K. Ouro, P. McSherry, R. Zampiron, A. Marusic, I. and Falconer, R. A. 2019. Friction factor decomposition for rough-wall flows: theoretical background and application to open-channel flows. *Journal of Fluid Mechanics* 872, pp. 626-664. doi: 10.1017/jfm.2019.344.

Nino, Y. and Garcia, M. H. 1996. Experiments on particle-turbulence interactions in the near-wall region of an open channel flow: implications for sediment transport. *Journal of Fluid Mechanics* 326, pp. 285-319. doi: 10.1017/s0022112096008324.

Osher, S. and Sethian, J. A. 1988. Fronts propagating with curvature-dependent speed: Algorithms based on Hamilton-Jacobi formulations. *Journal of Computational Physics* 79(1), pp. 12-49. doi: 10.1016/0021-9991(88)90002-2.

Ouro, P. Wilson, C.A. Evans, P. and Angeloudis, A. 2017. Large-eddy simulation of shallow turbulent wakes behind a conical island. *Physics of Fluids* 29(12). doi: 10.1063/1.5004028.

Ouro, P.O. and Stoesser, T. 2017. An immersed boundary-based large-eddy simulation approach to predict the performance of vertical axis tidal turbines. *Computers and Fluids* 152, 74-87. doi: 10.1016/j.compfluid.2017.04.003.

Packman, A. I. Brooks, N. H. and Morgan, J. J. 2000. A physicochemical model for colloidal exchange between a stream and a sand streambed with bedforms. *Water Resources Research* 36, pp. 2351-2361. doi: 10.1029/2000WR900059.

Pan, Y. and Banerjee, S. 1995. A numerical study of free-surface turbulence in channel flow. *Physics of Fluids* 7(7), pp. 1649-1664. doi: 10.1063/1.868483.

Panah, M. and Blanchette, F.2018. simulating flow over and through porous media with application to erosion of particulate deposits. *Computers and Fluids* 166, 9023. doi: 10.1016/j.compfluid.2018.01.021.

Papadopoulos, K. Nikora, V. Vowinckel, B. Cameron, S. Jain, R. Stewart, M. Gibbins, C. and Frohlich, J. 2020. Double-averaged kinetic energy budgets in flows over mobile granular beds: insights from DNS data analysis. *Journal of Hydraulic Research* 58(4), pp. 653-672. doi: 10.1080/00221686.2019.1661291.

Persson, B. N. J. Albohr, O. Tartaglino, U. Volokitin, A.I. and Tosatti, E. 2005. On the nature of surface roughness with application to contact mechanics, sealing, rubber friction and adhesion. *Journal of Physics: Condensed Matter* 17, 1-62. doi: 10.1088/0953-8984/17/1/R01.

Peskin, C. S. 1972. Flow patterns around heart valves: A numerical method. *Journal of Computational Physics* 10(2), 252-271. doi: 10.1016/ 0021-9991(72)90065-4.

Piomelli, U. Balint, J. L. and Wallace, J. M. 1989. On the validity of Taylor's hypothesis for wall-bounded turbulent flows. *Physics of Fluids A* 4, p. 1521. doi: 10.1063/1.857432.

Pokrajac, D. and Manes, C. 2009. Velocity Measurements of a Free-Surface Turbulent Flow Penetrating a Porous Medium Composed of Uniform-Size Spheres. *Transport of Porous Media* 78, 367-383. doi: 10.1007/s11242-009-9339-8.

Raupach, M. R. and Shaw, R.H. 1982. Averaging procedures for flow within vegetation canopies. *Boundary-Layer Meteorology* 22, 79-90. doi: 10.1007/BF00128057.

Rodi, W. Constantinescu, G. and Stoesser, T. 2013. *Large-eddy simulation in hydraulics*. CRC Press. doi: 10.1201/b15090.

Rouzes, M. Moulin, F. Y. Florens, E. and Eiff, O. 2018. Low relative-submergence effects in a rough-bed open-channel flow. *Journal of Hydraulic Research* 57(2), pp. 139-166. doi: 10.1080/00221686.2018.1478894.

Sambrook Smith, G. H. and Nicholas, A. P. 2005. Effect on flow structure of sand deposition on a gravel bed: Results from a two-dimensional flume experiment. *Water Resources Research* 41, W10405. doi: 10.1029/2004WR003817.

Shen, G. Yuan, J. and Phanikumar, M.S. 2020. Direct numerical simulations of turbulence and hyporheic mixing near sediment-water interfaces. *Journal of Fluid Mechanics* 892, A20. doi: 10.1017/jfm.2020.173.

Singh, K. M. Sandham, N. D. and Williams, J. J. R. 2007. Numerical Simulation of Flow over a Rough Bed. *Journal of Hydraulic Research* 133(4), pp. 386-398. doi: 10.1061/(ASCE)0733-9429(2007)133:4(386).

Singha, A. and Balachandar, R. 2010. An Assessment of the Literature and Recent Developments on the Shallow Wake in an Open Chanel Flow. *Advances in Civil Engineering* 969407. doi: 10.1155/2010/969407.

Smagorinsky, J. 1963. General Circulation Experiments with the Primitive Equation I the Basic Experiment. *Monthly Weather Review* 91, pp. 99-164. doi: 10.1175/1520-0493(1963)091<0099:GCEWTP>2.3.CO;2.

Soni, J. P. Islam, N. and Basak, P. 1978. An experimental evaluation of non-Darcian flow in porous media. *Journal of Hydrology* 38, pp. 231-241. doi: 10.1016/0022-1694(78)90070-7.

Spiegel, M. R. and Stephens, L.J. 1999. *Theory and Problems of STATISTICS*, 3rd ed. McGraw-Hill: New York, NY, USA.

Stewart, M. T. Cameron, S.M. Nikora, V.I. Zampiron, A. and Marusic, I. 2018. Hydraulic resistance in open-channel flows over self-affine rough beds. *Journal of Hydraulic Research*. doi: 10.1080/00221686.2018.1473296.

Stoesser, T. 2008. Coherent flow structures – driving mechanism for hyporheic exchange in gravel beds. *River Flow* 1, pp. 765-772.

Stoesser, T. 2010. Physically Realistic Roughness Closure Scheme to Simulate Turbulent Channel Flow over Rough Beds within the Framework of LES. *Journal of Hydraulic Engineering* 136(10). 812-819. doi: 10.1061/(ASCE)HY.1943-7900.0000236.

Stoesser, T. 2014. Large-eddy simulation in hydraulics: Quo Vadis? *Journal of Hydraulic Research* 52(4), pp. 441-452. doi: 10.1080/00221686.2014.944227.

Stoesser, T. and Nikora, V. 2008. Flow structure over square bars at intermediate submergence: Large Eddy Simulation of bar spacing effect. *Acta Geophysica* 56(3), 836-893. doi: 10.2478/s11600-008-0030-1.

Stoesser, T. and Rodi, W. 2007. Large eddy simulation of open-channel flow over spheres. *High Performance Computing in Science and Engineering* 4, pp. 321-330. doi: 10.1007/978-3-540-36183-1_23.

Stoesser, T. Ruther, N. and Olsen, N. R. B. 2012. Calculation of primary and secondary flow and boundary shear stresses in a meandering channel. *Advance in Water Resources* 33, pp. 158-170. doi: 10.1016/j.advwatres.2009.11.001.

Stuart, T. A. 1953. Water currents through permeable gravels and their significance to spawning salmonids, etc. *Nature* 172, pp. 407-408. doi: 10.1038/172407a0.

Stubbs, A. Stoesser, T. and Bockelmann-Evans, B. 2018. Developing an approximation of a natural, rough gravel riverbed both physically and numerically. *Geosciences* 8 (12), p. 449. doi: 10.3390/geosciences8120449.

Suga, K. Matsumura, Y. Ashitaka, Y. Tominaga, S. and Kaneda, M. 2010. Effects of wall permeability on turbulence. *International Journal of Heat and Fluid Flow* 31(6), 974-984. doi: 10.1016/j.ijheatfluidflow.2010.02.023.

Sutherland, A. J. 1967. Proposed mechanism for sediment entrainment by turbulent flows. *Journal of Geophysical Research* 72, pp. 6183-6194. doi: 10.1029/JZ072i024p06183.

Takhanov, D. 2011. *Forchheimer Model for Non-Darcy Flow in Porous Media and Fractures*. MSc Dissertation, Imperial College London.

Taylor, G. I. 1938. Production and dissipation of vorticity in a turbulent fluid. *Proceedings of the Royal Society* A 164, p. 15. doi: 10.1098/rspa.1938.0002.

Thibodeaux, L. J. and Boyle, J. D. 1987. Bedform-generated convective transport in bottom sediment. *Nature* 325, pp. 341. doi: 10.1038/325341a0.

Tonina, D. and Buffington, J. M. 2007. Hyporheic exchange in gravel bed rivers with pool-riffle morphology: Laboratory experiments and three-dimensional modeling. *Water Resources Research* 43, W01421, pp.1-16. doi: 10.1029/2005WR004328.

Uhlmann, M. 2005. An immersed boundary method with direct forcing for the simulation of particulate flows. *Journal of Computational Physics* 209(2), 448-476. doi: 10.1016/j.jcp.2005.03.017.

van't Woudt, B. D. and Nicolle, K. 1978. Flow processes below a gravelly riverbed. *Journal of Hydrology* 17(2), pp. 103-120.

Vollmer, S and Kleinhans, M. G. 2007. Predicting incipient motion, including the effect of turbulent pressure fluctuations in the bed. *Water Resources Research* 43, W05410, pp. 1-16. doi: 10.1029/2006WR004919.

Weigard, A. and Gharib, M. 1995. Turbulent Vortex-Ring/Free-Surface Interaction. *Journal of Fluids Engineering* 117(3), p.374-381. doi: 10.1115/1.2817272.

Yoshizawa, A. and Horiuti, K. 1985. A Statistically-Derived Subgrid-Scale Kinetic Energy Model for the Large-Eddy Simulation of Turbulent Flows. *Journal of Physical Society of Japan* 54(8), pp. 2834-2839. doi: 10.1143/JPSJ.54.2834.

Yuan, J. and Piomelli, U. 2014. Roughness effects on the Reynolds stress budgets in near-wall turbulence. *Journal of Fluid Mechanics* 760, R1. doi:10.1017/jfm.2014.608.

Zaman, K. B. M. Q. and Hussain, A. K. M. F. 1981. Taylor hypothesis and large-scale coherent structures. *Journal of Fluid Mechanics* 112, p. 379. doi: 10.1017/S0022112081000463.

Zhong, D. Wang, G. and Ding, Y. 2011. Bed sediment entrainment function based on kinetic theory. *Journal of Hydraulic Engineering* 137(2), pp. 222-223. doi: 10.1061/(ASCE)HY.1943-7900.0000299.

Zhou, D. and Mendoza, C. 1993. Flow through porous bed of turbulent stream. *Journal of Engineering Mechanics* 119(2), pp. 365-383. doi: 10.1061/(ASCE)0733-9399(1993)119:2(365).